Determining the Distance Scale with CLASS: Studies of Two New Gravitational Lenses and a Measurement of the Hubble Constant

Thesis by

Christopher D. Fassnacht

In partial fulfillment of the requirements

for the degree of

Doctor of Philosophy

California Institute of Technology

Pasadena, California

1999

(Submitted October 19, 1998)

Acknowledgements

I have really enjoyed working on this thesis, due, in a large part, to the fantastic people working on the CLASS project. I am grateful for their enthusiasm and encouragement. I would first like to thank my advisor, Tony Readhead, for bringing me into the collaboration and, with his optimism, keeping me going when times looked bleak. I am grateful to Tony for trusting me to work independently, for being willing to send me to Europe to meet regularly with other members of the CLASS collaboration, and for showing me that it is possible to be a successful scientist without losing one's appreciation for the finer things in life. I would also like to thank Ian Browne, Steve Myers, Tim Pearson, and Peter Wilkinson for being mentors, friends, and, in my view, unofficial co-advisors. Tim was always willing to help me struggle through arcane AIPS tasks, to explain subtleties of VLA and VLBI mapping, to deal with questions about statistics, and to provide fantastic vegetables from his garden. Ian and Peter kept me in touch with the CLASS "big picture" and made me feel welcome on my trips to England. With their enthusiasm and generosity, my visits to Jodrell Bank were a joy, even when it rained every day for a month. Steve taught me a

lot about the nitty-gritty of the CLASS observations and data reduction and gamely put up with my naively cheery outlook. I am in awe at how smoothly the survey observations and Steve's automatic mapping procedure worked. I am also grateful to the other members of the CLASS collaboration. Andy Biggs, Roger Blandford, Ger de Bruyn, Neal Jackson, Dan Marlow, Leon Koopmans, Sunita Nair, David Rusin, and Donna Womble have provided friendship and lots of help along the way. The collaboration has been extremely smooth considering its size and that it has members at at least six institutions in the US and Europe.

I thank the members of my thesis committee: Roger Blandford, Mark Metzger, Gerry Neugebauer, Wal Sargent, Nick Scoville, and Hal Zirin. They gave me guidance, asked insightful questions, and never let me get away with glib answers. I am indebted to Martin Elvis and Pepi Fabbiano who showed me, when I was a young undergraduate, how much fun astronomy could be. They also hired me as a research assistant after I returned from the Peace Corps. I would never have gone on to graduate school in astronomy if I had not spent that year and a half with them at the CfA. I am extremely grateful to my undergraduate senior thesis advisor, John Biretta, for getting me interested in radio astronomy and VLBI.

I am grateful to Judy Cohen for repeatedly and generously observing CLASS objects during her Keck runs. Thanks also to George Djorgovski for getting important early data on 1608+656 during his Palomar and Keck time. For assistance with the

many observations conducted as part of this thesis, I thank the competent and helpful staff of Palomar Observatory, the W. M. Keck Observatory, the Owens Valley Radio Observatory, the Very Large Array, and the Very Long Baseline Array. I am grateful to Donna Womble for teaching me how to reduce data from spectroscopic observations; Gerry Neugebauer, Lee Armus, Aaron Evans, and Mike Pahre for teaching me how to reduce infrared data; David Hogg for teaching me the basics of gravitational lens modeling; Greg Taylor for help with radio mapping; Roy Gal for lots of help with the Palomar Sky Survey and reducing CCD images; Leon Koopmans for modeling 1608+656 and for thorough comments on paper; and Martin Shepherd and Erik Leitch for teaching me how to program in C. I hope that one day the quality of my programs may approach that of Martin's programs. The above list only begins to touch on the number of people who generously gave of their time to help me understand a problem. I am grateful to them all.

I thank Cheryl Southard and Martin Shepherd for keeping the computers running smoothly and to Nanci Candelin, Diane Fujitani, Anna Marie Hetman, Sandy Lester, Candi Lewis, Carlton Parker, and Gita Patel for keeping the department running smoothly.

The friends I made while I was at Caltech made graduate school much more fun than I had expected it to be. I am grateful for the support and friendship of my fellow graduate students. Special thanks go to those with whom I was lucky enough to share

an office: Rachel Akeson, Andrew Baker, Ken Banas, John Cartwright, John Gizis, Laura Grego, Mindy Kellogg, Marc Kuchner, and Paul Speaker. I regret that only Ken and Mindy were brave enough to continue the Robinson 03 hair-dying tradition that Laura, Rachel, and I started. I thank Rebecca Bernstein for matchmaking that was not nearly as subtle as she now claims. Mike Pahre and Suzanne Elsasser made me feel at home when I first arrived at Caltech and provided me with many tasty dinners over the years. I passed many pleasant hours with John Gizis, David Hogg, Erik Leitch, and Gautam Vasisht drinking coffee and playing pool, and almost always getting a bit of science discussed as well. Gautam deserves special mention for the time vs. frequency plot on the blackboard in the lozenge. I thank John Yamasaki for his unfailing moral support, fantastic barbecues, and for lending me his panniers for my trip across New Zealand. I am grateful to Gerry Neugebauer and the Infrared Army for making me feel welcome at their lunches. Lunch with the IRA was something that I looked forward to every week, even though I was constantly harassed about the value of H_0. I thank Lee Armus for magnificent softball managing. For crazy times, failed birthday hikes, and outrageously spicy cookfests, I thank Babra Akmal, Alexa Harter, Hideo Mabuchi, Tom Murphy, Reinaldo Román, Carlotta Scaramuzzi, and Bill Weber. I thank Brad Behr and Brian Kern for all of those early morning workouts that kept me in shape during grad school. I also thank the members of the intramural volleyball (Noisy Receivers, Eat at Achmed's), soccer (Big Head Todd,

Cataclysmic Variables, Protostars), and softball (The A-hats, Ether Binge, Downs Syndrome) teams which which I've been involved.

How can I thank my family enough for their love, humor, and support? They have always been behind me in my crazy adventures, whether going off to Ghana for two years or getting a Ph.D. in astronomy. My mother has been an inspiration to me and has provided me with a shining example of how to handle adversity with dignity and courage. I am also thankful that she dragged us children around the world when we were growing up and made us see what a wonderfully diverse collection of cultures it contains. My wonderful sisters, Karin and Heidi, are my friends as well as my siblings. They have provided a great support network for me, yet have never been content to stay in their big brother's shadow. I am proud of the successes that they have had, and I'm glad that we have remained so close in spite of the distance that separates us. My grandparents and Aunt Babs have been tremendously supportive over the last five years; I only wish I could have seen them more often. I wish I knew my Aunt Carol and my cousins better.

Finally, I thank Lori Lubin, who has been my rock and my muse. I would never have made it without her. She helped me through the job search, read my papers with a critical eye, and cheered me up when I was feeling down. Without her wisdom and compassion, the daunting task of finishing my thesis would have overwhelmed me. We have had a lot of fun being together, whether exploring Hawaii, California,

and New Zealand, or sitting together eating pasta and laughing at the absurdity of human nature. I am so lucky to have found her.

Abstract

Gravitational lenses have the potential to be excellent tools for investigating the Universe. This thesis describes the Cosmic Lens All-Sky Survey (CLASS), a program to find new gravitational lenses, and presents data on two newly-discovered lenses, 1608+656 and 2045+265. One of the major goals of CLASS is to find "golden lenses," which can be used to measure the Hubble Constant (H_0). A measurement of H_0 requires the redshifts of the lensing object and the background source, a well-constrained model of the gravitational potential of the lensing object, and a measurement of time delays between the images of the background source.

The 1608+656 system contains four images of the background source, which is the unresolved core of a classical radio double source. The lensing galaxy is at a redshift of $z_\ell = 0.630$, while the background source is at a redshift of $z_s = 1.394$. Interestingly, the spectrum of the background object indicates that it is an "E + A" galaxy. Ground-based optical and infrared images clearly show the lensing galaxy at the location predicted by the lens models. Images taken with instruments on the *Hubble Space Telescope* further resolve the lensing galaxy into two distinct objects,

which may be a merging pair of galaxies.

Radio maps of the 2045+265 system also show four images of the background source. In addition, a fifth component appears in the maps. The radio spectrum of the fifth component is significantly different from the spectra of the other four components, and its location matches that of the lensing galaxy to within the positional errors. Therefore, it appears that the fifth component is the flat-spectrum core of the lensing galaxy. The redshift of the lensing galaxy is $z_\ell = 0.8673$. The spectrum of the background source shows one broad emission line, which appears to be Mg II at a redshift of $z_s = 1.28$. However, this redshift implies that the lensing galaxy is unusually massive and would have a rotation velocity two to three times what is observed in nearby galaxies of the same type. There is either a significant contribution by dark (or underluminous) matter associated with the lensing object or the source redshift is incorrect. More sensitive spectroscopy is needed to resolve this issue.

Preliminary observations of the 1608+656 system showed that the component flux densities varied by $\sim$15% on time scales of months. For this reason, I conducted a dedicated monitoring program with the Very Large Array (VLA) from October 1996 to May 1997. The observations took place, on average, every four days. The calibrated light curves for components A, B, C, and D show variations in flux density at the 3 – 5% level. Although the fractional variations are small, the time delays between the curves can be measured. The final values are $\Delta t_{BA} = 30^{+5}_{-7}$ d, $\Delta t_{BC} = 36^{+5}_{-8}$ d, and

$\Delta t_{BD} = 76^{+6}_{-7}$ d, where the 95% confidence levels have been obtained from Monte Carlo simulations. The model of the mass distribution of the lens correctly reproduces the image positions, flux ratios, *and* time delay ratios. The combination of the measured time delays with the lens model yields the first determination of H_0 from a CLASS lens: $H_0 = 59^{+5}_{-4}$(statistical) $\pm$ 15(systematic) km sec^{-1} Mpc^{-1}.

Contents

List of Tables

List of Figures

Chapter 1

Introduction: A Gravitational Lens Primer

In 1919, Dyson, Eddington, & Davidson (1920) measured the deflection of light from a distant star as it passed close to the Sun. This measurement provided observational confirmation of the validity of Einstein's theory of general relativity because the measured angle of deflection was inconsistent with the Newtonian value based on the corpuscular theory of light, and consistent with the value predicted by general relativity. Papers by Eddington (1920) and Chwolson (1924) soon followed, which discussed the possibility that the deflection of light by nearby stars might produce multiple images of a background star. Zwicky (1937) realized that, although stars did not contain enough mass to produce multiple images with wide enough separations to be detected, galaxies (nebulae) were massive enough to produce detectable separations. He also noted that gravitational lenses could be used as cosmological

telescopes to magnify extremely distant objects. In 1979, Zwicky's prediction was confirmed when Walsh, Carswell, & Weymann (1979) discovered the first gravitational lens, the "double quasar" 0957+561.

In the mid-1960's, still fifteen years before the existence of gravitational lenses was observationally confirmed, Refsdal (1964) developed an elegant method for using lens systems to determine the distance scale of the Universe and, thus, to measure the Hubble Constant. This method will be described in §1.7 and is the motivation for most of the observations and analysis presented in this thesis. In particular, Chapter 5 describes a direct application of Refsdal's method.

This chapter is intended to give a brief overview of gravitational lens theory, focusing on the areas treated in the rest of the thesis. In particular, this chapter treats "strong" lensing by galaxies, in which multiple images of the background source are formed, and does not deal with "weak" lensing. The inspired reader should refer to the works cited in this chapter for a more detailed treatment. Among the excellent general resources available are articles by Blandford & Narayan (1986; 1992), lecture notes by Blandford & Kochanek (1987) and Narayan & Bartelmann (1998) and the *Gravitational Lenses* textbook by Schneider, Ehlers, & Falco (1992).

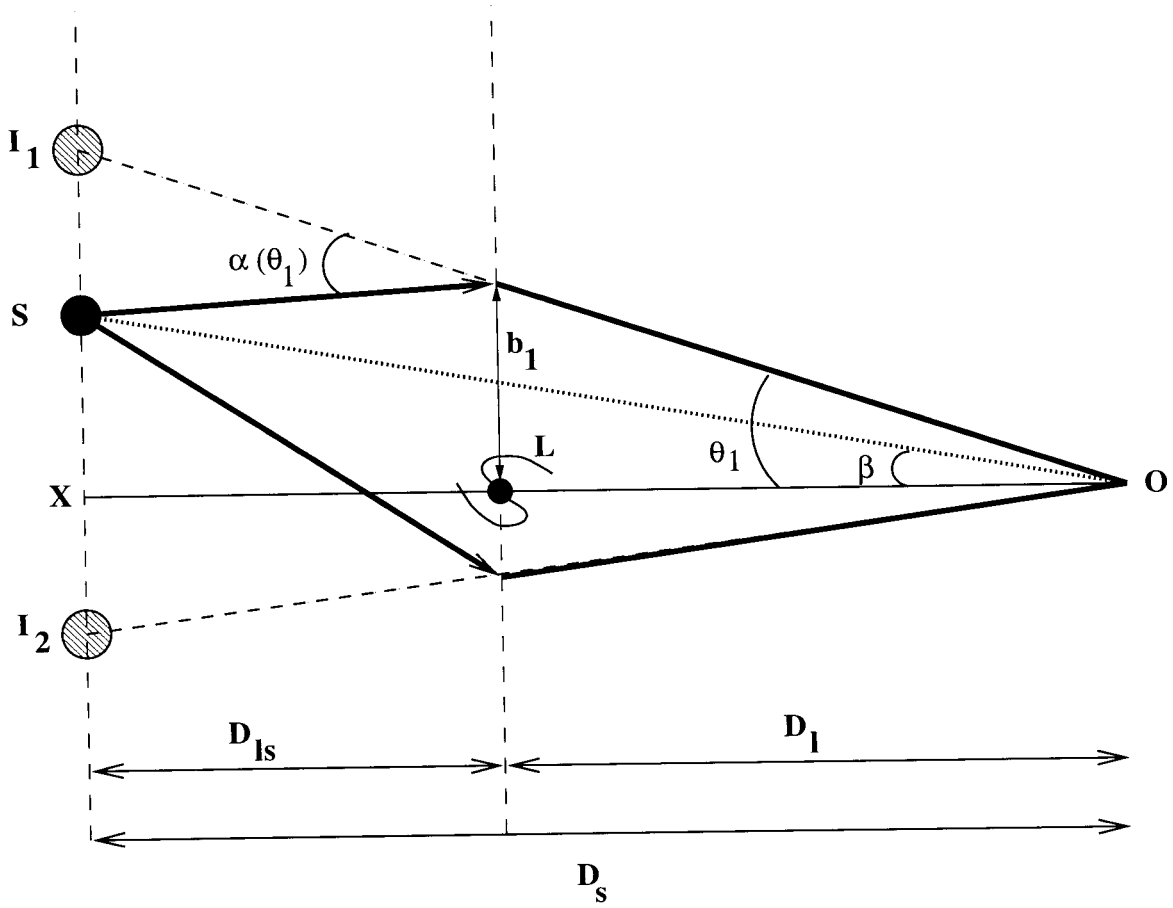

Figure 1.1 Cartoon of a gravitational lens system. Two rays from the background source (S), shown by the heavy lines, have been deflected by the lensing object (L) and arrive at the observer (O) from different directions. The observer sees two images of the background source at I_1 and I_2. The sizes of the angles have been exaggerated for clarity.

1.1 The Lens Equation

In a gravitational lens, light traveling from an astronomical source (the "background source") to an observer is deflected by the gravitational potential of an intervening object (the "lens"). In some systems the lensing potential causes deflections which produce more than one possible path from the source to the observer through the

potential. In these systems, multiple images of the background source are formed. Figure 1.1 shows a cartoon representation of such a situation. The background source located at "S" emits light that is deflected by the lens at "L." The two rays drawn as heavy lines in the figure are bent in such a way that both arrive at the observer ("O") in spite of taking different paths through the lensing potential. The observer will see two images of the background source at I_1 and I_2. The distances from the observer to the lens and source are given by D_ℓ and D_s, respectively. The distance between the lens and source is $D_{\ell s}$. The two dashed vertical lines represent the source plane, containing S, I_1, and I_2; and the lens plane, containing L. If we define an optical axis by drawing a line through O and L, we can define the angular positions of the objects of interest: β for the source position S, and $\theta_{1,2}$ for the image positions I_1 and I_2, respectively. An additional angle $\alpha(\theta)$ quantifies the deflection of a light ray when it passes through the lensing potential at an angular displacement θ from the optical axis. Now we can perform a simple geometric and trigonometric analysis of the system. It is obvious that in the source plane the distance between the optical axis and the image I_1 is

$$\overline{XI_1} = \overline{XS} + \overline{SI_1}, \tag{1.1}$$

and that a similar equation holds for $\overline{XI_2}$. All of the angles involved in gravitational lensing are small, so we can approximate $\sin\delta \sim \delta$, where δ represents any of the

angles discussed above. A simple substitution then gives

$$D_s\theta_i = D_s\beta + D_{\ell s}\alpha(\theta_i), \tag{1.2}$$

or

$$\theta_i = \beta + \frac{D_{\ell s}}{D_s}\alpha(\theta_i), \tag{1.3}$$

where θ_i represents the angular position of the i^{th} image of the background source. Equation 1.3 is referred to as the lens equation; it serves as the "first principle" on which much of lensing theory is based.

For a spherically symmetric lens, the source and image positions are collinear. However, for a general lens, this is not necessarily true. As such, the scalar quantities β, θ_i, and α need to be replaced by two-dimensional vector quantities $\vec{\beta}$, $\vec{\theta_i}$, and $\vec{\alpha}$. Note that all of these quantities are dimensionless *angular* quantities. For physical distances in the lens plane, I will follow Schneider, Ehlers, & Falco (1992) and use $\vec{\xi}$. The physical and angular distances are related by $\vec{\xi} = D_\ell\vec{\theta}$. This relationship is used in several of the derivations in this chapter.

1.2 Cosmology and the Lens Equation

For the applications of the lens equation discussed in this thesis, both the lensing object and the background source are at cosmological distances. Thus, the effects of the expansion and possible curved geometry of the Universe must be taken into

account. The correction for these effects is achieved through the use of angular diameter distances in the lens equation. These quantities relate a physical distance in the plane of the sky, dx_p, to the angle that it subtends, $d\theta$:

$$dx_p = D_A \, d\theta, \tag{1.4}$$

which is exactly the role played by the physical distances D_ℓ, D_s, and $D_{\ell s}$ in the simple geometric derivation above. The use of angular diameter distances allows the lens equation to remain unchanged while all of the cosmological effects are contained in the definition of the distances.

The cosmological world model which controls the expansion factor of the Universe, $R(t)$, can be parameterized by four quantities: the mass density (ρ), the cosmological constant (Λ), the curvature index (k), and the Hubble Constant (H). These are often combined into the dimensionless quantities (e.g., Peebles 1993, p. 100; Carroll, Press, & Turner 1992):

$$\Omega_M = \frac{8\pi G}{3H_0^2}\rho_0, \quad \Omega_\Lambda = \frac{\Lambda}{3H_0^2}, \quad \Omega_k = -\frac{kc^2}{R_0^2 H_0^2}, \tag{1.5}$$

where the subscript 0 indicates the value at the present time ($t = t_0$). These quantities are related by:

$$\Omega_M + \Omega_\Lambda + \Omega_k = 1. \tag{1.6}$$

For a general world model, the angular diameter distance between two objects at

redshifts of z_i and z_j, where $z_i < z_j$, is:

$$D_{ij} = \frac{c}{H_0(1+z_j)|\Omega_k|^{1/2}} \text{sinn}\left(|\Omega_k|^{1/2}\mathcal{I}(z_i, z_j)\right), \tag{1.7}$$

where

$$\mathcal{I}(z_i, z_j) = \int_{z_i}^{z_j} \frac{dz}{[(1+z)^2(1+\Omega_M z) - z(2+z)\Omega_\Lambda]^{1/2}} \tag{1.8}$$

and $\text{sinn}(x)$ is a function that depends on the value of k:

$$\text{sinn}(x) = \begin{cases} \sin(x) & (k=1) \\ x & (k=0) \\ \sinh(x) & (k=-1) \end{cases} \tag{1.9}$$

(Carroll, Press, & Turner 1992). In world models which have $\Lambda = 0$, the integral $\mathcal{I}(z_i, z_j)$ has an analytic solution, and the angular diameter distance can be written as:

$$D_{ij} = \frac{2c}{H_0} \frac{(1 - \Omega_M - G_i\, G_j)\,(G_i - G_j)}{\Omega_M^2\,(1+z_i)\,(1+z_j)^2}, \tag{1.10}$$

where

$$G_{i,j} = (1 + \Omega_M\, z_{i,j})^{1/2} \tag{1.11}$$

(e.g., Blandford & Narayan 1992).

1.3 The Deflection Angle

The distribution of mass in the lensing object determines the deflection angle, $\vec{\alpha}$. The simplest case is that of a point mass, i.e., a spherical body for which the impact parameter of the light ray, $\xi \equiv |\vec{\xi}|$, is much larger than the Schwarzschild radius of the object. In this case, the weak-field approximation is valid (e.g., Schneider, Ehlers, & Falco 1992). For a such an object with mass M, the general relativistic scattering angle is

$$\alpha = \frac{4\,G\,M}{c^2\,\xi}, \tag{1.12}$$

which is twice the value predicted by the classical Newtonian calculation.

For more complex mass distributions, we must consider the effects of having many objects with different masses and different distances from the light ray. In cases such as those examined in this thesis, D_ℓ and $D_{\ell s}$ are much greater than the physical dimensions of the mass distribution. In these situations it is possible to use the "thin lens" approximation and assume that all of the deflection by the lensing masses occurs at one specific location rather than considering the effects on the light as it passes through the distribution. Thus, it is possible to project the mass distribution down to a plane perpendicular to the line of sight (the "lens" or "image" plane). The final deflection angle becomes the sum of the deflection angles produced by the individual

masses distributed in the plane:

$$\vec{\alpha}(\vec{\xi}) = \sum_i \frac{4\,G\,m_i\,(\vec{\xi} - \vec{\xi_i})}{c^2\,|\vec{\xi} - \vec{\xi_i}|^2}, \tag{1.13}$$

where $\vec{\xi_i}$ is the physical position of mass m_i. The deflection angle produced by an extended object with a smooth mass distribution is a natural extension of Equation 1.13 with the individual masses replaced by a projected *surface* mass density, $\Sigma(\vec{\xi'})$, of the lensing object:

$$\vec{\alpha}(\vec{\xi}) = \int \frac{4G\Sigma(\vec{\xi'})(\vec{\xi} - \vec{\xi'})}{c^2|\vec{\xi} - \vec{\xi'}|^2} d^2\xi' \tag{1.14}$$

where the integral is over the lensing plane.

1.4 Determining Lens Masses

The lens equation predicts interesting behavior when the background source and the lensing object are collinear, i.e., when $|\vec{\beta}| = 0$. In this case, the solutions of the lens equation produce a locus of positions in the lensing plane that defines a circle or ellipse, known as an "Einstein ring." Such rings have been seen in gravitational lens systems in which the background source is an extended radio object (Patnaik et al. 1992a; Lehár et al. 1997; Hewitt et al. 1988; Lehár et al. 1993; Langston et al. 1989; Jauncey et al. 1991; Patnaik et al. 1992b). Recently Einstein rings also have been detected in infrared images of lens systems obtained by the *Hubble Space Telescope* (King et al. 1998; Impey et al. 1998; Kochanek et al. 1998).

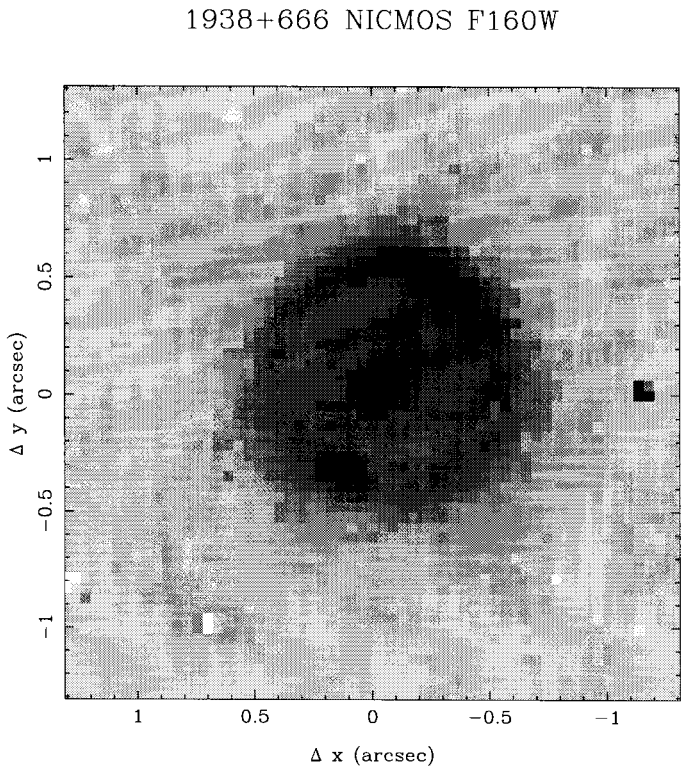

Figure 1.2 The Einstein ring in the gravitational lens system B1938+666. This image is from observations made with the Near Infrared Camera and Multi-Object Spectrograph (NICMOS) on HST by King et al. (1998). The lensing galaxy is the object at the center of the ring.

Figure 1.2 shows a particularly nice image of an infrared Einstein ring.

The relationship of the Einstein ring radius and the mass of the lensing object inside the ring can be derived straightforwardly from the lens equation and a description of the mass distribution of the lensing object. The derived mass is nearly independent of the form of the mass distribution. To illustrate this, I present two examples, both of which yield the same result. Both cases are spherically symmetric, so scalar quantities can be used in the equations. First, consider a point mass lens. Insert the expression for the deflection angle presented in Equation 1.12 into the lens

equation. Figure 1.1 shows that $\xi_i = D_\ell \theta_i$. Thus, the lens equation becomes

$$\theta_i = \beta + \frac{4GM}{c^2} \frac{D_{\ell s}}{D_\ell D_s} \frac{1}{\theta_i} \tag{1.15}$$

or

$$\theta_i^2 = \beta\theta_i + \frac{4GM}{c^2} \frac{1}{D}, \quad \text{where } D \equiv \frac{D_\ell D_s}{D_{\ell s}}. \tag{1.16}$$

If $\beta = 0$, the equation can be solved for M, giving the projected mass inside the Einstein ring:

$$M_E = \frac{c^2}{4G} \theta_E^2 \frac{D_\ell D_s}{D_{\ell s}} \tag{1.17}$$

$$= 1.22 \times 10^{11} \left(\frac{\theta_E}{1''}\right)^2 \left(\frac{D}{1\text{Gpc}}\right) M_\odot. \tag{1.18}$$

Another common representation for the lensing object is an isothermal sphere, which appears to be a good approximation to the mass (light + dark matter) distributions in galaxies from X-ray observations (Fabbiano 1989), well-constrained individual lens models (e.g., Kochanek 1995; Grogin & Narayan 1996), and lens statistics (e.g., Maoz & Rix 1993). In these spherically symmetric models, $\rho(\xi) \propto \xi^{-2}$, where ρ is the three-dimensional mass density. The density profile may continue rising to $\xi = 0$ (singular isothermal sphere) or may level off inside some core radius ξ_c (non-singular or softened isothermal sphere). Outside the core, the velocity dispersion, σ, is constant with radius. *Hubble Space Telescope* photometry of early-type galaxies suggest that the cores are effectively singular (e.g., Byun et al. 1996; Gebhardt et al. 1996), so the simple singular isothermal form is often used in lens models. The projected surface

density for a singular isothermal sphere is $\Sigma(\vec{\xi}) = \sigma^2/2G|\vec{\xi}|$, giving a deflection angle, $\alpha = 4\pi\sigma^2/c^2$, that is independent of the impact parameter. Again substitute this equation into the lens equation (1.3) and set $\beta = 0$ to get

$$\theta_E = \alpha \frac{D_{ls}}{D_s} = \frac{4\,\pi\,\sigma^2}{c^2} \frac{D_{ls}}{D_s}. \tag{1.19}$$

To find the mass inside the Einstein ring radius, express $\vec{\xi}$ in polar coordinates (ξ, ϕ) and integrate the surface mass density out to the physical distance ξ_E corresponding to the Einstein ring radius, such that

$$M_E = \int_0^{\xi_E} \Sigma(\xi)\,\xi\,d\xi\,d\phi = \frac{\pi\,\sigma^2\,\xi_E}{G}. \tag{1.20}$$

Replace σ^2 by the relationship derived from Equation 1.19, and set $\xi_E = D_\ell \theta_E$. The result is, once again, Equation 1.17.

Most lens systems do not exhibit Einstein rings. Instead, they typically contain multiple isolated images of the background source as in Fig. 1.1. However, in a typical lens system, the images form close to the Einstein ring radius (Schneider, Ehlers, & Falco 1992). Thus, the observed separation of the images in a lens system (or maximum separation in a system with more than two lensed images) roughly can be equated with the *diameter* of the Einstein ring, and Equation 1.17 can be used to estimate the lens mass.

1.5 The Lens Equation Revisited: The Time Delay Approach

So far I have taken a geometrical approach to the lens equation. There is, however, another way to describe a gravitational lens system. This second approach involves the computation of the light travel times of rays passing through the gravitational potential of the lens. These times are compared with the time that would have been taken by an undeflected ray propagating from the source to the observer if no lensing object were present. The differences in light travel times are referred to as the "time delays" produced by the lens. Two separate delays combine to produce the final time delay experienced by the deflected ray. The first is a geometric effect, Δt_{geom}, due to a difference in the lengths of the paths followed by the deflected and undeflected rays. The geometrical delay depends on the deflection angle and on the difference between the impact parameters of the deflected and undeflected rays at the lens plane. At the observer, the delay is

$$\Delta t_{geom}(\vec{\xi}) = (1 + z_\ell) \frac{1}{2c} \frac{D_\ell D_s}{D_{\ell s}} |\vec{\theta} - \vec{\beta}|^2 \tag{1.21}$$

where the factor $(1 + z_\ell)$ is needed to convert the delay measured at the lens plane to the delay observed at $z = 0$ (e.g., Blandford & Narayan 1986). The second contribution, Δt_{grav}, is a relativistic time delay caused by the passage of the ray through the

gravitational potential of the lens. For weak gravitational fields the metric is

$$ds^2 = -c^2\,(1 + \frac{2\Phi}{c^2})\,dt^2 + (1 - \frac{2\Phi}{c^2})\,(dx^2 + dy^2 + dz^2) \tag{1.22}$$

where Φ is the Newtonian potential chosen such that at large distances from a source of mass M, $\Phi = -GM/r$ (e.g., Schutz 1990). Light travels along null geodesics, implying that the light travel time along a ray is

$$\int dt = \frac{1}{c} \int (1 - \frac{2\Phi}{c^2})\,d\ell \tag{1.23}$$

where $d\ell$ is the line element along the ray. This can be compared with the light travel time taken in a flat spacetime

$$\int dt = \frac{1}{c} \int d\ell. \tag{1.24}$$

The difference between the two light travel times, after the correction for the redshift of the lens, is the gravitational time delay:

$$\Delta t_{grav} = -(1 + z_\ell)\,\frac{2}{c^3} \int \Phi\,d\ell \tag{1.25}$$

The time delay at any position in the lens plane can be found by adding Equations 1.21 and 1.25.

The time delay equation is often expressed in terms of a scaled two-dimensional gravitational potential, ψ, in order to produce a particularly simple version of the lens equation. The two-dimensional potential is constructed by integrating Φ along the line of sight and multiplying the result by the scaling factor, producing

$$\psi = \frac{2D_{\ell s}}{c^2 D_\ell D_s} \int \Phi\,d\ell. \tag{1.26}$$

Substituting ψ for the integrated Newtonian potential in the time delay equation yields

$$\Delta t = (1 + z_\ell) \frac{D_\ell D_s}{c D_{\ell s}} \left[\frac{1}{2} |\vec{\theta} - \vec{\beta}|^2 - \psi(\vec{\theta}) \right] \tag{1.27}$$

(e.g., Blandford & Narayan 1986).

Fermat's theorem states that the real light ray from a source to an observer is that member of a set of (virtual) null curves for which the light travel time is an extremum, usually the minimum. The application of Fermat's theorem to a gravitational lens implies that images of the background source form at the extrema in the time delay surface, which are found by differentiating Equation 1.27 with respect to $\vec{\theta}$ and setting the result to zero. This yields the lens equation in its time delay form:

$$\vec{\theta}_i = \vec{\beta} - \nabla_\theta \psi(\vec{\theta}). \tag{1.28}$$

This form of the lens equation is the backbone of the potential-based modeling presented in the next section. Figure 1.3 shows a contour plot representation of the time delay surface for a gravitational lens system. Images of the background source will form at the extrema of the delay surface.

From a comparison with Equation 1.3, we see that the deflection angle is related to the scaled potential by

$$\vec{\alpha}(\vec{\theta}_i) = \frac{D_{\ell s}}{D_s} \nabla_\theta \psi(\vec{\theta}). \tag{1.29}$$

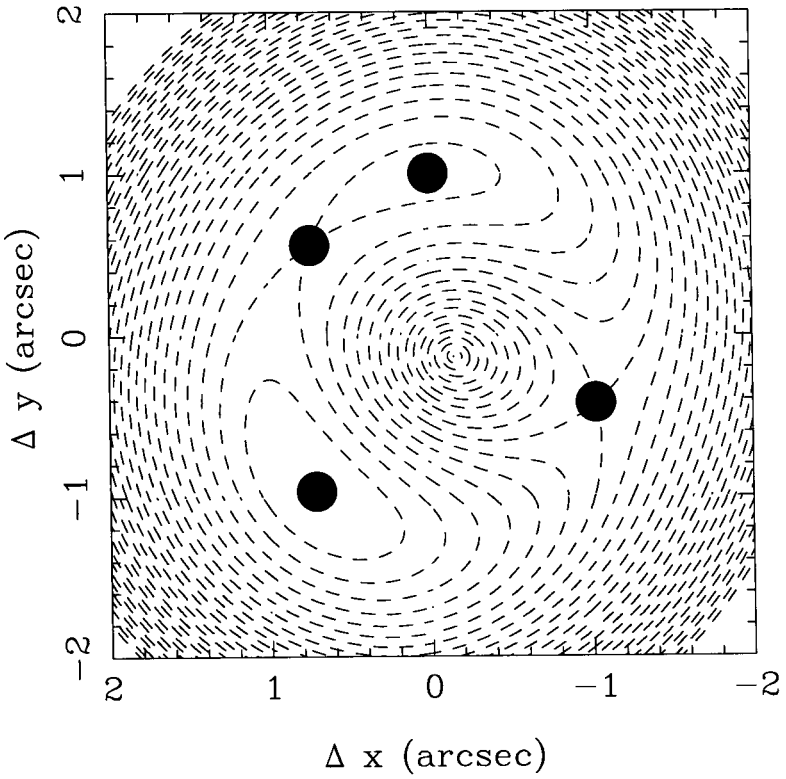

Figure 1.3 Time delay surface for a gravitational lens system, with the dashed lines representing contours of equal delay. The surface was created using a simple singular isothermal sphere plus mixed shear model (see §1.6) for the gravitational lens 1608+656 (see Chapter 3). The images, represented as filled circles, form at the extrema of the time delay surface. No image forms at the extremum at the center of the image because of the singularity at the center of the lensing potential. If, instead, the lensing potential had a non-singular core, a fifth image would form at the central extremum.

1.6 Lens Modeling

The modeling of the gravitational potential of the lensing object is a crucial step in the determination of H_0 from a gravitational lens system. In addition, a well-constrained lens model provides information about the mass distribution of the lensing object. In

this way, gravitational lenses can be used to study the properties of galaxies and clusters of galaxies at relatively high redshifts. The first step in the modeling procedure is to get the relative angular positions of the lensed images. The next is to choose a model representation of the lensing potential or, equivalently, a representation of the mass distribution in the lensing object. The parameters of the model are varied, and at each iteration the lens equation is used to compute the image positions. These are compared to the observed positions, and the model is varied accordingly. This process is continued until a good fit to the model positions is found. Note that the unobservable true source position $\vec{\beta}$ contributes two additional parameters to the model (β_x and β_y).

The representation of the gravitational potential or mass distribution of the lensing object is often a matter of personal taste because the observational constraints in many lens systems are not sufficient to distinguish between model types (e.g., Kochanek 1991). A model that is commonly used is the singular isothermal sphere (SIS). As discussed in §1.4, an isothermal sphere appears to provide a good description of the mass distribution in galaxies. The two-dimensional representation of the gravitational potential of a SIS centered at the origin of the coordinate system can be written in polar coordinates as

$$\psi(\vec{\theta}) = \psi(r, \phi) = b\, r \tag{1.30}$$

where b is the "critical radius" of the lensing object, measured in *angular* units

(Kochanek 1991). A comparison with the discussion in §1.4 reveals that

$$b = \frac{4\pi\sigma^2}{c^2}\frac{D_{\ell s}}{D_s}. \tag{1.31}$$

In many lens systems the observed image positions cannot be produced by a circularly symmetric lens. In these cases, it is necessary to introduce perturbations that break the purely symmetric nature of the lensing potential. These perturbations produce a "shear" which distorts bundles of rays passing through the gravitational potential of the lens. Kochanek (1991) presents several model potentials which contain a shear term in addition to an underlying SIS potential:

$$\psi(r,\phi) = br - \tfrac{\gamma}{2}\tfrac{b^4}{r^2}\cos 2(\phi - \phi_\gamma) \quad \text{(internal shear)} \tag{1.32}$$

$$\psi(r,\phi) = br + \tfrac{\gamma}{2}r^2\cos 2(\phi - \phi_\gamma) \quad \text{(external shear)} \tag{1.33}$$

$$\psi(r,\phi) = br + \gamma\, b\, r\cos 2(\phi - \phi_\gamma) \quad \text{(mixed shear)} \tag{1.34}$$

where γ represents the magnitude of the shear and ϕ_γ represents its position angle. Such simple representations of the lensing potential are often sufficient to reproduce the relative positions of the images (e.g., Kochanek 1991; Chapter 4 of this thesis).

The determination of H_0 with a gravitational lens system requires an accurate model of the time delay surface produced by the lensing potential. If the only constraints on the model are from the relative positions of the lensed images, there is considerable freedom in choosing a representation for the lensing potential (e.g., Kochanek 1991). Different representations can produce time delay surfaces that differ

significantly. These surfaces can produce large variations in the relative time delays predicted by the model, and therefore produce a large uncertainty in H_0. For this reason, it is necessary to have as many observational constraints as possible on the lens model. The flux density ratios of the images provide additional constraints. These constraints arise from the fact that surface brightness is conserved in the lensing process, so that the relative flux densities are proportional to the relative sizes of the images. The magnification matrix, $[\mu]$, that determines the size of each image of the lensed source is just the mapping of the source structure ($\vec{\beta}$) to the image structure ($\vec{\theta_i}$). This mapping can be expressed as a function of the second derivatives of the gravitational potential at the location of the image:

$$\mu_i = \left[\frac{\partial\vec{\theta_i}}{\partial\vec{\beta}}\right] = \left[\frac{\partial\vec{\beta}}{\partial\vec{\theta_i}}\right]^{-1} = \begin{bmatrix} 1-\frac{\partial^2\psi}{\partial\theta_x^2} & -\frac{\partial^2\psi}{\partial\theta_x\partial\theta_y} \\ -\frac{\partial^2\psi}{\partial\theta_x\partial\theta_y} & 1-\frac{\partial^2\psi}{\partial\theta_y^2} \end{bmatrix}^{-1}, \tag{1.35}$$

where $\vec{\theta_i}$ has been expressed in terms of its orthogonal components (θ_x, θ_y). If the image is unresolved, the determinant of μ_i gives the ratio of the flux density of the i^{th} image to that of the background source. Of course, the true size and brightness of the background source cannot be measured. However, if the images of the background source are resolved and it is possible to identify common features in the images, the relative magnification matrix, or transformation matrix, between the images can be determined. This matrix is the product of the inverse magnification matrix for one of the images (to reconstruct the source from the first image) and the magnification

matrix of the second (to map the reconstructed source to the second image), i.e.,

$$[\mu_{ij}] = [\mu_j][\mu_i]^{-1}. \tag{1.36}$$

Similarly, if the images are unresolved, their flux density ratios give the ratios of the determinants of their respective magnification matrices. The model of the gravitational potential must produce the correct relative image magnifications.

1.7 Using Lenses to Determine H_0

The determination of H_0 with a gravitational lens system follows straightforwardly from the presentation in the previous sections, particularly from the time-delay formalism discussed in §1.5. Consider a gravitational lens system with multiple lensed images of the background source located at angular positions $\vec{\theta}_i$. Assume that there are many observational constraints and that a model potential, $\psi(\vec{\theta})$, that satisfies all of the constraints has been found. The time delays at the image positions can then be calculated using Equation 1.27, which is reproduced here:

$$\Delta t_i = (1 + z_\ell) \frac{D_\ell D_s}{c D_{\ell s}} \left[\frac{1}{2} |\vec{\theta}_i - \vec{\beta}|^2 - \psi(\vec{\theta}_i) \right]$$

It is not possible to measure these absolute time delays because there is no undeflected ray. Instead, the observable quantities are the *relative* time delays between pairs of deflected rays, i.e.,

$$\Delta t_{ij} \equiv \Delta t_i - \Delta t_j. \tag{1.37}$$

How, then, do these delays determine H_0? Consider the observable quantities in Equation 1.27 for a lens system. They are the relative time delays (Δt_{ij}); the image positions ($\vec{\theta_i}$); and the lens and source redshifts (z_ℓ and z_s), which are contained in the angular diameter distances. The observed image positions and other observational constraints give a model of the lensing potential, which gives ψ and $\vec{\beta}$ in the equation. The remaining unknowns are the cosmological information contained in the angular diameter distances. Examining Equation 1.7, we see that

$$\frac{D_\ell D_s}{D_{\ell s}} \propto \frac{1}{H_0}. \tag{1.38}$$

Thus, for a system with a well-constrained model, both redshifts, and measured time delays,

$$H_0 = \frac{f(z_\ell, z_s, \Omega_M, \Omega_\Lambda)\{\frac{1}{2}[|\vec{\theta_i} - \vec{\beta}|^2 - |\vec{\theta_j} - \vec{\beta}|^2] - \psi(\vec{\theta_i}) + \psi(\vec{\theta_j})\}}{\Delta t_{ij}}, \tag{1.39}$$

where the function $f(z_\ell, z_s, \Omega_M, \Omega_\Lambda)$ is the ratio of angular diameter distances with the factor of H_0 extracted, i.e.,

$$f(z_\ell, z_s, \Omega_M, \Omega_\Lambda) = (1 + z_\ell)\, \frac{D_\ell D_s}{c\, D_{\ell s}}\, H_0. \tag{1.40}$$

A system with more than two images of the background source can produce an estimate of H_0 for each independent pair of images. If time delays can be measured for the independent pairs of images, these delays provide strong constraints on the lens model. The ratios of the observed time delays ($\Delta t_{ij}/\Delta t_{jk}$) are independent of H_0 (see

Table 1.1 EFFECT OF ASSUMED WORLD MODEL ON H_0 DETERMINATION USING 1608+656

Ω_M, Ω_Λ	D_ℓ (h^{-1} Mpc)	D_s (h^{-1} Mpc)	$D_{\ell s}$ (h^{-1} Mpc)	$H_0(\Omega_M, \Omega_\Lambda)/H_0(1.0, 0.0)$
(1.0, 0.0)	800	890	340	1.000
(0.1, 0.0)	920	1200	470	1.123
(0.3, 0.0)	890	1100	430	1.092
(0.1, 0.9)	1100	1500	730	1.064
(0.3, 0.7)	990	1200	550	1.070

Equation 1.27); in fact the ratios depend only on the observed image positions ($\vec{\theta_i}$) and the lens model, ($\psi(\vec{\theta})$ and $\vec{\beta}$). The model *must* correctly reproduce the observed time delay ratios, or the model is useless for any H_0 determination.

The choice of world model, $(\Omega_M, \Omega_\Lambda)$, affects the value of H_0 determined from a gravitational lens system. In general the effects are at the 5 – 15% level. As an example, I examine the effect of the choice of world model on determinations of H_0 for the lens system discussed in Chapters 3 and 5 of this thesis, 1608+656. For this system, the redshifts are $z_\ell = 0.630$ and $z_s = 1.394$. The ratio of the value of H_0 calculated in two different cosmologies is equal to the ratio of the values of f calculated in those cosmologies. I compare H_0 for several choices of world model to the Hubble Constant in an $(\Omega_M, \Omega_\Lambda) = (1, 0)$ universe. The results are in Table 1.1.

1.8 Lensing Statistics and Λ

Cosmologies with large values of Ω_Λ produce a larger comoving volume per unit redshift at high redshifts than do low-Ω_Λ cosmologies (e.g., Fig. 6 of Carroll et al.

1992). If the comoving number density of possible lensing objects is constant, the probability that a high-redshift source is multiply-imaged is much higher in a high-Ω_Λ cosmology. Fukugita, Fumatse, & Kasai (1990) and Turner (1990) realized that this fact could be used to place observational limits on Λ. Their method involves the measurement of the empirical probability that a source at a given redshift is lensed and comparing this value to the predicted probabilities for different cosmologies. The empirical lensing probability is measured by deriving the lensing rate in a survey for lenses. This rate is combined with the redshift distribution of the survey sources to give a lensing probability (expressed as an optical depth to lensing) as a function of source redshift.

The predicted optical depth is derived from models of the lensing objects (assumed to be galaxies), which give their cross sections to lensing. The comoving number density of the lensing objects is assumed to be constant, so it suffices to derive the number density of lenses at the present time (n_0) and then use the relationship $n(z) = n_0\,(1+z)^3$. The differential optical depth at a redshift z is thus

$$\begin{aligned} d\tau &= n(z)\,\sigma_x\,\frac{c\,dt}{dz}\,dz \\ &= n_0\,(1+z)^3\,\sigma_x\,\frac{c}{H_0}\,\frac{1}{(1+z)}\,\frac{dz}{[\Omega_M(1+z)^3+\Omega_k(1+z)^2+\Omega_\Lambda]^{1/2}} \end{aligned} \tag{1.41}$$

where σ_x is the lensing cross section. At this point, a model for the mass distribution in the lensing galaxies needs to be chosen so that σ_x can be computed. Often a singular or softened isothermal sphere is used. For the choice of a singular isothermal

sphere, for example, a background source will form multiple images if the source position lies within the Einstein ring radius of the lens. The lensing cross section is thus

$$\sigma_x = \pi(D_\ell \theta_E)^2 = \pi\, D_\ell^2 \left(\frac{4\,\pi\, D_{\ell s}\, \sigma^2}{c^2\, D_s} \right)^2 \tag{1.42}$$

(see Equation 1.19) and the differential optical depth becomes

$$d\tau = 16\pi^3 n_0 \left(\frac{\sigma}{c}\right)^4 \left(\frac{D_\ell D_{\ell s}}{D_s}\right)^2 \frac{c}{H_0} (1+z)^2 \frac{dz}{[\Omega_M (1+z)^3 + \Omega_k (1+z)^2 + \Omega_\Lambda]^{1/2}} \tag{1.43}$$

(e.g., Turner, Ostriker, & Gott 1984; Fukugita et al. 1992). Note that σ now represents the velocity dispersion in the lensing galaxy. Values for n_0 and σ come from relations derived from observations of nearby galaxies. The basic approach is to assume the present number density of lensing galaxies is described by a Schechter function, which gives a differential number density as a function of luminosity (Schechter 1976). Different forms are used for E/S0 galaxies and spirals, and the observed relative numbers of each galaxy type have to be included in the analysis. The Faber-Jackson (Faber & Jackson 1976) or Tully-Fisher (Tully & Fisher 1977) relationship is used to convert galaxy luminosities into velocity dispersions. For each choice of the background source redshift, the differential optical depth is integrated over all possible values of lens luminosity and redshift, giving the predicted optical depth as a function of source redshift for each chosen cosmology.

More sophisticated treatments expand on the above simple methodology by including estimates of selection and magnification biases, accounting for inhomogeneous universes, and using more realistic models of galaxy mass distributions (e.g., Fukugita & Turner 1991; Fukugita et al. 1992; Kochanek 1993; Maoz & Rix 1993; Kochanek 1996). Recent papers which include the more thorough analyses of lensing statistics yield upper limits on Ω_Λ in the range $0.6 - 0.7$ for an $\Omega_M + \Omega_\Lambda = 1$ cosmology (Kochanek 1996; 1998).

Radio surveys for lenses are free from many of the problems associated with optical surveys such as biases introduced by extinction or poor angular resolution. For this reason, they can potentially place stronger limits on Λ than the optical surveys. However, the use of these surveys is limited by the poorly known redshift distribution of the parent samples. To address this deficiency, Falco, Kochanek, & Muñoz (1998) have started an observational program to measure the redshift distribution of representative samples of the radio sources in the MIT–Green Bank (MG; Bennett et al. 1986; Langston et al. 1990; Griffith et al. 1990; Griffith et al. 1991) survey and Jodrell-VLA Astrometric Survey (JVAS; Patnaik et al. 1992b; Browne et al. 1998; Wilkinson et al. 1998). My collaborators and I are conducting similar observations in order to use the lensing rate from the Cosmic Lens All-Sky Survey (CLASS; Myers et al. 1998; see also Chapter 2 of this thesis) to place limits on Λ. This CLASS sample contains sources which are

fainter than the MG and JVAS samples.

1.9 Thesis Overview

As described in this chapter, gravitational lenses can provide a powerful tool for studying galaxy structure and cosmology. The remainder of this thesis describes CLASS and two of the new gravitational lens systems discovered in the survey. Chapter 2 gives an overview of the survey. Chapters 3 – 4 are composed of three self-contained papers (two of them in Chapter 3) describing the lenses 1608+656 and 2045+265. Chapter 5 describes the measurement of time delays in the 1608+656 system and the resulting determination of H_0. Chapter 6 summarizes the material covered in this thesis.

REFERENCES

Bennett, C. L., Lawrence, C. R., Burke, B. F., Hewitt, J. N., & Mahoney, J. 1986, ApJS, 61, 1

Blandford, R. & Narayan, R., 1986, ApJ, 310, 568

Blandford, R. D. & Kochanek, C. S., in *Dark Matter in the Universe*, eds. J. Bahcall, T. Piran, & S. Weinberg, (Singapore: World Scientific), p. 133

Blandford, R. D. & Narayan, R. 1992, ARA&A, 30, 311

Browne, I. W. A., Patnaik, A. R., Wilkinson, P. N., & Wrobel, J. M. 1998, MNRAS, 293, 257

Byun, Y.-I., Grillmair, C. J., Faber, S. M., Ajhar, E. A., Dressler, A., Kormendy, J., Lauer, T. R., Richstone, D., & Tremaine, S. 1996, AJ, 111, 1889

Carroll, S. M., Press, W. H., & Turner, E. L. 1992, ARA&A, 30, 499

Chwolson, O., Astron. Nachrichten, 221, 329

Dyson, F. W., Eddington, A. S., & Davidson, C. R. 1920, Mem. RAS, 62, 291

Eddington, A. S. 1920, *Space, Time, & Gravitation* (Cambridge: Cambridge University Press)

Fabbiano, G. 1989, ARA&A, 27, 87

Faber, S. M. & Jackson, R. E. 1976, ApJ, 204, 668

Falco, E. E., Kochanek, C. S., & Muñoz, J. A. 1998, ApJ, 494, 47

Fukugita, M., Futamase, T., & Kasai, M. 1990, MNRAS, 246, 24P

Fukugita, M. & Turner, E. L. 1991, MNRAS, 253, 99

Fukugita, M., Futamase, T., Kasai, M., & Turner, E. L. 1992, ApJ, 393, 3

Gebhardt, K., Richstone, D., Ajhar, E. A., Lauer, T. R., Byun, Y.-I., Kormendy, J., Dressler, A., Faber, S. M., Grillmair, C., & Tremaine, S. 1996, AJ, 112, 105

Griffith, M., Heflin, M., Conner, S., Burke, B., & Langston, G. 1991, ApJS, 75, 801

Griffith, M., Langston, G., Heflin, M., Conner, S., Lehár, J., & Burke, B. 1990, ApJS, 74, 129

Grogin, N. A. & Narayan, R. 1996, ApJ, 464, 92

Helbig, P. & Kayser, R. 1996, A&A, 308, 359

Hewitt, J. N., Turner, E. L., Schneider, D. P., Burke, B. F., & Langston, G. 1988, Nature, 333, 537

Impey, C., Falco, E., Kochanek, C., Lehár, J., McLeod, B., Rix, H.-W., Peng, C., & Keeton, C. 1998, ApJ, submitted (astro-ph/9803207)

Jauncey, D. L., Reynolds, J. E., Tzioumis, A. K., Murphy, D. W., Preston, R. A., Jones, D. L., Meier, D. L., Hoard, D. W., Lobdell, E. T., & Skjerve, L. 1991, Nature, 352, 132

King, L. J., Jackson, N., Blandford, R. D., Bremer, M. N., Browne, I. W. A., De Bruyn, A. G., Fassnacht, C., Koopmans, L., Marlow, D., Wilkinson, P. N. 1998, MNRAS, 295, L41

Kochanek, C. S. 1991, ApJ, 373, 354

Kochanek, C. S. ApJ, 384, 1

Kochanek, C. S. 1993, ApJ, 419, 12

Kochanek, C. S. 1995, ApJ, 445, 559

Kochanek, C. S. 1996, ApJ, 466, 638

Kochanek, C. S., Falco, E. E., Impey, C. D., Lehár, J., McLeod, B. A., Rix, H.-W., Keeton, C. R., & Peng, C. Y. 1998, ApJ, submitted (astro-ph/9809371)

Langston, G. I., Heflin, M. B., Conner, S. R., Lehár, J., Carrilli, C. L., & Burke, B. F. 1990, ApJS, 72, 621

Langston, G. I., Schneider, D. P., Conner, S., Carilli, C. L., Lehár, J., Burke, B. F., Turner, E. L., Gunn, J. E., Hewitt, J. N., & Schmidt, M. 1989, AJ, 97, 1283

Lehár, J., Langston, G. I., Silber, A., Lawrence, C. R., & Burke, B. F. 1993, AJ, 105, 847

Lehár, J., Burke, B. F., Conner, S. R., Falco, E. E., Fletcher, A. B., Irwin, M., McMahon, R. G., Muxlow, T. W. B., & Schechter, P. L. 1997, AJ, 114, 48

Maoz, D. & Rix, H.-W. 1993, ApJ, 416, 425

Myers, S. T., et al. 1998, in preparation

Narayan, R. & Bartelmann, M. 1998, in *Formation of Structure in the Universe* eds. A. Dekel & J. P. Ostriker (New York: Cambridge University Press)

Patnaik, A. R., Browne, I. W. A., King, L. J., Muxlow, T. W. B., Walsh, D., & Wilkinson, P. N. 1992a, MNRAS, 261, 435

Patnaik, A. R., Browne, I. W. A., Wilkinson, P. N., & Wrobel, J. M. 1992b, MNRAS, 254, 655

Peebles, P. J. E. 1993, *Principles of Physical Cosmology* (Princeton: Princeton University Press)

Refsdal, S. 1964, MNRAS, 128, 307

Schechter, P. 1976, ApJ, 203, 297

Schneider, P., Ehlers, J., & Falco, E. E. 1992, *Gravitational Lenses*, (New York: Springer-Verlag)

Schutz, B. F. 1990, *A First Course in General Relativity* (Cambridge: Cambridge University Press)

Tully, R. B. & Fisher, J. R. 1977, A&A, 54, 661

Turner, E. L., Ostriker, J. P., & Gott III, R. 1984, ApJ, 284, 1

Turner, E. L. 1990, ApJ, 242, L135

Walsh, D., Carswell, R. F., & Weymann, R. J. 1979, Nature, 279, 381

Wilkinson, P. N., Browne, I. W. A., Patnaik, A. R., Wrobel, J. M., & Soratia, B. 1998, MNRAS, in press

Zwicky, F., 1937, Phys. Rev. Lett., 51, 290

Chapter 2

CLASS

2.1 Introduction

As described in Chapter 1, investigations of gravitational lenses can be used to determine cosmological parameters such as H_0 and Λ. At the beginning of the 1990's, however, the true potential of gravitational lenses as tools to study the Universe still had not been realized. Statistical studies of lenses suffered from the small number of known lenses and from the heterogeneous nature of the surveys in which they had been found. Only one lens, 0957+561, had provided a determination of H_0, and even that value was a matter of considerable debate. The advantages of conducting a large, systematic search for gravitational lenses were apparent. As a result, the Cosmic Lens All-Sky Survey (CLASS) was started. This chapter provides an overview of the CLASS project.

2.2 Overview and Scientific Motivation

The CLASS project is a collaboration between Caltech, Jodrell Bank, the University of Pennsylvania, the Netherlands Foundation for Research in Astronomy, and the Kapteyn Astronomical Institute. The survey is being conducted at radio wavelengths with the Very Large Array (VLA). The ultimate aim of the survey is to observe a sample of 14,000 flat-spectrum radio sources, which is expected to produce approximately 15 – 20 new gravitational lenses. Already 12 new lenses have been discovered in CLASS (§2.8). This yield represents a significant contribution to the population of known lenses. An up-to-date lens list (CASTLeS web page; Kochanek et al.) contains only 27 non-CLASS systems in the "probable lens" category (which also includes confirmed lenses).

The CLASS project has the following major objectives:

1) To Find Lenses Appropriate for Measuring H_0. When CLASS began in 1994, only one gravitational lens system, 0957+561(Walsh et al. 1979), had provided data from which H_0 could be determined. However, this value was controversial due to the difficulties in measuring the time delay and modeling the gravitational potential of the lens, which includes a substantial and unknown contribution from the host cluster (see Haarsma et al. 1997 for a summary of the history of the 0957+561 situation). Recently, the time delay controversy has been settled (Kundić et al. 1995; Kundić et al. 1997a; Oscoz et al. 1997); however, the modeling

of the system still presents difficulties due to the contribution of the cluster of galaxies (e.g., Barkana et al. 1998). One of the major goals of CLASS is to find "golden lenses" which are free from the problems associated with the 0957+561 system. These systems have the following characteristics: (1) the gravitational potential of the lens is dominated by the lensing galaxy, making the modeling more straightforward; (2) the source and lens redshifts are known, so angular measurements can be converted into physical units for the lens model; and (3) the background source is variable, so that time delays can be measured and combined with the lens model to provide a determination for H_0. The CLASS observing strategy is designed to maximize the chances of finding golden lenses. The high angular resolution of the CLASS observations allows the detection of systems in which the images of the background source are split by $\sim 1''$. Isolated massive galaxies will split images by this amount for typical lens and source redshifts (Equation 1.17). Thus, CLASS is sensitive to single galaxy masses. In addition, the survey sample is drawn from a population of typically variable sources (§2.3) to increase the chances of measuring time delays in the newly discovered lenses.

2) To Use the Lensing Rate to Place Limits on Λ. As discussed in the previous chapter, it is possible to use rates of gravitational lensing to place limits on Λ. In order to perform the necessary calculations, it is best to derive the lensing rate from a large, homogeneously selected sample. The homogeneous selection of sources

aids in the determination of the properties of the parent sample such as its redshift distribution. Ideally, the survey will also produce a large number of lenses. Before CLASS, attempts to place limits on Λ with available quasar samples suffered because the number of lenses in the samples were small. Hence, the statistical uncertainties in the derived lensing rates were large and could not be used to distinguish between different cosmologies (e.g., Kochanek, Falco, & Schild 1995). An additional complication arises if the limit on Λ is derived from an optical survey. In these surveys, the lensing rate can be underestimated easily because of two factors which may cause a lens system to escape detection. Atmospheric seeing can blur together lensed images at small separations, and extinction from dust can effectively demagnify one lensed image with respect to the other(s) and hide the multiply-imaged nature of the system. Radio surveys conducted with interferometric arrays can avoid both of these problems by providing high angular resolution images at wavelengths at which dust extinction is negligible.

3) To Study the Properties of Galaxies at Intermediate Redshifts. Gravitational lenses provide a unique tool for studying the properties of galaxies at the typical lens redshifts of $z \sim 0.4 - 1$. The image splittings and system redshifts give a direct and model-independent estimate of the mass of the lensing galaxy inside the Einstein ring radius. Broadband colors of the lens can be combined with

the mass determination to search for evolution in the mass-to-light ratios of galaxies. In addition, the lensing galaxy can be studied in absorption if the background source is an optically bright quasar. With a large sample of lenses the incidence of dust in galaxies at these redshifts can be studied. Evidence for dust has already been detected in several lens systems (e.g., Larkin et al. 1994; Lawrence et al. 1995; McLeod et al. 1998; Malhotra et al. 1997; Jackson et al. 1997). Note, however, that a recent paper by Kochanek et al. (1998) argues that the red colors in these systems are intrinsic to the background sources and are not due to the presence of dust in the lenses. Finally, because radio-selected lens systems are unbiased with respect to optical luminosity, the CLASS results can be used to search for evidence of "dark lenses," galaxy-mass-sized concentrations of matter with little or no associated optical emission (e.g., Hawkins et al. 1997).

4) To Find Phase Calibrators for High Resolution Radio Observations. The sources that serve as the survey sample for CLASS produce emission that is dominated at the wavelengths of the survey by the compact flat-spectrum core. The CLASS observations provide positions for the compact cores that have an RMS accuracy of $\sim$20 milliarcseconds (mas). The unlensed CLASS sources, which make up almost the entire survey sample, provide a database of compact sources with accurate positions. These sources can be used to determine antenna gain solutions, an important step in calibrating interferometer data. The solutions determined from

such calibrators are applied to the target source data. The quality of the interpolated solutions decreases as the distance between the calibrator and the target source increases. Thus, it is desirable to have the calibrator be as close as possible to the target source. The CLASS database augments existing lists of calibrator sources and increases the density of such sources on the sky. In addition, a large sample of flat-spectrum radio sources with accurate positions has other uses. For example, the sample can be used to make optical identifications of radio sources and to study active galactic nuclei.

2.3 Flat-spectrum Radio Sources as the Parent Sample

The CLASS sample consists of flat-spectrum radio sources. This subset of radio sources is chosen to maximize the chances of finding golden lenses and to provide clean statistics for placing limits on Λ. Flat-spectrum sources provide several advantages as a population in which to search for lenses. First, it is easy to recognize lens systems. Emission from these sources tends to be dominated by their flat-spectrum cores which will be unresolved by the VLA at the wavelengths of the survey. Any systems in which multiple images of the source are formed will stand out clearly from the vast majority of objects in the survey which will show only a point source. In

contrast, steep-spectrum radio sources often exhibit extended structures which may be difficult to distinguish from a true signature of multiple imaging. The ease of selecting good lens candidates speeds the analysis of the survey results (e.g., §2.5.3). Second, it is relatively straightforward to calculate lensing optical depths when the background source is compact. On the other hand, optical depths for extended sources depend strongly on the size of the source, which makes placing limits on Λ more difficult (Kochanek & Lawrence 1990). Third, only a small amount of time is needed to detect the sources because their compact nature implies relatively high surface brightnesses. With the flux density range of the sources chosen for the sample and the sensitivity of the VLA, only 30 sec of integration time is needed per source observed. This means that large numbers of sources can be observed very quickly. Fourth, by conducting the survey at radio wavelengths, no lenses should be lost to extinction or atmospheric seeing. Finally, flat-spectrum radio sources are often variable (e.g., Kellerman & Pauliny-Toth 1981), the necessary characteristic for the measurement of time delays.

2.4 Source Selection

The CLASS search differs from previous surveys for lenses at radio wavelengths. Unlike the lens search (Hewitt et al. 1988) based on the MIT-Green Bank Survey (MG; Bennett et al. 1986; Langston et al. 1990; Griffith et al. 1990; Griffith et al. 1991),

which imposes no spectral selection of sources, the CLASS sample consists of flat-spectrum radio sources only. The CLASS sample differs from the similar Jodrell-VLA Astrometric Survey (JVAS; Patnaik et al. 1992; Browne et al. 1998; Wilkinson et al. 1998) sample in that its lower flux density limit is fainter. The JVAS sample contains sources with $S_{5GHz} > 200$mJy, whereas the CLASS flux density limit is $S_{5GHz} > 30$mJy. As a result, the number of sources in the CLASS sample is a factor of four to five times larger than the number of JVAS sources. Other than the flux density cutoff, however, the CLASS and JVAS selection criteria are nearly identical. Thus, the combined CLASS+JVAS sample can be considered as a single survey of $\sim$16,000 sources.

The CLASS sources are selected from the updated 5 GHz Green Bank survey (GB6; Gregory et al. 1996), which provides more accurate positions and flux densities than the earlier 87GB catalog generated from the same observations (Gregory & Condon 1991). The initial selection criteria are $S_{5GHz} \geq 30$ mJy and $|b| > 10°$. The application of these criteria produces a list of sources with a wide range of spectral characteristics. To select the flat-spectrum sources from this list, we calculate a two-point spectral index, α, for each source, where α is defined such that $S_\nu \propto \nu^\alpha$. Only sources with $\alpha \geq -0.5$ are chosen. The spectral indices are calculated using the GB6 flux density and the flux density from the 1.4 GHz NRAO VLA Sky Survey (NVSS; Condon et al. 1998). Sources which have been observed in other lens

surveys (JVAS, MG, etc.) are excluded, effectively placing an upper flux density limit of 200 mJy on the CLASS sample. There are ~13,000 sources matching the spectral index, flux density, and position criteria, of which only ~700 remain to be observed.

In the early phases of the survey, neither the complete NVSS list nor the updated version of the 5 GHz catalog were available. As such, the 5 GHz selection was made from the 87GB catalog. The spectral index calculations were performed using flux densities from either the 325 MHz Westerbork Northern Sky Survey (WENSS; Rengelink et al. 1997) or the 365 MHz Texas Interferometer Survey (Douglas et al. 1996), neither of which cover the entire area observed by CLASS. Now that both the GB6 and NVSS lists are available, it is possible to produce a sample with uniform spectral characteristics over the entire northern sky. In the areas of the sky observed by the early phases of CLASS, some of the observed sources have dropped out of the sample because they do not satisfy the new spectral criterion. On the other hand, new sources in the previously observed areas have been added to the sample. A significant fraction of the most recent phase of observations was spent observing these new sources so that a homogeneous parent sample for use in converting lensing rates into constraints on Λ could be constructed.

2.5 Observations and Data Reduction

2.5.1 Observations

The survey has been conducted in three main phases: CLASS1 in the spring of 1994, CLASS2 in the late summer of 1995, and CLASS3 in the spring of 1998. Each phase was split into sub-phases due to differences in source selection techniques (CLASS1) or a significant separation in observing dates (CLASS2 and CLASS3). The observing dates and number of sources observed are listed in Table 2.1. The observations were made with at 8.4 GHz with the VLA in A configuration, giving angular resolutions of ~ 0.2 arcsec. Two intermediate frequencies (IFs) at 8.4149 and 8.4649 GHz (CLASS1 and CLASS2), or 8.4351 and 8.4851 (CLASS3) were used. Target sources with accurate positions determined from NVSS or WENSS observations were observed with IF bandwidths of 50 MHz for higher sensitivity. Sources with positions taken from the Texas Survey had less accurate positions due to occasional problems with lobeshifting (Douglas et al. 1996). As a result, those sources were observed with 25 MHz bandwidths for a wider effective field of view.

The observing strategy for each session was the same. Each target source was observed for 30 sec. Observations of phase calibrators chosen from the JVAS source list were interjected after every 13 or 14 target sources, and a flux density calibrator (3C 286 or 3C 48) was observed at least once per observing session. Including the time

Table 2.1 SUMMARY OF CLASS OBSERVATIONS

Phase	Date(s)	Sources Observed	Comments
1a	1994 Feb – Apr	2574	Texas-selected
1b	1994 Feb – Apr	683	WENSS-selected
2a	1995 August	2352	WENSS-selected
2b	1995 September	2132	WENSS/Texas-selected
3a	1998 March	2357	NVSS-selected
3b	1998 April	2078	NVSS-selected
3c	1998 May	662	NVSS-selected

taken for slewing and for the calibration observations, the average observing rate was approximately one target source per minute.

2.5.2 Calibration

The data are calibrated using the Astronomical Image Processing System (AIPS) developed by the National Radio Astronomy Observatory. The absolute flux density scale is set with the SETJY task and then the TVFLG task is used to assess data quality and to flag bad visibilities. Observations of the flux density and phase calibrators are used to find antenna-based gain solutions with the CALIB task. The solutions are then interpolated and applied to the survey source data with the CLCAL task. These tasks make up the "standard AIPS routines" described in many of the following chapters in this thesis. The data are not mapped in AIPS, but are processed using the automatic mapping routine described in the next section.

2.5.3 Automapping

The time needed to map the sources is drastically reduced through use of an automatic mapping procedure written in the scripting language available in the DIFMAP package (Shepherd 1997). The basic "automapping" procedure is to search for peaks of emission in a large field ($\sim 4' \times 4'$) and then to examine a smaller field centered on each peak at higher resolution. A map of the emission in each smaller field is made with the DIFMAP implementations of the CLEAN algorithm (Högbom 1974) and self-calibration routines. Cutoff levels are chosen to maximize the probability that the peaks found in the large and small maps are real emission and not noise spikes. The CLEANed map for each source is plotted and used in the lens candidate selection process. In addition to making maps via CLEANing, the automapping procedure also determines source information by placing Gaussian components at the peaks of emission found in the mapping procedure and then varying the component parameters to achieve the best fit to the (u, v) plane visibility data. This process is conducted with the `modelfit` function in DIFMAP. The positions, sizes, and flux densities of the model components for each source are recorded in an output file which is used in the automatic lens candidate selection described in the next section. Figure 2.1 shows a flowchart describing the steps of the automapping procedure. The most recent version of the automapping script can be found at `http://dept.physics.upenn.edu/~myers/class/automap`.

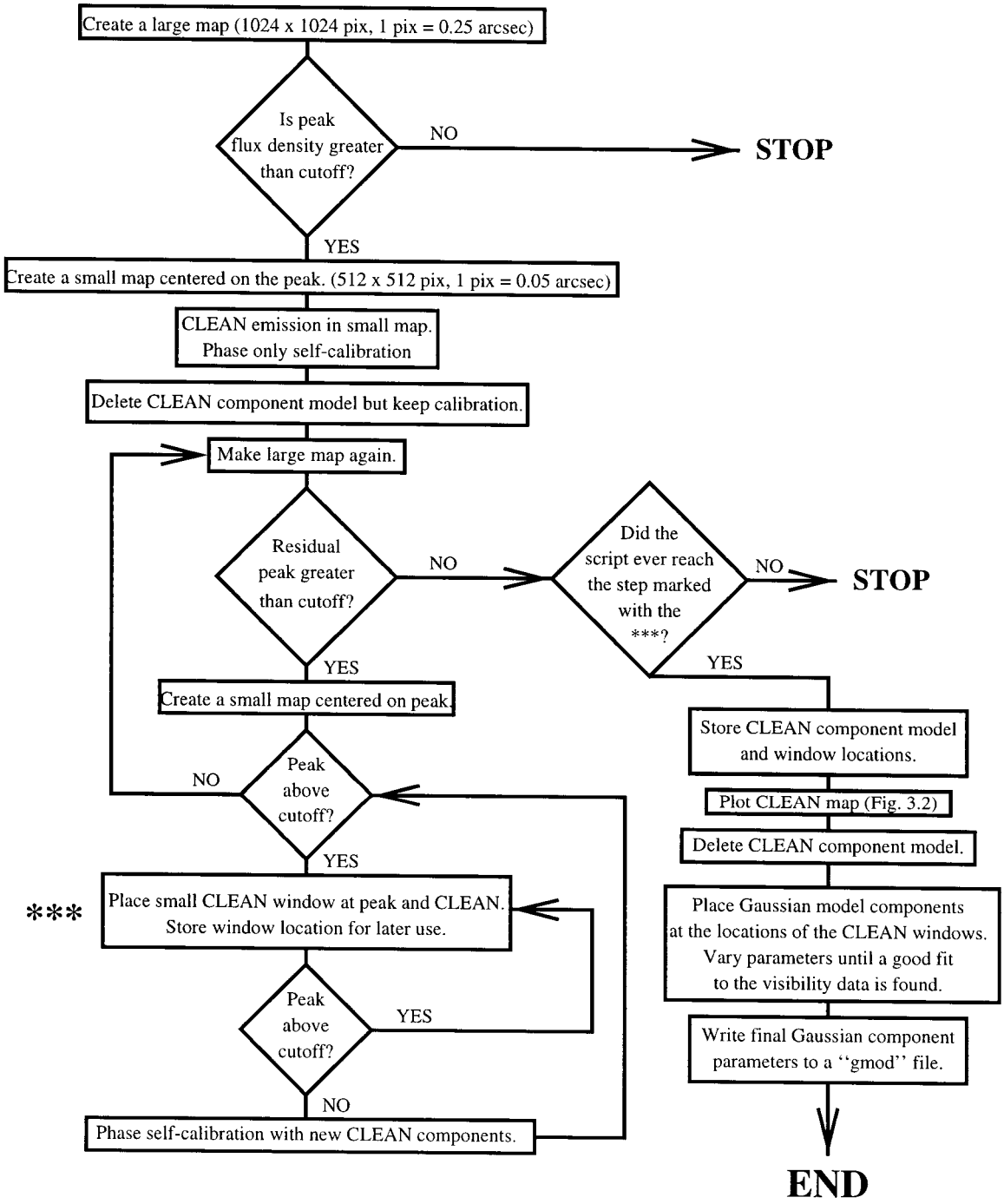

Figure 2.1 Flow chart describing CLASS automatic mapping script.

This procedure works extremely well due to the nature of the sources observed. The sources are compact, and any multiple images produced by gravitational lensing should also be compact. The maps should show little, if any, diffuse emission. As a result, the search for isolated peaks of emission carried out by the above algorithm is effective in producing good maps. In addition, the sources are relatively weak and so strong sidelobes are rarely a problem in the mapping. To test the procedure, several sources were mapped both with the automapping procedure and by hand. In all of the test cases, there were no significant differences in the resulting maps. Furthermore, the automatic mapping is fast. After the initial development of the mapping script, the 2574 sources in CLASS1a were mapped in 5 days on a Sparc 10 workstation. At the time of the CLASS2 and CLASS3, the data were mapped *during* the observing session. Thus, any promising lens candidates discovered early in the session could be reobserved later in the session with longer integration times and at a second frequency for spectral information.

A typical page of output from the automapping procedure is shown in Fig. 2.2. As expected, the majority of the maps are dominated by emission from a compact component, with no other components visible. Typical RMS noise levels in the final maps are $\sim$0.4 mJy/beam.

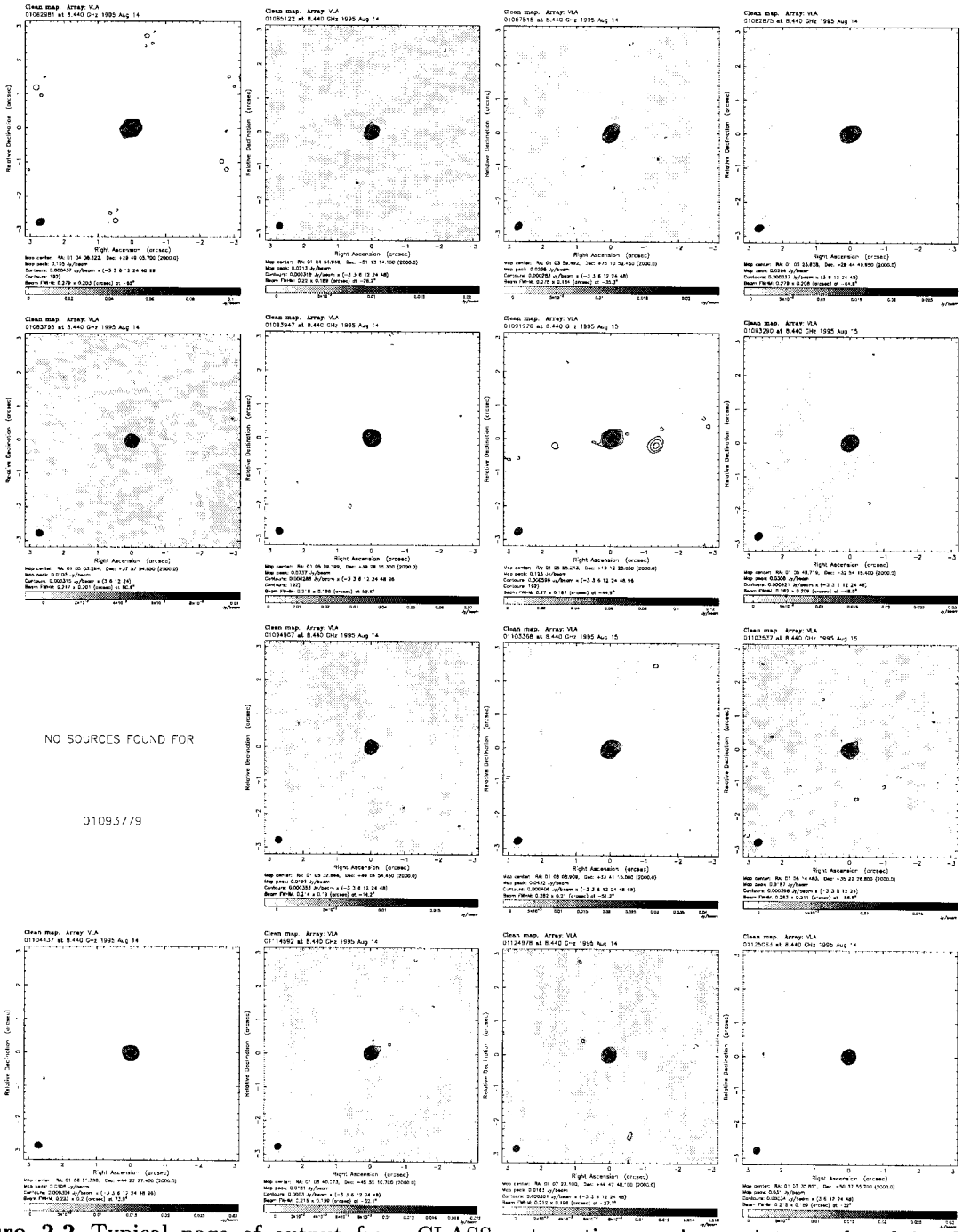

Figure 2.2 Typical page of output from CLASS automatic mapping script, produced in the CLASS2a data reduction. Note that almost all of the sources are dominated by a single compact component.

2.6 Candidate Selection

After the automapping process is complete, the results are examined in order to select a list of gravitational lens candidates. The selection is aided by the simple morphology of the survey sources. The vast majority (>95%) of the output maps show a single, compact object and are quickly rejected as lens candidates. On the other hand, any source with multiple components stands out quite clearly from the rest of the sample and is selected as a lens candidate.

Two parallel and complementary methods are used to select the lens candidates from the automapping output. All the maps are examined by members of the CLASS collaboration, and candidates are selected by eye (the "pundit" selection method). This method is especially effective in distinguishing lensing geometries from typical sidelobe patterns in sources with more than two components. The pundit method is also effective in identifying the cases in which weak extended emission may be indicative of lensing. The other method is an automated candidate selection program that I have developed. It selects candidates based on the parameters generated by the model fitting routine in the automapping. This method, described in detail below, has the advantage of applying objective selection criteria to all of the sources. In addition, it is effective in finding lens candidates with high flux density ratios between the components and systems in which the component separations are either very small (<250 mas) or large (>12″). The two selection methods complement each other well.

The majority of lens candidates are selected by both methods, but there are some systems which are found by only one of the methods. The final lens candidate list is the union of the lists produced by the two selection methods.

The automatic candidate selection program queries the model parameter files produced by the automapping procedures. A separate file is queried for source spectral indices derived from other surveys. The component sizes, separations and flux densities, as well as the overall radio spectra of the sources, are used to rank each candidate. The spectral ranking procedure now uses the NVSS – GB6 spectral index; if the NVSS data for a particular source are not yet available, the WENSS – GB6 spectral index is used. Four lists of candidates are produced by the program: the arcsecond-separation candidates that CLASS has been designed to find, large separation candidates (separations $>12''$), compact double candidates (two components separated by <250 mas), and possible very compact doubles (one component that has a flat spectrum but is extended). For the purposes of this program, a "compact" component is one with a major axis smaller than 170 mas; any larger component is considered "extended." The program evaluates each source in turn, first rejecting any source which meets any of the following criteria:

1. There is only one component. (However, if the source has a flat spectrum and is extended, consider it to be a very compact double candidate).

2. There are multiple components, but only one is compact.

Table 2.2 CRITERIA FOR AUTOMATIC CANDIDATE SELECTION

Criterion	Points
More than 2 compact components	10
All components have $S_{8.4} > 5$mJy	7
Spectral index greater than -0.4	6
Spectral index between -0.6 and -0.4	3
Flux ratio between 2 brightest components less than 2.5:1	3
At least 30 mJy in compact components	2

3. The flux density ratio between the two brightest components is extreme (>15:1).

4. The spectral index is $\alpha_{NVSS}^{GB6} < -0.8$. These sources were included in the survey before NVSS data were available and appeared to have flat spectra from other surveys.

5. The total 8.4 GHz flux density is <20 mJy.

The small number of sources that pass these criteria have point scores assigned based on the criteria in Table 2.2. The points for each candidate are totaled and used to assign ranks to the candidates. *All* of the lens candidates are reobserved to determine if they are lenses; the rankings are only used to assign priorities in the case of limited observing time. The sources most likely to be lenses are observed first and, if confirmed, can be subjected to further observation quickly.

An example of the output of the automatic candidate selection is given in Table 2.3. The grades given to each source are assigned as follows: A ($\geq$15 points), B (10 – 14), C (6 – 9), D (1 – 5). Each phase (1, 2, or 3) of the survey typically produces 30 – 80 lens candidates from the combined automatic and "pundit" selection

methods. These candidates are all subjected to the further observations described in §2.7.

2.6.1 Tests of the Pipeline Processing

As a test of the automated processing procedures, several known lenses were observed in CLASS2b, including lenses found in JVAS, the MG survey, and earlier phases of CLASS. The automapping produced adequate maps of all of the lenses, and all were easily selected as lens candidates by the "pundit" method[1]. The automatic candidate selection did nearly as well, only missing the JVAS lens 1938+666 (because the arcs appear to be extended components at the resolution of the VLA; see King et al. 1997 for the radio maps) and the CLASS lens 0712+472 (because the weak fourth component was not detected in the short integration and the two brightest components were modeled as one extended component; see Jackson et al. 1998b). It should be noted again that in each case the lensing nature of the system was obvious to the pundits, showing the benefits of having the parallel candidate selection methods.

[1]The inclusion of these systems led to some violent emotional swings as the maps came off the printer. The known lenses were mapped in the order that they were observed and thus randomly printed on pages full of CLASS sources. The elation that we felt at seeing each excellent lens candidate was quickly extinguished as we realized that it was one of the known lenses and not a new lens discovered by CLASS.

Table 2.3 OUTPUT OF AUTOMATIC CANDIDATE SELECTION FOR CLASS2A

Gravitational Lens Candidates

Source	Rank	Score	α	$N_{compact}$	S_{peak}	Ratio	Sep.	Shift($''$)
00164902	B	12	−0.41	2	44.5	7.5	1.13	2.0
03321875	C	9	−0.60	2	31.2	4.9	0.32	2.9
04602636	B	10	−0.62	2	18.0	1.8	0.98	2.9
07464077	A	16	−0.31	2	17.3	2.3	0.62	0.7
07513335	A	15	−0.02	2	363.3	4.4	0.56	9.1
08204068	B	12	−0.41	2	70.8	10.0	0.86	1.2
08515242	A	15	−0.35	2	24.3	2.7	2.82	3.3
08934959	A	15	−0.28	2	36.0	5.1	0.27	1.2
09204143	B	12	−0.47	2	170.0	13.1	1.89	1.5
10993140	C	9	−0.65	2	104.1	5.9	0.49	0.7
11503820	A	16	−0.01	2	14.7	1.2	0.70	25.5
15953736	A	15	−0.19	2	36.1	3.8	0.39	2.0
19474210	C	8	−0.42	2	16.6	1.0	0.47	1.9
22332646	A	15	+0.64	2	76.1	7.0	2.84	3.0

Large Separation Double Candidates

Source	Rank	Score	α	$N_{compact}$	S_{peak}	Ratio	Sep.	Shift($''$)
07863392	A	15	+0.19	2	692.3	12.8	31.16	7.7
08355506	B	13	−0.50	2	10.3	1.6	40.40	0.8
10963715	A	15	−0.05	2	103.6	6.2	45.49	35.3

Compact Double Candidates

Source	α	$N_{compact}$	S_{peak}	Ratio	Sep.	Shift($''$)
01824802	−0.46	2	29.6	1.4	0.17	0.3
18434404	−0.44	2	71.8	7.1	0.24	2.3

Very Compact Double Candidates

Source	α	S	Size (mas)	Shift($''$)
00712095	−0.39	90.1	141	2.5
01125246	−0.49	24.3	169	3.0
01944499	−0.46	29.1	108	4.3
02753486	+0.16	31.0	109	26.5
03184008	+0.04	29.9	110	17.3
03283970	+0.06	48.0	111	8.1
03423354	−0.39	35.6	123	13.3
03874049	−0.32	44.9	130	29.7
06963803	−0.43	25.3	108	0.6
07002993	+0.87	26.9	110	29.9
07173007	−0.45	44.6	101	28.0
07334281	−0.47	25.9	246	4.9
07692863	+0.31	30.3	111	29.7
07863508	+0.08	48.3	105	2.5
10903142	+0.08	27.0	119	28.4
11194522	−0.42	27.1	173	2.4
... and so on ...				

2.7 Further Observations of Lens Candidates

2.7.1 High-Resolution Radio Images

The first step in the evaluation of the lens candidates is a radio observation at higher angular resolution. The reason for pursuing this path is that components which appear compact to the VLA may be resolved by the higher resolution observations. If a source consists of multiple compact components in the VLA maps, but the higher resolution observations show that the components have different surface brightnesses or drastically different morphologies, the candidate is rejected. The candidate is also rejected if its components have significantly different radio spectra. The followup radio observations are made with the Multi-Element Radio-Linked Interferometer Network (MERLIN), an array of six radio telescopes with a maximum baseline of 217 km run by the Nuffield Radio Astronomy Laboratory at Jodrell Bank, England. The observations are conducted at 1.66 and 5 GHz, giving resolutions of $\sim$120 and $\sim$50 mas, respectively. Observations at the two frequencies allow two-point spectral indices to be calculated for the individual components. An example of a rejected candidate is shown in Fig. 2.3. The source was selected as a candidate because it has two compact components of nearly equal flux density. The MERLIN image reveals that one of the components remains unresolved and has high surface brightness, while the other component is resolved and has lower surface brightness. The object is a

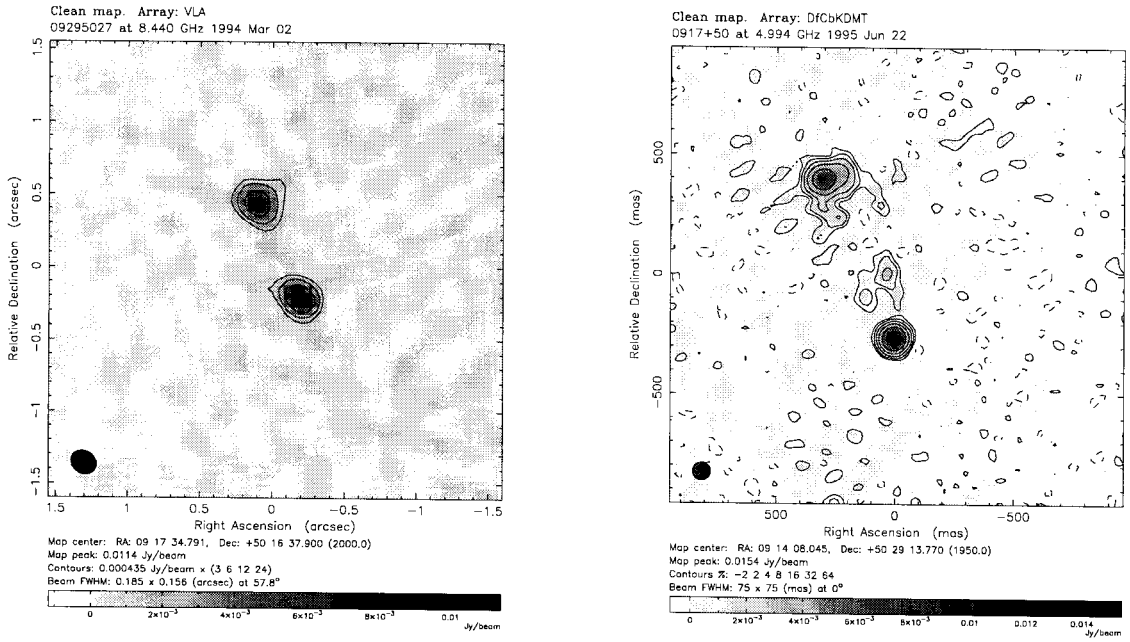

Figure 2.3 Example of the use of high angular resolution radio images to evaluate lens candidates. The VLA image (left) shows two compact components while the MERLIN image (right) reveals the object to be a "core-jet" source. This object is not lensed.

"core-jet" source, not a lens. The MERLIN observations are a remarkably effective filter, rejecting ~80% of the lens candidates observed. The sources that survive are strong lens candidates.

In yet another round of winnowing, these sources are observed at even higher angular resolution with the Very Long Baseline Array (VLBA). The nearly 9000 km maximum baseline gives angular resolutions of ~1 mas for observations at 5 GHz. Any objects which pass the VLBA filter are presumed to be lens systems and are observed at optical wavelengths for final confirmation.

2.7.2 Optical Imaging and Spectroscopy

All of the new lenses are imaged at optical wavelengths to provide additional confirmation of the lensed nature of the systems, to study the nature of the lensing object, and to provide additional data for modeling the gravitational potential of the lens. Both ground-based and *Hubble Space Telescope* (HST) multicolor imaging are performed. The HST images are taken with the F555W (roughly ground-based V) and F814W (roughly I) filters on the Wide Field/Planetary Camera 2 (WFPC2) and the F160W (roughly H) on the Near Infrared Camera and Multi-object Spectrograph (NICMOS). The images often show both the optical counterparts of the radio emission and the lensing galaxy, both of which strengthen the arguments in favor of the gravitational lens interpretation of the system. As discussed in Chapter 2, it is possible to construct a model of the gravitational potential of the lens using the constraints provided by the locations and flux density ratios of the lensed images of the background source. For the CLASS lenses a preliminary model has always been constructed before any optical imaging occurs. The detection of a lensing galaxy in the location predicted by the models is a strong confirmation of the lensed nature of the system. In addition, the achromatic nature of gravitational lensing implies that the optical and radio morphology of the lensed images should be the same, as long as the emission is produced by the same region of the background source. Thus, if the radio components have the same relative positions as their presumed optical

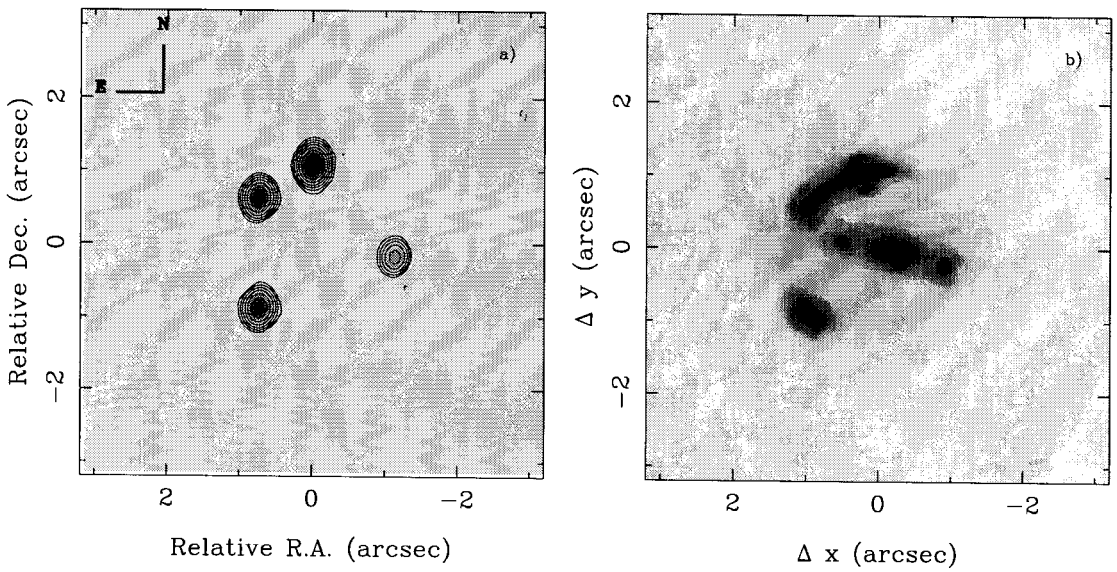

Figure 2.4 Radio (left) and infrared (right) images of the 1608+656 lens system. The radio map is from a 8.4 GHz follow-up investigation, the infrared image is a F160W image taken with NICMOS (Fassnacht et al. 1998b). The NICMOS image shows the optical counterparts of the radio components, with an arc connecting the two brightest components. Emission from the lensing galaxy is seen inside the ring formed by the four images of the background source.

counterparts, the lensing hypothesis is further strengthened, especially if the system geometry is complex (e.g., more than two images). Figure 2.4 shows an example of a system in which a complex radio morphology is reproduced at infrared wavelengths.

The optical and infrared images are used to get the magnitudes, colors, and rough morphologies of the lens galaxies. The separation between the lensed images is a direct indication of the mass of the lensing galaxy. Thus, mass-to-light ratios of the lensing galaxies can be computed and examined for evidence of evolution with redshift (e.g., Keeton, Kochanek, & Falco 1998). The HST images, with their high angular resolution, provide not only the most accurate means of determining the lens galaxy

morphology, but also give high-precision relative positions between the lensing galaxy and lensed images. These relative positions provide strong constraints on models of the gravitational potential of the lens.

Spectroscopic observations of the lens systems are performed to measure the redshifts of the lens and background source. The system redshifts are crucial to using the systems to determine H_0, as discussed in the previous chapter. The Hale 5-m and Keck 10-m telescopes are invaluable instruments in the quest for the system redshifts because they provide the sensitivity needed to measure redshifts of these often faint objects. The spectroscopy of the lens systems can also be used to determine the velocity dispersions of the lensing galaxies. These data can be used to place constraints on models of the gravitational potential of the lens (e.g., Romanowsky & Kochanek 1998; Falco et al. 1997).

2.8 New Lenses and Survey Status

At this time, the survey observations have been completed for the first three phases of CLASS. Over 12,000 sources have been observed. A planned fourth phase of CLASS will contain an estimated 700 sources. The candidate selection has been performed for the first three phases. All candidates from CLASS1 and CLASS2 have been observed with MERLIN, and a proposal to observe the CLASS3 candidates has been submitted. All of the CLASS1 and CLASS2 candidates surviving the MERLIN filter now have

Table 2.4 SUMMARY OF FILTERING PROCESS FOR CLASS1 AND CLASS2

Instrument	Sources Observed	Candidates Selected
VLA	7741	140
MERLIN	140	25
VLBA	25	12

Table 2.5 GRAVITATIONAL LENSES DISCOVERED IN CLASS

Lens System	Phase	N_{im}	z_l	z_s	Reference(s)[a]
0712+472	1	4	0.4060	1.339	J98, FC98
0742+366	2	2			
0827+525	2	2			
1127+385	2	2			K98
1152+199	3	2	0.4386	1.019	My98
1359+154	3	4		3.235	My98
1555+375	2	4			Ma98
1600+434	1	2	0.4144	1.589	J95, FC98
1608+656	1	4	0.630	1.394	M95, F96
1933+503	1	10	0.755		S98
2045+265	2	4	0.8674	1.28	F98
2319+051	2	2			Ma98

[a]References are Jackson et al. 1998b (J98), Fassnacht & Cohen 1998 (FC98), Koopmans et al. 1998 (K98), Myers et al. 1998 (My98), Marlow et al. 1998 (Ma98), Jackson et al. 1995 (J95), Myers et al. 1995 (M95), Fassnacht et al. 1996 (F96), Sykes et al. 1998 (S98), Fassnacht et al. 1998a (F98).

been observed with the VLBA. Table 2.4 summarizes the observations and candidate selection for CLASS1 and CLASS2. Table 2.5 lists the 12 new gravitational lenses found by CLASS so far. Approximately 25 candidates, most from CLASS3, are still being investigated. *Hubble Space Telescope* images of all of the CLASS1 and CLASS2 lenses will have been obtained by the end of Cycle 7. Spectroscopic observations have been obtained for most of the new lenses, and many of the system redshifts are known (Table 2.5).

The discovery of at least 12 new gravitational lenses in the four and a half years since the beginning of CLASS allows us to pursue actively the goals of the survey.

- *Quest for H_0:* Three of the new lens systems are being monitored to search for time delays. One of these, the 1608+656 system, has produced the first determination of H_0 from a CLASS lens (Chapter 5 of this thesis). The other lenses being monitored are 1600+434 (L. Koopmans) and 1933+503 (E. Xanthopoulos).

- *Constraints on Λ:* With a nearly completed, homogeneously selected survey of 13,000 sources, CLASS provides an excellent sample with which to use lensing rates to constrain Λ. The JVAS source selection is nearly the same as that made in CLASS, but for brighter sources. Therefore, the two surveys can be combined to yield a sample of over 16,000 sources. For lens surveys conducted at radio wavelengths, the difficulties in determining the lensing rate as a function of source redshift arise not from losing lenses due to extinction or atmospheric blurring, but rather from the fact that the redshift distribution of radio sources is not well determined (e.g., Kochanek 1996b; Falco, Kochanek, & Munoz 1998). Spectroscopic observations of faint flat-spectrum radio sources are being made to determine the redshift distribution of the population from which the lenses are drawn.

- *Investigations of galaxies at intermediate redshifts:* The HST images have provided lens galaxy magnitudes, colors, and morphologies for many of the CLASS

systems. In several systems, the flux ratios of the lensed images of the background source change with wavelength. This may indicate that one or more of the images is reddened (Jackson et al. 1997). In addition, the lens in 1600+434 shows a distinct dust lane and has been identified as an edge-on spiral galaxy (Jackson et al. 1997; Jaunsen & Hjorth 1997). In fact, the morphologies of the lensing galaxies in four out of five systems observed by Jackson et al. (1997) may indicate that they are disk systems; they appear to be highly elongated in the HST images, and the major axis position angle of the luminous material generally matches that of mass (from models of the lensing potential). The possibility of a relatively high incidence of disk galaxy lenses is surprising since 80 – 90% of lenses are expected to be massive E/S0 galaxies (e.g., Fukugita & Turner 1991; Kochanek 1996a). The magnitudes of the lenses are combined with the masses implied by the separation of the images of the background sources to calculate mass-to-light ratios (Jackson et al. 1998a). Some of the resulting values are quite high, especially in the case of 1600+434 (Jaunsen & Hjorth 1997; Fassnacht & Cohen 1998; Keeton, Kochanek, & Falco 1998). However, in all of the CLASS systems which have been imaged by HST, the lensing galaxy has been detected. Thus, there have been no "dark lenses" found in CLASS so far (Jackson et al. 1998a).

- *Addition to phase calibrator lists:*

The CLASS1 and CLASS2 source lists are now publicly available on the web at `http://www.jb.man.ac.uk/~njj/glens/class.html`. Active followup studies of the CLASS and JVAS samples are being conducted by members of the CLASS collaboration and of the Consortium for European Research on Extragalactic Surveys (CERES; `http://www.jb.man.ac.uk/~ceres1/`)

The remainder of this thesis presents observations of two of the new CLASS lenses, 1608+656 and 2045+265, and the interpretation of those observations.

REFERENCES

Barkana, R., Lehár, J., Falco, E. E., Grogin, N. A., Keeton, C. R., & Shapiro, I. I. 1998 ApJ, submitted (astro-ph/9808096)

Bennett, C. L., Lawrence, C. R., Burke, B. F., Hewitt, J. N., & Mahoney, J. 1986, ApJS, 61, 1

Browne, I. W. A., Patnaik, A. R., Wilkinson, P. N. & Wrobel, J. M. 1998, MNRAS, 293, 257

Condon, J. J., Cotton, W. D., Greisen, E. W., Yin, Q. F., Perley, R. A., Taylor, G. B., & Broderick, J. J. 1998, AJ, 115, 1693

Douglas, J. N., Bash, F. N., Bozyan, F. A., Torrence, G. W., & Wolfe, C. 1996, AJ, 111, 1945

Falco, E. E., Kochanek, C. S., & Munoz, J. A. 1998, ApJ, 494, 47

Falco, E. E., Shapiro, I. I., Moustakas, L. A., & Davis, M. 1997, ApJ, 484, 70

Fassnacht, C. D. & Cohen, J. G. 1998, AJ, 115, 377

Fassnacht, C. D., et al. 1998a, AJ, submitted (also this thesis, Chapter 4)

Fassnacht, C. D., Pahre, M. A., & Readhead, A. C. S. 1998b, in preparation

Fassnacht, C. D., Womble D. S., Neugebauer, G., Browne, I. W. A., Readhead, A. C. S., Matthews, K., & Pearson, T. J. 1996, ApJ, 460, L103 (also this thesis, §3.2)

Fukugita, M. & Turner, E. L. 1991, MNRAS, 253, 99

Gregory, P. C. & Condon, J. J. 1991, ApJS, 75, 1011

Gregory, P. C., Scott, W. K., Douglas, K., & Condon, J. J. 1996, ApJS, 103, 427

Griffith, M., Heflin, M., Conner, S., Burke, B., & Langston, G. 1991, ApJS, 75, 801

Griffith, M., Langston, G., Heflin, M., Conner, S., Lehár, J., & Burke, B. 1990, ApJS, 74, 129

Haarsma, D. B., Hewitt, J. N., Lehár, J., & Burke, B. F. 1997, ApJ, 479, 102

Hawkins, M. R. S., Clements, D., Fried, J. W., Heavens, A. F., Veron, P., Minty, E. M., & Van Der Werf, P. 1997, MNRAS, 291, 811

Hewitt, J. N., Burke, B. F., Turner, E. L., Schneider, D. P., Lawrence, C. R., Langston, G. I., & Brody, J. P. 1988, in *Gravitational Lenses*, eds., J. M. Moran, J. N. Hewitt & K. Y. Lo, (Berlin: Springer-Verlag), 147

Högbom, J. 1974, ApJS, 15, 417

Jackson, N., et al. 1995 MNRAS, 274, L25

Jackson, N. J., Nair, S., & Browne, I. W. A. 1997, in *Observational Cosmology with the New Radio Survey*, eds., M. Bremer, N. Jackson & I. Perez-Fournon (Dordrecht: Kluwer) 315

Jackson, N., Helbig, P., Browne, I., Fassnacht, C. D., Koopmans, L., Marlow, D., & Wilkinson, P. N. 1998a, A&A, 334, L33

Jackson, N. J. et al. 1998b MNRAS, 296, 483

Jaunsen, A. O. & Hjorth, J. 1997, A&A, 317, L39

Keeton, C. R., Kochanek, C. S., & Falco, E. E. 1998, ApJ, submitted (astro-ph/9708161)

Kellerman, K. I. & Pauliny-Toth, I. I. K. 1981, ARA&A, 19, 373

King, L. J., Browne, I. W. A., Muxlow, T. W. B., Narashima, D., Patnaik, A. R., Porcas, R. W., & Wilkinson, P. N. 1997, MNRAS, 289, 450

Kochanek, C. S. & Lawrence, C. R. 1990, AJ, 99, 1700

Kochanek, C. S., Falco, E. E., & Schild, R. 1995, ApJ, 452, 109

Kochanek, C. S. 1996a, ApJ, 466, 638

Kochanek, C. S. 1996b, ApJ, 473, 595

Kochanek, C. S., Falco, E. E., Impey, C., Lehár, J., McLeod, B., & Rix, H.-W. `http://cfa-www.harvard.edu/glensdata/`

Koopmans, L. V. E., et al. 1998, MNRAS, submitted

Kundić, T. et al. 1995, ApJ, 455, L5

Kundić, T. et al. 1997a, ApJ, 482, 75

Langston, G. I., Heflin, M. B., Conner, S. R., Lehár, J., Carrilli, C. L., & Burke, B. F. 1990, ApJS, 72, 621

Larkin, J. E., et al. 1994, ApJ, 420, L9

Lawrence, C. R., Elston, R., Januzzi, B. T., & Turner, E. L. 1995, AJ, 110, 2570

Malhotra, S., Rhoads, J. E., & Turner, E. L. 1997, MNRAS, 228, 138

Marlow, D. R., et al. 1998, in preparation.

McLeod, B. A., Bernstein, G. M., Rieke, M. J., & Weedman, D. W. 1998, AJ, 115, 1377

Myers, S. T., et al. 1995, ApJ, 447, L5 (also this thesis, §3.1)

Myers, S. T., et al. 1998, in preparation

Oscoz, A., Mediavilla, E., Goicoechea, L. J., Serra-Ricart, M., & Buitrago, J. 1997, ApJ, 479, L89

Patnaik, A. R., Browne, I. W. A., Wilkinson, P. N., & Wrobel, J. M. 1992, MNRAS, 254, 655

Rengelink, R. B., Tang, Y., de Bruyn, A. G., Miley, G. K., Bremer, M. N., Röttgering, H. J. A., & Bremer, M. A. R. 1997, A&AS, 124, 259

Romanowsky, A. J. & Kochanek, C. S. 1998, ApJ, submitted (astro-ph/9805080)

Shepherd, M. C. 1997, in *Astronomical Data Analysis Software and Systems VI*, eds. G. Hunt & H. E. Payne, (ASP Conference Series, v125) 77

Sykes, C. M., et al. 1998, MNRAS, in press

Turner, E. L. 1990, ApJ, 242, L135

Walsh, D., Carswell, R. F., & Weymann, R. J. 1979, Nature, 279, 381

Wilkinson, P. N., Browne, I. W. A., Patnaik, A. R., Wrobel, J. M., & Soratia, B. 1998, MNRAS, in press

Chapter 3

1608+656

3.1 1608+656: A Quadruple Lens System Found in the CLASS Gravitational Lens Survey†

S.T. Myers, C.D. Fassnacht, S.G. Djorgovski, R.D. Blandford, K. Matthews, G. Neugebauer, T.J. Pearson, A.C.S. Readhead, J.D. Smith, D.J. Thompson, D.S. Womble

Palomar Observatory, California Institute of Technology, 105-24, Pasadena, CA 91125

I.W.A. Browne, P.N. Wilkinson, S. Nair

University of Manchester, NRAL, Jodrell Bank, Macclesfield, Cheshire SK11 9DL, UK

N. Jackson[1], I.A.G. Snellen, G.K. Miley

†Previously published as Myers et al. 1995, in *The Astrophysical Journal (Letters)*, 447, L5. In this version the reference list has been updated to cite the published versions of papers, and lines in some figures have been darkened for clarity.

[1]Current address University of Manchester, NRAL, Jodrell Bank, Macclesfield, Cheshire SK11 9DL, UK

Leiden Observatory, Postbus 9513, 2300 RA Leiden, The Netherlands

A.G. de Bruyn[2], R.T. Schilizzi[3]

NFRA, Postbus 2, 7990 AA Dwingeloo, The Netherlands

Abstract

The first phase of a large gravitational lens survey using the Very Large Array at a wavelength of 3.6 cm has been completed, yielding images for 3258 radio sources. The Cosmic Lens All-Sky Survey, or CLASS, is designed to locate gravitational lens systems consisting of multiply-imaged compact components with separations $> 0\farcs2$. We report here the first discovery of a gravitational lens from the survey: 1608+656, a quadruply-imaged object with maximum separation of $2\farcs1$. Images from the Palomar 5-m and Keck 10-m telescopes show the lensed images and the lensing galaxy. An optical spectrum obtained with the Palomar 5-m Telescope indicates a redshift of $z = 0.6304$ for the lensing galaxy. No conclusive redshift for the lensed object has been determined, although a single strong emission line is found at 9240Å in the Keck LRIS spectrum. The two most likely identifications for this line are either Hβ ($z = 0.90$) or Mg II ($z = 2.30$)[4]. The preliminary lens model derived from the radio image

[2]and Kapteyn Laboratory, Postbus 800, 9700 AA Groningen, The Netherlands
[3]and Leiden Observatory
[4]The source redshift has now been measured to be $z = 1.394$ (see §3.2 or Fassnacht et al. 1996, ApJ, 460, L103).

reproduces the observed configuration and relative fluxes of the images, as well as the position, shape, and orientation of the lensing galaxy. Because a simple mass model is able to fit the observations, we argue that this lens system is promising for determining H_0.

3.1.1 Introduction

Gravitational lenses provide a unique way of probing the distribution of clumpy matter in the Universe and have the potential to give values for the Hubble constant and other cosmological parameters. With this in mind, and building upon the success of JVAS, the Jodrell-Bank/VLA astrometric survey (Patnaik et al. 1992; Browne et al. 1998), we have embarked on a new much larger VLA survey: CLASS, the Cosmic Lens All Sky Survey. The ultimate aim of CLASS is to survey $\sim 10^4$ flat spectrum radio sources with the prime motivation of identifying systems suitable for Hubble constant determination based on measurements of time delays. Restricting the sample to flat spectrum sources preferentially selects objects with compact and variable components well suited to time delay measurements. A total of 3258 targets have been observed in the first phase of the CLASS survey. Based on previous surveys with similar selection criteria (e.g., Patnaik et al. 1992), we expect to find about one lens per 500 sources observed, i.e., about 6 new lenses should emerge from the first phase of the survey and, ultimately, about 20 lenses from the survey of the northern

hemisphere. CLASS has already yielded two new lens systems: 1600+434, a double image system (Jackson et al. 1995) and 1608+656, reported here.

3.1.2 CLASS VLA Observations

The CLASS observations took place in several sessions during February, March and April 1994 in the A-configuration of the VLA[5] at a frequency of 8.4 GHz. The 3258 sources were selected from the 4.85 GHz Green Bank Survey (87GB: Gregory & Condon 1991) to have flux densities ≥ 50 mJy and $|b| > 10°$. At the time of the CLASS VLA observations, we were able to select 683 sources with two-point spectral indices of $\alpha \geq -0.5$ between 4.85 GHz and the 325 MHz Westerbork Northern Sky Survey (WENSS: Rengelink et al. 1997). The remaining 2575 sources were selected with $\alpha \geq -0.6$ between 4.85 GHz and the 365 MHz Texas Survey. The lens 1608+656 was found in the 87GB/Texas portion of the survey.

Two independent IFs of 25 MHz bandwidth were centered at 8.415 GHz and 8.465 GHz. An on-source dwell time of 30 seconds was used. A source from the JVAS (Patnaik et al. 1992) was observed after every 14th target source for phase calibration. The average target source observation rate was one per minute, including the overhead from calibration and slewing.

The initial calibration of the data was done using AIPS following the standard

[5]The National Radio Astronomy Observatory is operated by Associated Universities, Inc., under cooperative agreement with the National Science Foundation.

procedure. Automatic mapping of the 2575 87GB sources was performed using the DIFMAP package (Shepherd, Pearson & Taylor, 1994). From the resulting maps $\sim$ 100 objects which show multiple components have been selected for further investigation as potential gravitational lens candidates. Only a few of these are expected to be real lensed systems.

The source 1608+656 (target source 87GB 16087+6540) was observed on 1994 March 1. The VLA image is shown in Figure 3.1a. The source consists of four well-separated unresolved components and has a slightly inverted radio spectrum between 325 MHz and 4.85 GHz, a property that led to it being followed-up with the VLA independently by Snellen et al. amongst a sample of other inverted spectrum objects. The results of these and other auxiliary radio observations are described in a companion paper (Snellen et al. 1995).

Several cycles of model-fitting and phase-only self-calibration were performed in DIFMAP on the VLA data using four point sources. The residual image showed no missing extended flux. The rms noise level in the final image was 0.44 mJy. A total flux density of 73.2 ± 0.9 mJy was measured. The individual flux densities for components A, B, C and D were 35.6, 17.8, 15.2, and 4.6 mJy respectively. The brightest component (A) is located at $16^{\rm h}\,09^{\rm m}\,13\overset{\rm s}{.}956$ $+65^\circ\,32'\,28\overset{''}{.}97$ (J2000). This was $26\overset{''}{.}4$ from the 87GB position.

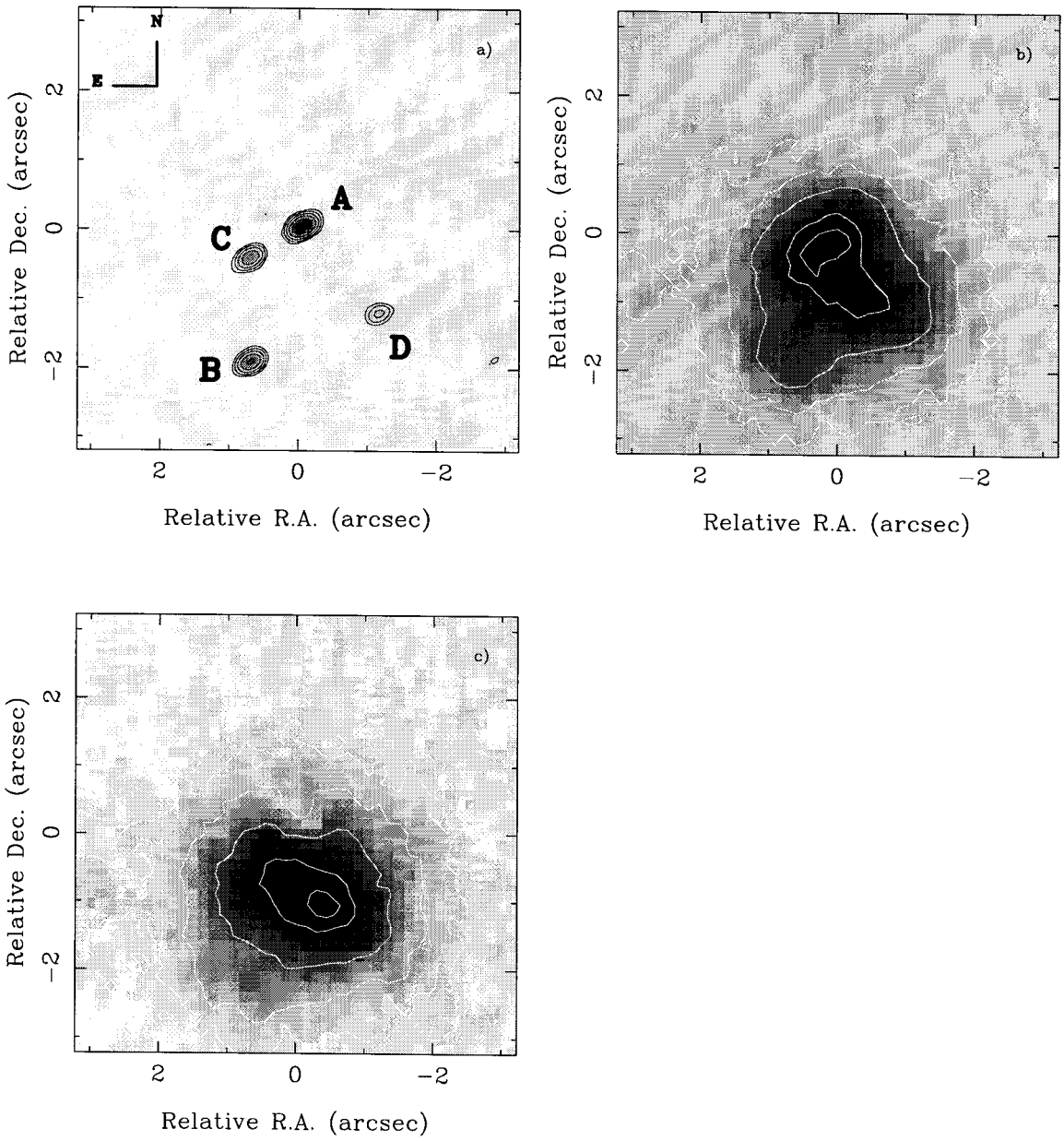

Figure 3.1 The CLASS gravitational lens 1608+656. (a) 8.4 GHz VLA radio image. The peak in the image is 34 mJy/beam. Contours begin at 1.1 mJy/beam (2.5σ), spaced by factors of 2. (b) Keck NIRC image. Seeing is 1″. (c) Keck NIRC image with scaled VLA model subtracted. Residual should reflect lensing galaxy emission. Note position, ellipticity and position angle of galaxy for comparison with the lens model (Fig. 3.4).

3.1.3 Follow-up optical and infrared observations

On 1994 August 9, an optical image and spectrum of 1608+656 were obtained with the Palomar Observatory 5-m Telescope. The optical image (see Figure 3.2), taken with the COSMIC camera in 1.″5 seeing, is consistent with blended emission from the components in the same configuration as in the radio image as well as extra emission from the presence of a lensing galaxy. Preliminary photometry gives the magnitudes in the Gunn system for the entire image (including the lensing galaxy) of $r = 19.4^m$ and $i = 19.2^m$. Since the weather was non-photometric, these may be uncertain by a few tenths of a magnitude.

The spectrum, taken on the same night using the Double Spectrograph with a 2″ slit accepting most of the light from the aggregate system, is shown in Figure 3.3a. The total exposure was 3000 seconds. The absorption lines of Mg II $\lambda\lambda 2796, 2803$, H$\epsilon$, H$\delta$, and the [O II] $\lambda 3727$ emission line are indicated. These yield a redshift of $z = 0.6304$ for the lensing galaxy. The Balmer absorption lines are strong, indicating that there are A stars present, and that the lens might possibly be a post-starburst galaxy. The 4000Å break is weak, which is what would be expected in the combined light of a young stellar population and a background quasar.

On 1994 August 22, a 2.2μm (K band) infrared image of 1608+656 (Figure 3.1b) was obtained on the W.M. Keck[6] 10-m Telescope using the near infrared camera

[6]The W.M. Keck Observatory is operated as a partnership between the California Institute of Technology and the University of California, and was made possible by the generous gift of the W.M.

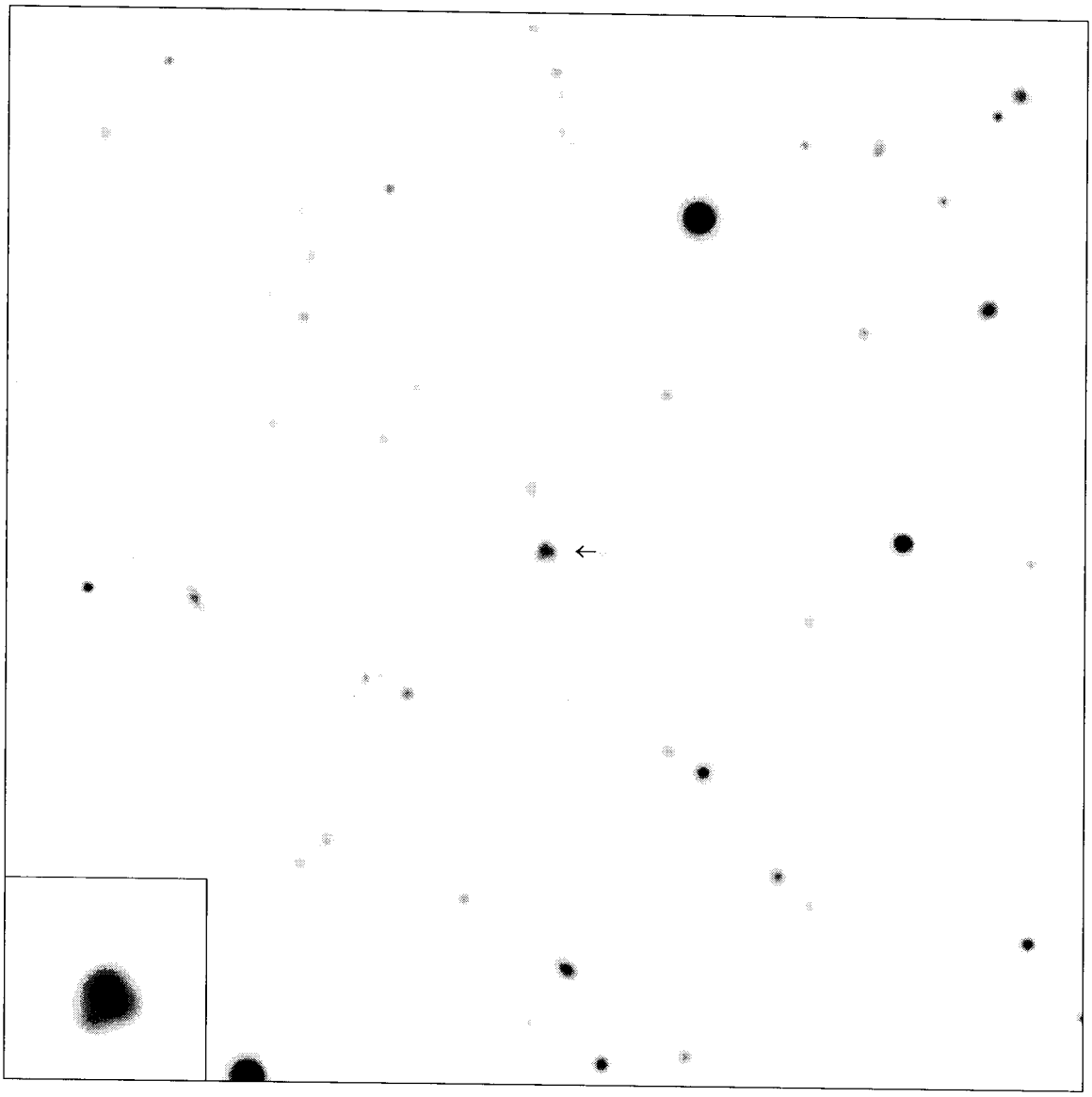

Figure 3.2 An i-band image of the field of 1608+656 obtained at Palomar using COSMIC. The field shown is 200″square, with N at the top and E to the left. The inset image is in the r band, and is 10″square.

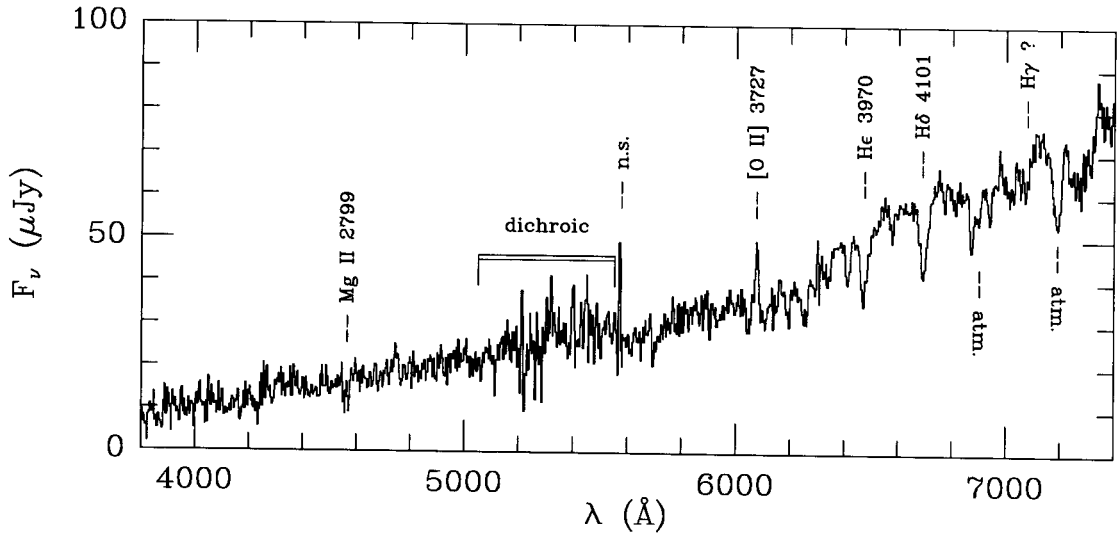

Fig. 3a

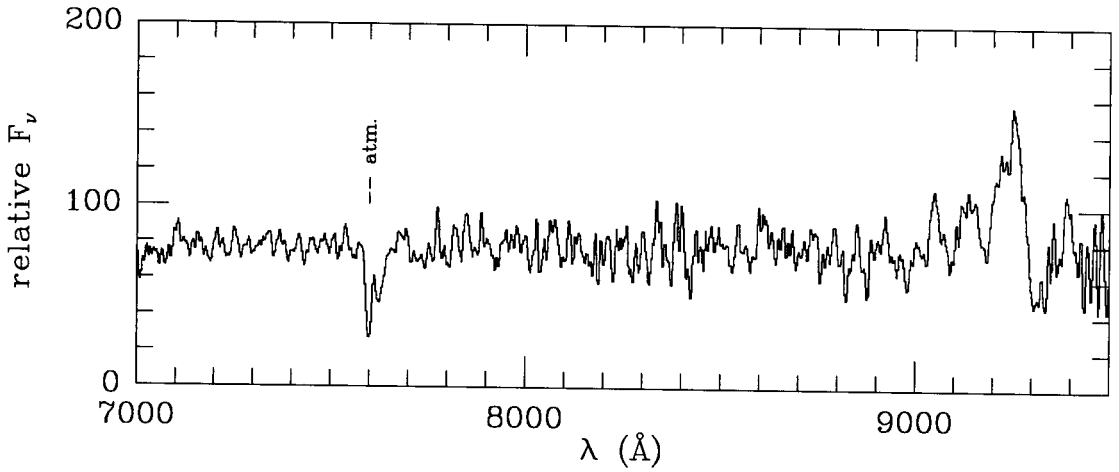

Fig. 3b

Figure 3.3 (a) spectrum of 1608+656 using the Double Spectrograph at the Palomar 5-m Telescope versus observed wavelength. The detected emission and absorption features attributed to the lensing galaxy ($z_l = 0.6304$) are indicated. (b) Keck LRIS spectrum, self-normalized to a flat shape, since a proper flux calibration is not available. The only convincing feature detected is centered at 9240Å. In both spectra, strong atmospheric absorption (atm) and night-sky emission (ns) features are indicated.

(NIRC: Matthews & Soifer 1994). The total exposure time was 450 seconds, and the seeing was 1″. The three brightest lens images and the lensing galaxy are seen in this image. A model with four point components was constructed with relative intensities and positions determined from the VLA radio images, convolved with the K-band point spread function, and then subtracted from the NIRC image. The overall scaling factor for the VLA model was adjusted to minimize the residual at the image positions. The results of this are shown in Figure 3.1c. There is clearly extended emission from the lensing galaxy remaining in the subtracted image. The lensing galaxy has a K-band flux roughly four times greater than that of the total emission from the four lens components. The galaxy image has an axial ratio of $b/a = 0.56 \pm 0.10$ with its major axis in position angle 60°. The true galaxy shape is likely to be more elliptical than this axial ratio would indicate, as the image is substantially circularized by the seeing.

Photometry on the K band residual image yields a mean surface brightness of $60\,\mu\mathrm{Jy\,arcsec^{-2}}$ within a circle of radius 1.″1. This gives a distance-independent mean K surface luminosity, L_E, of $7.7 \times 10^8\,\mathrm{L_\odot\,kpc^{-2}}$ for the lensing galaxy. The observed 2.2μm emission was emitted at 1.3μm. The ratio of 1.3μm to V fluxes for nearby galaxies is near unity, so the K band luminosity should be roughly equivalent to a V luminosity.

An additional spectrum of the object was obtained using the Low Resolution

Keck Foundation.

Imaging Spectrograph[7] on the W.M. Keck 10-m Telescope, on the night of UT 1994 September 4, in non-photometric conditions. The spectrum covers the range 7000Å – 9600Å, with a resolution of around 7Å FWHM. Unfortunately, no standard star exposure was obtained with the same setup, due to instrumental problems. The spectrum is shown in Figure 3.3b, with the baseline artificially flattened. The only non-telluric feature detected is a single strong emission line at 9240Å (±50Å). This line is broader than the instrumental resolution. This does not correspond to any feature expected at the redshift of the lensing galaxy, and is assumed to belong to the lensed object.

The plausible identifications for this line are either Mg II at $z = 2.30$ or Hβ at $z = 0.90$[8]. If the Mg II identification is correct, then Lyα λ1216 at 4014Å and C III] λ1909 at 6302Å would be expected, neither of which is seen in the Palomar spectrum; C IV λ1549 at 5113Å would fall in the dichroic fold of the Palomar data, where the noise is high. The Hβ interpretation, on the other hand, is supported by the presence of a weak broad feature at 5320Å which is where Mg II should be found. Unfortunately, this is close to the dichroic fold and we are not confident of its reality. The $z = 0.90$ Hγ line at 8250Å is not seen in the LRIS spectrum.

[7]LRIS; Oke, J. B. et al. 1995, PASP, 107, 375.
[8]Now known to be $z = 1.394$ (see §3.2).

3.1.4 A possible lens model

A lens model for 1608+656 has been constructed based on the information contained in the VLA 8.4 GHz radio map. An oblate spheroidal mass model has been used for the lens, with mass density $\rho(r)$ following the modified Hubble profile:

$$\rho(r) = \rho_0 \left[1 + (r/r_c)^2\right]^{-3/2} \qquad r^2 = x^2 + y^2/(1-e^2) + z^2. \tag{3.1}$$

The spheroid is assumed to be viewed edge on in order to simplify the model, with x, y in the plane of the sky and z along the line of sight (e is the eccentricity, and r_c is the scale length of the mass distribution). Note that the r^{-3} profile assumes that the mass traces the light distribution. The lensing code used was described in Narasimha, Subramanian & Chitre (1982, 1984). The constraints are the relative image positions and the relative fluxes, making a total of 9 constraints. The model positions were registered on the position of observed component B, which is not so close to the critical surface as A. Fitting of the lens model to the VLA image yields values for the 6 variable parameters: r_c, e, a mass parameter σ^* in units of velocity, the two coordinates of the lens center, and the position angle θ of the major axis of the spheroid in the plane of the sky.

The set of parameters listed in Table 3.1 yields a good match to the observations. The position and orientation of the galaxy which is visible in the Keck infrared image agree to within the measurement uncertainties with those predicted by the model. The high eccentricity called for in the mass model for the lens galaxy corresponds

Table 3.1 PARAMETERS FOR A GRAVITATIONAL LENS MODEL FOR 1608+656

Scale Length r_c	Mass Parameter σ^* (km/s)	Eccentricity e	P.A. θ (°)	Cutoff[a] n	Lens Center[b]
0.″48	311.7	0.96	+67.0	20	(−0.″33, −1.″00)

[a] The mass model was cutoff at n scale-lengths to ensure finite total mass.
[b] This value is with respect to Image A (see Table 3.2).

Table 3.2 IMAGE PROPERTIES FOR THE LENS MODEL

Image	Observed		Model			
	Position[a] (arcsec)	Flux ratio (vs. B)[b]	Position (arcsec)[c]	Magnification	Flux ratio (vs. B)	Delay ($h^{-1}\,T_0$ days)
A	(+0.00, +0.00)	2.06 ± 0.06	(+0.15, +0.19)	+2.58	1.68	11.9
B	(+0.74, −1.96)	1.00	(+0.74, −1.96)	+1.54	1.00	0.0
C	(+0.75, −0.46)	0.85 ± 0.03	(+0.76, −0.45)	−1.36	0.88	13.1
D	(−1.13, −1.24)	0.26 ± 0.03	(−1.27, −1.24)	−0.35	0.23	34.2
E	...	...	(−0.52, −1.05)	+0.04	0.03	...

[a] Position offsets with respect to component A at $16^h\,09^m\,13.^s956$ +65° 32′ 28.″97 (J2000).
[b] Measured 8.4 GHz flux density for component B was 17.80 ± 0.44 mJy.
[c] Position of model component B fixed to radio position of image B.

to an axial ratio (minor axis to major axis) of $\sqrt{1-e^2} = 0.28$. The image positions and flux density ratios observed in the VLA image and the predicted model values are listed in Table 3.2. The predicted position and magnification for the brightest image A are the most uncertain; therefore, the flux ratios are taken relative to image B; the positions and ratios for C and D relative to B agree within the measurement uncertainties. The demagnified fifth image E is predicted to be below the detection threshold in the radio map. Even with this preliminary model, the pattern of image positions and flux density ratios is reproduced, strongly suggesting that the basic properties of the lensing potential are well determined.

The lens parameters are cast in a redshift-independent form as in Nair, Narasimha, & Rao (1993). The expression for the central density in the lens mass distribution is

Table 3.3 MASSES AND DELAYS FOR POSSIBLE SOURCE REDSHIFTS

z_s	d_{ls}	M_E ($h^{-1}\,M_\odot$)	$(M/L)_E^a$ ($h\,M_\odot/L_\odot$)	T_0	C-B delay (h^{-1} days)	C-A delay (h^{-1} days)
0.9	4.77	5.6×10^{11}	13.2	6.19	81.1	7.67
2.3	1.93	2.3×10^{11}	5.3	2.51	32.9	3.11

[a] Using $L_E = 7.7 \times 10^8$ $L_\odot$ kpc^{-2} from NIRC K band image.

given by:

$$\rho_0 = \frac{9\sigma^{*2}}{4\pi G r_c^2}\, d_{ls} \qquad\qquad d_{ls} = \frac{D_s}{D_{ls}}. \tag{3.2}$$

D_l, D_s and D_{ls} are the observer–lens, observer–source and lens–source angular diameter distances (e.g., Weinberg, 1972). Note that the central velocity dispersion is given by $\sigma = \sigma^* \sqrt{d_{ls}}$. For $z_l = 0.6304$, then $D_l = 798\,h^{-1}$ Mpc ($q_0 = 0.5$). For the model in Table 1, we find a central density of $\rho_0 = 4.83 \times 10^9\, d_{ls}\, h^2\, M_\odot$ kpc^{-3}. The mass within the equivalent circular Einstein ring radius $\theta_E = 1\farcs1$ is $M_E = 1.18 \times 10^{11}\, d_{ls}\, h^{-1}\, M_\odot$. The inferred masses and mass-to-light (K band) ratio within θ_E for $z_s = 0.90$ and $z_s = 2.30$, the two most likely source redshifts, are listed in Table 3.3. The mass-to-light ratios are similar to those found for other lenses such as MG1654+1346 (Langston et al. 1990), while the masses are somewhat larger.

The image plane critical curves, along with the model image positions, and the corresponding source plane critical curves, with the source position marked, are shown in Figure 3.4. According to this model, image B should vary first. The predicted time delays are given in Table 3.2. Here we define $T_0 = (1 + z_l)\,(D_l\, d_{ls}/1\,\mathrm{Gpc})$. The shortest relative pairwise delay is $1.24\,T_0\,h^{-1}$ days between images A and C.

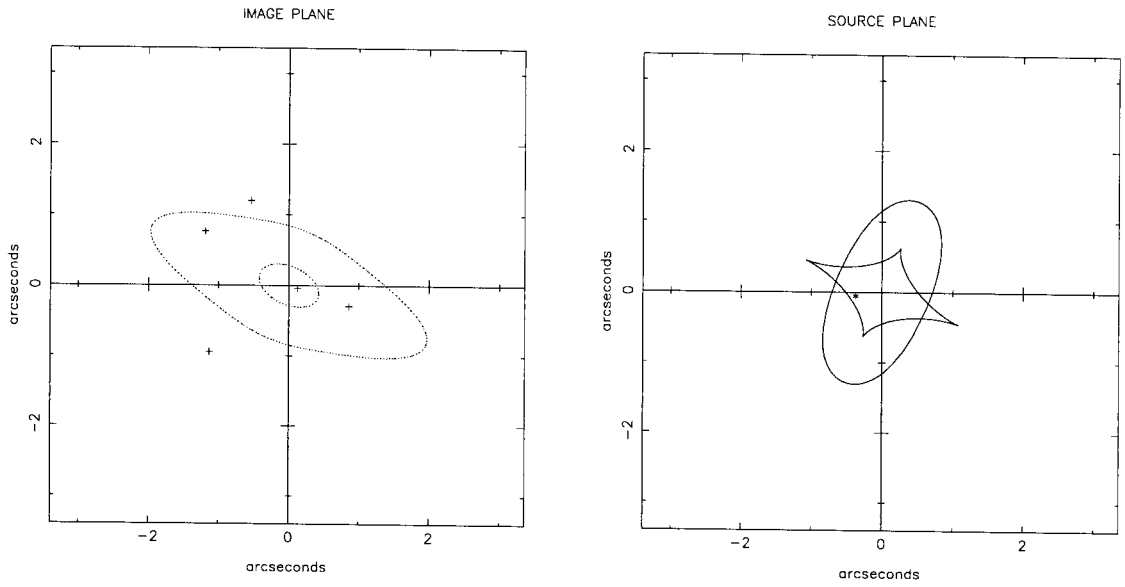

Figure 3.4 A preliminary lens model for the 1608+656 system. (*left*) Critical curves in image plane separating domains of 1,3,5 images. Positions of images are marked. (*right*) Lens mass model in source plane. The images of the inner and outer critical curves are shown. Correspondence of position, ellipticity, and orientation of lensing galaxy model with Keck NIRC residual is good.

A Friedmann-Robertson-Walker universe with a smoothed-out background matter distribution, $q_0 = 0.5$, and $h = H_0/100\,\mathrm{km\,s^{-1}\,Mpc^{-1}}$ is assumed. The predicted relative delays for the source redshifts are given in Table 3.3. The parameters in our simple lens model, given the missing source redshift, are well constrained by the current observations. VLBI measurements of milliarcsecond component separations in the four images, or the discovery of an Einstein ring from lensed jet emission, would help to constrain more complicated mass models.

3.1.5 Discussion and Conclusions

The necessary ingredients for using a gravitational lens to determine the distance scale are redshifts for lens and background object, variability in the lensed object with measured time delays between images, and an accurate model for the mass distribution in the lens and along the line-of-sight to the lens. We have determined the lens redshift and have a tentative redshift for the lensed object. The lensed source is the flat-spectrum core of a double radio source (Snellen et al. 1995), so it is likely that it will be variable at a measureable level. Source variations have allowed measurements of time delays in other systems (e.g., Lehár et al. 1992). The 1608+656 system appears to be simple compared to many other lens systems. The preliminary mass model consisting of a single galaxy with a specified orientation and ellipticity reproduces the observed image and lens configuration. If further observations support the simple lens model, and should the lens object prove to be variable, 1608+656 may prove to be an excellent system for determining the Hubble constant.

The lensing galaxy in the 1608+656 system presents an interesting puzzle. Whether the lens is a single highly elliptical spheroid, disk galaxy, or a pair of close galaxies has yet to be determined. The large implied mass within the image radius ($M_E \sim 5 \times 10^{11}\, h^{-1}\, \mathrm{M}_\odot$) and central velocity dispersion ($\sigma \sim 500\,\mathrm{km\,s^{-1}}$) are representative of first-ranked cluster ellipticals, yet the spectrum and high ellipticity is more suggestive of an early-type spiral galaxy. The Balmer absorption is indicative

of a post-starburst population of A-stars, with the emission line of [O II] caused by ongoing star formation. The large implied ellipticity of the mass distribution, plus the large implied mass, could also be due to a close pair of massive galaxies. The unexpectedly large number of quadruple lenses found in radio surveys, presumably due to highly elliptical potentials in many of the most massive lensing galaxies, may point toward a high merging rate. HST observations of this system have been allocated, and should provide a much more detailed view of the lensing galaxy.

STM is supported by an R.A. Millikan Fellowship at Caltech. The CLASS survey at Caltech is supported by NSF grant AST-9117100. SGD was supported by NSF PYI award AST-9157412. Infrared astrophysics at Caltech is supported by a grant from the NSF. DSW acknowledges support of a Hubble Fellowship provided by NASA through grant HF-1040.01-92A from the STScI, which is operated by the AURA. We thank the staff of the VLA, Palomar and Keck observatories for their assistance during our observing runs. STM also acknowledges the hospitality the ITP in Santa Barbara, which is supported by the NSF under grant PHY89-04035, during the completion of this manuscript.

REFERENCES

Browne, I. W. A., Patnaik, A. R., Wilkinson, P. N., & Wrobel, J. M. 1998, MNRAS, 293, 257

Gregory, P.C. & Condon, J.J. 1991, ApJS, 75, 1011

Jackson, N., et al. 1995 MNRAS, 274, L25

Langston, G. I., Conner, S. R., Lehár, J., Burke, B. F., & Weiler, K. W. 1990, Nature, 344, 43.

Lehár, J., Hewitt, J. N., Roberts, D. H., & Burke, B. F. 1992, ApJ, 384, 453

Matthews, K. & Soifer, T. 1994, in *Infrared Astronomy with Arrays: The Next Generation*, I. McLean, ed. (Dordrecht: Kluwer), p.239

Narasimha, D., Subramanian, K., & Chitre, S. M. 1982, MNRAS, 200, 941

Narasimha, D., Subramanian, K., & Chitre, S. M. 1984, MNRAS, 210, 79

Nair, S., Narasimha, D., & Rao, A.P. 1993, ApJ, 407, 46

Patnaik, A. R., Browne, I. W. A., Wilkinson, P. N., & Wrobel, J. M. 1992, MNRAS, 254, 655

Rengelink, R. B., Tang, Y., de Bruyn, A. G., Miley, G. K., Bremer, M. N., Röttgering, H. J. A., & Bremer, M. A. R. 1997, A&AS, 124, 259

Shepherd, M. C., Pearson,T. J., & Taylor,G. B. 1994, BAAS, 26, 987

Snellen, I. A. G., de Bruyn, A. G., Schilizzi, R. T., Miley, G. K., & Myers, S. T. 1995, ApJ, 447, L9

Weinberg, S., 1972, *Gravitation and Cosmology* (New York: Wiley)

3.2 1608+656: A Gravitationally Lensed Post-Starburst Radio Galaxy†

C.D. Fassnacht, D.S. Womble, G. Neugebauer

Palomar Observatory, California Institute of Technology, 105-24, Pasadena, CA 91125

I.W.A. Browne

NRAL Jodrell Bank, University of Manchester, Macclesfield, Cheshire SK11 9DL, UK

A.C.S. Readhead, K. Matthews and T.J. Pearson

Palomar Observatory, 105-24, California Institute of Technology, Pasadena, California 91125

Abstract

The gravitational lens system 1608+656 displays four flat spectrum, point-like components which are the images of the unresolved core of a double-lobed radio source. The lensing mass is a galaxy at $z = 0.630$. New spectra of this system enable us to determine a conclusive redshift of 1.394 for the lensed object. The spectra show prominent high order Balmer absorption lines and Mg II absorption. These lines, and the absence of [O II] emission, indicate that this is a post-starburst, or E+A galaxy. It is unique among lensed objects in not being a quasar, and among E+A galaxies in having the highest known redshift. Even allowing for lens

† Previously published as Fassnacht et al. 1996 in *The Astrophysical Journal (Letters)*, 460, L103.

magnification, the lensed object is a very luminous galaxy, with an absolute magnitude, $M(r) = -22.8^m$. The deconvolved infrared image indicates that the galaxy may be slightly resolved. The radio luminosity density of the lobes is $L_{1.4} = 5.78 \times 10^{25}$ W Hz^{-1}, which puts the source on the boundary between FR I and FR II radio galaxies. Together with the redshift for the lens and a satisfactory mass model, the determination of the lensed object redshift makes this system an excellent candidate for measuring H_0.

3.2.1 Introduction

The quadruply-imaged gravitational lens 1608+656 was discovered as part of the Cosmic Lens All Sky Survey (CLASS; Myers et al. 1996, in preparation), a large-scale search for gravitational lenses among flat-spectrum radio sources using the VLA[1]. CLASS was designed to find systems with the lensing potential dominated by a single galaxy. The expected yield from the survey is 10 to 15 new lenses. Because single-galaxy lensing potentials are fairly straightforward to model, CLASS provides a powerful method for determining galaxy masses and mass-to-light ratios. The 8.4 GHz radio map of 1608+656 shows four flat-spectrum, point-like components (Myers et al. 1995, hereafter Paper I[2]), while 1.4 GHz maps show that the source being lensed is the core of a classical double radio source (Snellen et al. 1995). Optical and infrared

[1]The VLA is a facility of the National Radio Astronomy Observatory, which is operated by Associated Universities, Inc., under contract with the National Science Foundation
[2]Also §3.1 of this thesis.

images (Paper I) show the same morphology as the 8.4 GHz radio map, and additionally show the lensing galaxy. Spectra of this object gave a redshift $z = 0.630$ for the lensing galaxy (Paper I), but did not yield a conclusive redshift for the background source. A simple mass model derived in Paper I reproduces the location of the images and the lensing galaxy. Thus, this is an excellent system for the determination of the Hubble constant H_0, provided that a redshift for the lensed object and a time delay can be measured. This paper reports on spectroscopic observations made with the Palomar 5 m Telescope which provide a redshift for the lensed object. Optical and infrared imaging are also reported. We have assumed $H_0 = 100h$ km s^{-1} Mpc^{-1} and $q_0 = 0.5$ throughout this paper.

3.2.2 Observations and Data Reduction

Spectroscopy

Optical spectra of 1608+656 were obtained on 1995 July 21 and 23 with the double spectrograph on the Palomar 5 m Telescope. A total of five 2000 second observations were made, covering the wavelength range 3400–9700Å. The observing conditions were excellent, with approximately 0.″8 FWHM seeing and no visible clouds. In order to minimize the contribution of light from the foreground lensing galaxy, the slit was aligned at a position angle of 160°, centered on lens components A and B (see Fig. 2a). A slit width of 1.″0 was used together with a 300 lines mm^{-1} grating in the blue and

a 158 lines mm^{-1} grating in the red to produce a spectral resolution of 5.4Å FWHM for $\lambda < 5100$Å and 15.2Å FWHM for $\lambda > 5100$Å.

The resulting data were reduced using the VISTA and IRAF software packages. Bias subtraction and flat-fielding were done using standard procedures. Because of the faintness of the object relative to the sky background, the spatial curvature of the spectrum was traced and removed using a standard star profile. The two-dimensional spectra were cleaned of cosmic rays and extracted to 1-D using an optimal weighting algorithm similar to that described by Horne (1986); spectra of the background sky and 1σ uncertainties based on Poisson statistics were also extracted by this routine. Flexure corrections to the wavelength scales were applied using prominent night-sky lines, and the data were flux calibrated using standard star exposures taken during the evening and morning twilights. Atmospheric absorption bands were removed from the individual exposures using template spectra which were produced by scaling the appropriate portions of standard star spectra to the effective object airmasses. All of the resulting spectra for 1608+656 were weighted according to their signal-to-noise ratios and added; a portion of the combined spectrum is shown in Fig. 3.5. No significant features are evident at wavelengths other than those shown in this figure.

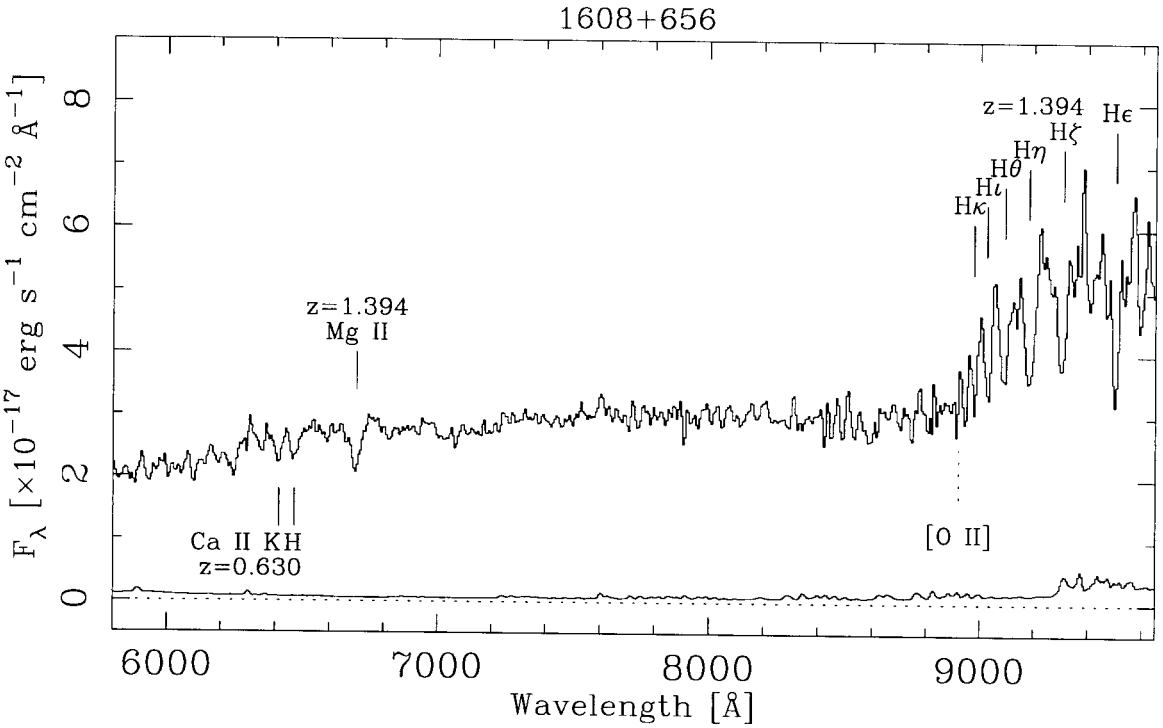

Figure 3.5 Optical spectrum of the gravitational lens 1608+656 with the slit positioned to maximize the background source light and minimize the lensing galaxy light. The wavelengths are as observed in air; features belonging to the background source, $z = 1.394$, and the lensing galaxy, $z = 0.630$, are labeled. The solid vertical lines mark the positions of detected absorption features at both redshifts whereas the dotted line marks the expected position of [O II] λ3726.6 emission at $z = 1.394$. The lower spectrum designates the 1σ uncertainties associated with the object spectrum.

Infrared Imaging

An image of 1608+656 was taken on the night of 1995 July 18 with the Cassegrain infrared camera at the f70 focus of the Palomar 5 m Telescope. The camera scale was 0.″125 per pixel and the median seeing was 0.″7 FWHM in the K-short (K_s) filter band which admits radiation between 2.00 and 2.30 μm. Twenty-five exposures, each of 40 seconds, were obtained using an offset guider which applied "tip-tilt" corrections based on the visual position of the guide star. Three similar exposures of a star 4′

from the object were interleaved with the 25 object observations to provide a point spread function (PSF); the guide star used for 1608+656 was also used for the PSF observations. The images were linearized, flat-fielded and sky-subtracted following standard procedures. The 25 images were sorted in order of sharpness and the eight sharpest images were combined in the mosaic image shown in Fig. 2a. Flux calibration was not done because the conditions were not photometric.

The PSF was normalized and convolved with a model containing the positions and intensities of the four unresolved radio components. The intensities were taken from a VLA image of 1608+656 which was observed on 1995 July 6. The resulting image was scaled to the level of the K-short image and subtracted from it, giving the residual image shown in Fig. 2b. A Lucy-Richardson deconvolution (Lucy 1974; Richardson 1972; Snyder, Hammond & White 1993) on the K-short image was also carried out using the normalized PSF. The result from 40 iterations is shown in Fig. 2c.

Optical Imaging

The 1608+656 field was observed with the imaging CCD camera on the Palomar 1.5 m Telescope on 1995 April 24-27, using Gunn r and i filters. Three 800 sec and two 600 sec exposures were taken of 1608+656. The limiting magnitudes for detecting unresolved objects were $m_r \sim 22.2$ and $m_i \sim 21.9$. A standard star was observed before and after the 1608+656 exposures. The camera scale was $0\farcs372$ per

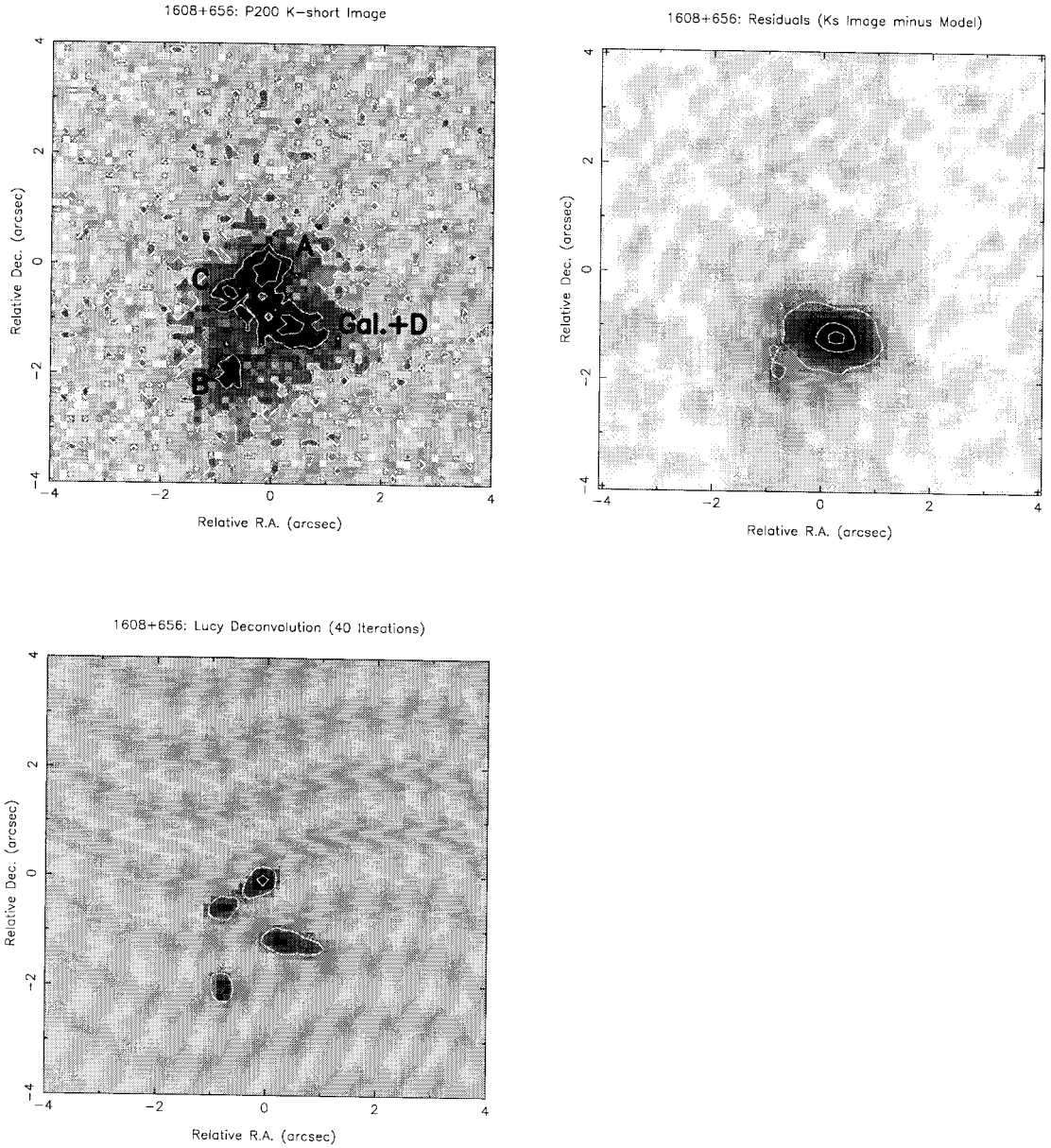

Figure 3.6 **(a)** Infrared K_s band image of the quadruple lens 1608+656. North is up and east is to the left. **(b)** Residual image of 1608+656 produced by the subtraction of a scaled radio model from the field. Resulting image is that of the lensing galaxy. **(c)** Lucy-Richardson deconvolution of K_s band image.

pixel, giving a field of view of $13' \times 13'$. The first three nights were photometric, with average seeing of $1\farcs4$ FWHM, which allowed a determination of colors for the object. The images were bias-subtracted and flat-fielded using IRAF. In a manner similar to that described above, residual images were created by subtracting a model of the four source components from the r and i images taken in the best seeing. The lens galaxy flux density was derived from the residual image and the source flux density from the model fit. Magnitudes were derived using the "apphot" package in IRAF and are given in the following section.

3.2.3 Results and Discussion

In the final spectrum, the blended Mg II doublet $\lambda\lambda$2795.5, 2802.7 is identified in absorption at 6696.0Å as are the Balmer absorption lines Hϵ λ3970.1, Hζ λ3889.1, Hη λ3835.4, Hθ λ3797.9, Hι λ3770.6 and Hκ λ3750.2 at λ= 9500.4, 9303.3, 9182.3, 9088.4, 9030.8, 8979.6Å. These lines yield an unambiguous redshift for the background source of $z = 1.394$. No [O II] λ3726.6 emission is detected at this redshift to a rest equivalent width limit of 1Å (3σ). For comparison, the Hζ line has a rest equivalent width of 3.9±0.5Å. A Ca II K & H $\lambda\lambda$3933.7, 3968.5 doublet is also clearly seen at $\lambda\lambda$=6411.8, 6469.4Å; this was seen in Paper I and is associated with the lensing galaxy at a redshift of $z = 0.630$. It should be noted that the $z = 1.394$ Mg II absorption occurs at the same wavelength as the Hδ absorption from the $z = 0.630$

lensing galaxy. This causes the spectrum of the lensing galaxy (see Paper I) to have deceptively strong Hδ absorption. However, the $z = 0.630$ [O II] emission and Mg II absorption seen in the lens spectrum (Paper I) are not associated with any lines from the background source.

The lensed object is not what one would expect for the host of a relatively powerful radio source. Instead of strong emission lines, the spectrum is more like that of an A star, characteristic of an "E + A" or "post-starburst" galaxy (Dressler & Gunn 1983, Oegerle et al. 1991). These galaxies are composed of old stars typical of elliptical galaxies ("E") and stars thought to have formed in a burst within the past 10^9 years ("+ A"). Dressler and Gunn proposed that the bursts of star formation in E+A galaxies may have been triggered by ram pressure compression of gas in clusters or through galaxy-galaxy interactions and/or mergers. Because mergers and interactions may be causes for the onset of radio emission in galaxy nuclei, it is possible that the same mechanism which produced this E+A galaxy is also responsible for origin of the nuclear radio source. We note that the redshift of $z = 1.394$ for 1608+656 is higher than that of CL 1601+4253 #105, which at $z = 0.7367$ was previously the E+A galaxy with the highest known redshift (Dressler & Gunn 1992).

We know of no other radio galaxy that has such a spectrum, though we are aware that the host around the quasar 3C48 (Boroson & Oke 1982) has Balmer absorption lines typical of A stars. What makes 1608+656 so unusual for an active galaxy is the

absence of narrow emission lines. If it were like 3C48, its nucleus must be exceedingly well hidden. The unusual spectrum might be a result of selective magnification in the lensing of one part of the host galaxy image at the expense of the nucleus. However, we think this unlikely as the similarity of the radio and optical flux density ratios implies that the emission at both wavelengths comes from the same region, i.e., the nucleus of the galaxy.

With the source redshift determined, it is possible to calculate the radio luminosity and linear size of the source. Snellen et al. (1995) found that the total 1.4 GHz flux density from the radio lobes was 12 mJy and that the peaks in the lobes were separated by 50″. Using the redshift $z = 1.394$ for the source and assuming a spectral index $\alpha = -0.5$ (where $S_\nu \propto \nu^\alpha$) gives an emitted luminosity density at 1.4 GHz of $L_{1.4} = 5.8 \times 10^{25}$ W Hz^{-1} and a projected peak separation of 215 h^{-1} kpc. The calculated luminosity density puts 1608+656 on the boundary between FR I and FR II radio galaxies (Fanaroff & Riley 1974), which is usually taken as 10^{25} W Hz^{-1} at 1.4 GHz.

Optical magnitudes were derived from the residual images (for the lens) and the scaled radio models (for the background source), as discussed in the previous section. The lens magnitudes are $m(r) = 20.0^m$, $r-i = 0.7^m$, and the total source magnitudes, from combining all four components, are $m(r) = 20.2^m$, $r - i = 0.6^m$. To obtain luminosities we have calculated k-corrections for the r and i bands using a composite

stellar spectrum of type A9 to F0 V taken from Silva & Cornell (1992) for $\lambda\lambda$ 1100–3200Å and from Heck et al. (1984) for $\lambda\lambda$3750–8900Å. This spectrum closely matches that of the source in the vicinity of the Balmer lines; it is a much better representation of the spectral energy distribution than any of the galaxy SEDs given by Coleman, Wu & Weedman (1980). The resulting k-corrections for $z = 1.394$ are $k(r) = 1.4^m$, $k(i) = 0.6^m$. In order to calculate the intrinsic luminosity of the source, we must also account for the magnification due to lensing. From the lens model given in Paper I, the total magnification is a factor of 5.9, or 1.9 magnitudes. Provided that this magnification limit holds for 1608+656, the implied absolute magnitude for the source is $M(r) = -22.8 - 5\log h^{-1}$. The source is considerably brighter than a typical L^* galaxy, where $M(r)^* = -20.2 - 5\log h^{-1}$ (Loveday et al. 1992; Frei & Gunn 1994), and it approaches the luminosities of the brightest known galaxies. The magnification is calculated assuming that the background source is point-like. If the source is extended, as may be the case for a galaxy, this value for the magnification is only valid when $r\mu \ll D$, where r is the intrinsic source size, μ is the magnification, and D is the distance between images. For the most magnified component A and its nearest neighbor C, this limit corresponds to an intrinsic source size, $r \ll 0\farcs34$, or a projected distance of $r \ll 1.5h^{-1}$ kpc at $z = 1.394$. If the intrinsic source size is larger than this, then the total magnification will be smaller than our model predicts. The result is that the intrinsic source luminosity could be greater than that

derived above. However, the clean residuals displayed in Fig. 2b demonstrate that the magnifications derived from the radio data are approximately correct for modeling the infrared image. Thus we conclude that the calculated source luminosity is fairly accurate. However, strictly speaking, it is a lower limit.

Although we identify 1608+656 as an E+A galaxy based on the strong Balmer absorption lines, there is little spectral evidence for the presence of an old stellar population. The majority of features associated with older stars have wavelengths longward of our spectral coverage. The wavelengths of the Ca II K & H doublet at $z = 1.394$ are covered by the spectrum, but if the doublet is present it is very weak and may be contaminated by atmospheric absorption. The lack of strong evidence for older stars raises the possibility that 1608+656 has had only one burst of star formation. One check on this possibility is to compare the colors of 1608+656 with those of young star clusters to see if a system composed solely of young stars could reproduce the very red $i - K$ color that is seen in 1608+656. We estimated the integrated flux in bands corresponding to K and i for $z = 1.394$ of seven young clusters (Bica, Alloin & Schmitt 1994; Bica & Alloin 1986, 1987). These gave $i - K$ colors ranging from -0.9^m for the youngest cluster (8×10^6 years) to 0.2^m for the oldest clusters (1 to 2×10^9 years). In comparison, 1608+656 has $i - K = 2.7^m$, where the K magnitude is from Paper I. Thus the colors of 1608+656 are significantly redder than expected for only a single population of young stars. This implies that an old

stellar population is also present in 1608+656 unless the continuum is reddened by about $\mathrm{E}(i-K) = 2.5$ as the light passes through the lens. We think that this is unlikely because such reddening would imply an extinction of $A_r = 4.0$, assuming a "van de Hulst #15" theoretical extinction curve (van de Hulst 1949). This gives a corrected absolute magnitude for the background source of $M(r) = -26.8 - 5\log h^{-1}$, which is unrealistically bright.

The infrared image of 1608+656 shows that the lensing galaxy is clearly separated from the three brightest components of the multiply lensed background source (A, B and C; see Fig. 2a), and that the three components are also well separated from each other. The deconvolved image (Fig. 2c) matches the structure in the radio map (see Paper I) extremely well. This is what is expected if the majority of the infrared light originates from the same region as the radio emission. There is a hint, however, of some extended emission between components A and C, and component B appears to be somewhat elongated in the north-south direction. Another possible indication that the background source is extended is that the residual image (Fig. 2b) shows an excess near the location of component B in addition to the lensing galaxy. It is possible that we are resolving more than just the nuclear region of the background source. This is consistent with the "stellar" nature of the spectrum of the lensed source.

In Paper I, the mass model for the lensing galaxy was derived from the positions

and flux densities of the components in the original radio image. The lens can be modeled as a single galaxy with a central mass density which can be expressed in a redshift-independent form as

$$\rho_0 = \frac{9\sigma^{*2}}{4\pi G r_c^2} d_{ls}, \qquad d_{ls} = \frac{D_s}{D_{ls}}, \tag{3.3}$$

where D_s and D_{ls} are the observer-source and lens-source angular diameter distances, G is the gravitational constant, σ^* is related to the central velocity dispersion by $\sigma = \sigma^* \sqrt{d_{ls}}$ and r_c is the scale length of the mass distribution. The redshifts of $z = 0.630$ for the lensing galaxy and $z = 1.394$ for the source give $D_l = 798h^{-1}$ Mpc, $D_s = 886h^{-1}$ Mpc and $D_{ls} = 343h^{-1}$ Mpc. This gives a central mass density of $\rho_0 = 1.25 \times 10^{10}\ h^2\ \mathrm{M}_\odot\ \mathrm{kpc}^{-3}$ and a mass within the Einstein ring radius ($\theta_E = 1\farcs1$) of $3.05 \times 10^{11}\ h^{-1}\ \mathrm{M}_\odot$. Using the K band luminosity of $7.7 \times 10^8 L_\odot$ within θ_E from Paper I gives a mass-to-light ratio within the Einstein radius of $(M/L)_E = 6.98h\ M_\odot/L_\odot$. The expected time delays are $t_C - t_A = 4.0h^{-1}$ days and $t_A - t_B = 40.0h^{-1}$ days.

The large derived mass for 1608+656 is comparable to that of the largest cluster ellipticals and could indicate that a pair of galaxies or a merging galaxy system is doing the lensing. However, the K_s band image of 1608+656 does not support this suggestion and the single galaxy model derived in Paper I is consistent with all the present data. In addition, there is no indication of a galaxy cluster in the r and i band images. Hence, any further refinement to the model will have to await new information.

3.2.4 Conclusions

Our observations of the lensed system 1608+656 have given a redshift of $z = 1.394$ for the background source. The background source is unique among lensed objects in that it is a post-starburst radio galaxy and not a quasar. The new observations are consistent with the mass model derived in Paper I. Hence, three of the four pieces of information needed to determine H_0 from the system are now available: the redshift of the lens, the redshift of the background source, and a working mass model; what is missing is the measurement of a time delay. A monitoring program is underway and there is a strong possibility for measuring a time delay and finding H_0 from this system.

For valuable discussions, we thank Roger Blandford, David Hogg, Steve Myers, Ann Zabludoff, Neal Jackson and Lee Armus. We are grateful to Greg Taylor for helping with the optical observations. We thank the staff at Palomar Observatory for their assistance during our observing runs. CLASS and Infrared astrophysics at Caltech are supported by grants from the NSF. CDF is supported by an NSF Graduate Research Fellowship. DSW acknowledges support of a Hubble Fellowship provided by NASA through grant HF-1040.01-92A from the STScI, which is operated by AURA.

REFERENCES

Bica, E. & Alloin, D. 1986, A&A, 162, 21

Bica, E. & Alloin, D. 1987, A&A, 186, 49

Bica, E. Alloin, D., & Schmitt, H. R. 1994, A&A, 283, 805

Boroson, T. A. & Oke, J. B. 1982, Nature, 296, 397

Coleman, G. D., Wu, C.-C., & Weedman, D. W. 1980, ApJS, 43, 393

Dressler, A. & Gunn, J. 1983, ApJ, 270, 7

Dressler, A. & Gunn, J. E. 1992, ApJS, 78, 1

Fanaroff, B. L. & Riley, J. M. 1974, MNRAS, 167, 31

Frei, Z. & Gunn, J. E. 1994, AJ, 108, 1476

Heck, A., Egret, D., Jaschek, M., & Jaschek, C. 1984, A&A Suppl. Ser., 57, 213

Horne, K. 1986, PASP, 98, 609

Loveday, J., Peterson, B. A., Efstathiou, G., & Maddox, S. J. 1992, ApJ, 390, 338

Lucy, L. B. 1974, AJ, 79, 745

Myers, S. T. et al. 1995, ApJ, 447, L5 (Paper I)

Oegerle, W. R., Hill, J. M., & Hoessel, J. G. 1991, ApJ, 381, L9

Richardson, W. H. 1972, J. Opt. Soc. Am., 62, 55

Silva, D. R. & Cornell, M. E. 1992, ApJS, 81, 865

Snellen, I. A. G., de Bruyn, A. G., Schilizzi, R. T., Miley, G. K., & Myers, S. T. 1995, ApJ, 447, L9

Snyder, D. L., Hammoud, A. M., & White, R. L. 1993, J. Opt. Soc. Am. A: 10, 1014

van de Hulst, H. C. 1949, Rech. Astr. Obs. Utrecht, 11, Part 1

Chapter 4

B2045+265: A New Four-Image Gravitational Lens from CLASS†

C. D. Fassnacht, R. D. Blandford[1], J. G. Cohen, K. Matthews, T. J. Pearson, A. C. S. Readhead, D. S. Womble[2]

Palomar Observatory, 105-24, California Institute of Technology, Pasadena, CA 91125

S. T. Myers

Department of Physics and Astronomy, University of Pennsylvania, 209 S. 33rd St., Philadelphia, PA 19104-6396

†This chapter has been submitted to the *Astronomical Journal*. Based on observations made with the National Radio Astronomy Observatory, which is operated by Associated Universities, Inc., under cooperative agreement with the National Science Foundation; with the NASA/ESA *Hubble Space Telescope*, obtained at the Space Telescope Science Institute which is operated by AURA, Inc. under NASA contract NAS 5-26555; and with the W. M. Keck Observatory, which is operated as a scientific partnership among the California Institute of Technology, the University of California, and the National Aeronautics and Space Administration. The Keck Observatory was made possible by the generous financial support of the W.M. Keck Foundation.

[1]Also Theoretical Astrophysics, 130-33, California Institute of Technology, Pasadena, CA 91125

[2]Present address: Monterey Institute for Research in Astronomy, 200 Eighth St., Marina, CA 93955, dsw@mira.org

I. W. A. Browne, N. J. Jackson, D. R. Marlow, P. N. Wilkinson

NRAL Jodrell Bank, University of Manchester, Macclesfield, Cheshire SK11 9DL, UK

L. V. E. Koopmans

Kapteyn Astronomical Institute, Postbus 800, 9700 AV Groningen, The Netherlands

A. G. de Bruyn[3], R. T. Schilizzi,

NFRA, Postbus 2, 7990 AA Dwingeloo, The Netherlands

M. Bremer, G. Miley

Leiden Observatory, Postbus 9513, 2300 RA Leiden, The Netherlands

Abstract

We have discovered a new gravitational lens in the Cosmic Lens All-Sky Survey (CLASS). The lens B2045+265 is a four-image system with a maximum separation of 1.″9. A fifth radio component is detected, but its radio spectrum and its positional coincidence with infrared emission from the lensing galaxy strongly suggests that it is the radio core of the lensing galaxy. This implies that the B2045+265 lens system consists of a flat-spectrum radio source being lensed by another flat-spectrum radio source. Infrared images taken with the *Hubble Space Telescope* and the Keck I Telescope detect the lensed images of the background source and the lensing galaxy. The lensed images have relative positions and flux

[3]Also Kapteyn Astronomical Institute, Postbus 800, 9700 AV Groningen, The Netherlands

densities that are consistent with those seen at radio wavelengths. The lensing galaxy has magnitudes of $J = 19.2^m$, $m_{F160W} = 18.8^m$ and $K = 17.6^m$ in a $1\farcs9$ diameter aperture, which corresponds to the size of the Einstein ring of the lens. Spectra of the system taken with the Keck I Telescope reveal a lens redshift of $z_\ell = 0.8673$ and a source redshift of $z_s = 1.28$. The lens spectrum is typical of a Sa galaxy. The image splitting and system redshifts imply that the projected mass inside the Einstein radius of the lensing galaxy is $M_E = 4.7 \times 10^{11} h^{-1} M_\odot$. An estimate of the light emitted inside the Einstein radius from the K magnitude gives a mass-to-light ratio in the rest frame B band of $(M/L_B)_E = 20\,h(M/L_B)_\odot$. Both the mass and mass-to-light ratio are higher than what is seen in nearby Sa galaxies. In fact, the implied rotation velocity for the lensing galaxy is two to three times higher than what is seen in nearby spirals. The large projected mass inside the Einstein ring radius may be the result of a significant amount of dark matter in the system, perhaps from a compact group of galaxies associated with the primary lensing galaxy; however, it may also arise from a misidentification of the source redshift. A simple model of the gravitational potential of the lens reproduces the image positions well, but further modeling is required to satisfy the constraints from the image flux density ratios. With further observations and modeling, this lens may

yield an estimate of H_0.

4.1 Introduction

The Cosmic Lens All-Sky Survey (CLASS; Myers et al. 1998) is a large-scale survey for gravitational lenses among flat-spectrum radio sources. The primary goals of CLASS are to find lenses which may be suitable for determinations of the Hubble Constant, H_0 (e.g., Refsdal 1964; Blandford & Narayan 1992), and to study the lensing rate in a large, homogeneous sample in order to place limits on the cosmological constant, Λ (e.g., Turner, Ostriker & Gott 1984; Turner 1990; Fukugita, Futamase & Kasai 1990; Fukugita & Turner 1991). Over 12,000 sources have been observed with the VLA in three sessions – the first in the spring of 1994 (CLASS 1; ~3300 sources), the second in the summer of 1995 (CLASS 2; ~4500 sources) and the third in the spring of 1998 (CLASS 3; ~5000 sources). The vast majority of flat-spectrum radio sources are dominated by emission from a single compact core; all CLASS sources containing multiple compact components are selected as gravitational lens candidates, amounting to 50 – 100 candidates in each phase of the survey. These are followed up with high resolution radio imaging using MERLIN; the best surviving candidates are then imaged using the VLBA. During this procedure, the majority of VLA candidates are rejected based on surface brightness and morphology criteria. The candidates that survive the radio filters are then investigated

further with optical and/or infrared imaging, spectroscopy and more radio imaging. By these means we have discovered 11 new lenses in the survey, in addition to the one reported here. We are also investigating ∼25 promising lens candidates.

We use $H_0 = 100h$ km s^{-1} Mpc^{-1} and, except where noted, assume $q_0 = 0.5$ throughout this paper.

4.2 VLA Observations

The lens system B2045+265 (GB6 J2047+2643) was observed on 1995 September 02 as part of CLASS 2. The observations were made at 8.4 GHz with the VLA in A configuration, giving a resolution of ∼0.″25. Observation and data reduction techniques for the survey will be discussed in Myers et al. (1998). The survey image of B2045+265 shows four components, with a possible detection of a fifth, weak component. The system has a standard lens geometry (e.g., Blandford & Narayan 1992) and is similar in appearance to B1422+231 (Patnaik et al. 1992).

The source was re-observed with the VLA on 1996 December 31. Observations were made in A configuration at 1.4, 4.9, 8.5 and 14.9 GHz. Details of the observations are given in Table 4.1. The source 3C 286 was used as a flux calibrator. Phase calibrators were selected from the VLA calibrator list. The data were calibrated using standard AIPS routines, and maps were made using DIFMAP (Shepherd, Pearson & Taylor 1994). At the frequencies above 1.4 GHz, the source

Table 4.1 RADIO OBSERVATIONS

Array	Date	ν (GHz)	t_{tot} (min)	Angular Resolution
VLA	1995 Sep 02	8.5	0.5	0.″25
VLA	1995 Sep 11	14.9	7	0.″14
VLBA	1995 Nov 12	5.0	35	0.″0025
VLA	1996 Dec 31	1.4	12	1.″5
VLA	1996 Dec 31	4.9	12	0.″43
VLA	1996 Dec 31	8.5	192	0.″25
VLA	1996 Dec 31	14.9	20	0.″14
MERLIN	1997 Nov 30	5.0	750	0.″50

can be characterized as five point components, with no significant extended structure. Hence, the maps were made by fitting five point components to the data and then repeating a cycle of model-fitting and phase self-calibration. The self-calibration time scale was set to the length of the individual scans at each frequency. Both the positions and the flux densities were allowed to vary in the model fitting. At 1.4 GHz the beam size is large compared to the component separation, so the model fitting was done by fixing the component positions at their 8.5 GHz values and varying only the component flux densities. In addition, there were confusing sources in the 1.4 GHz map that had to be included as components in the model.

The final maps are shown in Figures 4.1 – 4.4. In all cases, the morphology seen in the discovery map is duplicated, with five distinct components clearly present in the high-dynamic-range 5 and 8.5 GHz maps. Component positions and flux densities

were obtained using the model fitting procedures in DIFMAP. The brightest component (A) has an 8.5 GHz flux density of 16.55 mJy and is located at 20:47:20.29, +26:44:02.7 (J2000); the positions of the other components relative to component A are given in Table 4.2 (see Figure 4.1 for component labels). The positional uncertainties for the different components are estimated as the beam size at each frequency divided by the signal-to-noise ratio of the component flux densities; the positional errors in the 8.5 GHz map are given in Table 4.2. The largest separation in the system is 1.″9. At all frequencies, five point components are adequate to fit the data. No sign of extended emission is seen, even in the deep 8.5 GHz map. The final component flux densities and RMS noise levels for the maps are given in Table 4.3. In all cases the noise levels are within 5% of the thermal noise expected in the maps.

The 8.5 GHz data were also analyzed to search for polarized emission. The polarization calibration was carried out in AIPS, using 3C 286 as the calibrator. The phase calibrator 2115+295 was observed over a range of parallactic angles and was used to determine the instrumental polarization. The final maps are consistent with no polarized emission above 56μJy/beam (0.34% of the peak unpolarized intensity).

Radio spectra for the five components are shown in Fig. 4.5. Components A – C have very similar spectra, with spectral indices of $\alpha_{1.4}^{4.9} \sim -0.2$ and $\alpha_{4.9}^{15} \sim -0.6$ ($S_\nu \propto \nu^\alpha$). The spectra of components D and E differ from those of the three brighter components. In order to determine which, if either, of these two components is the

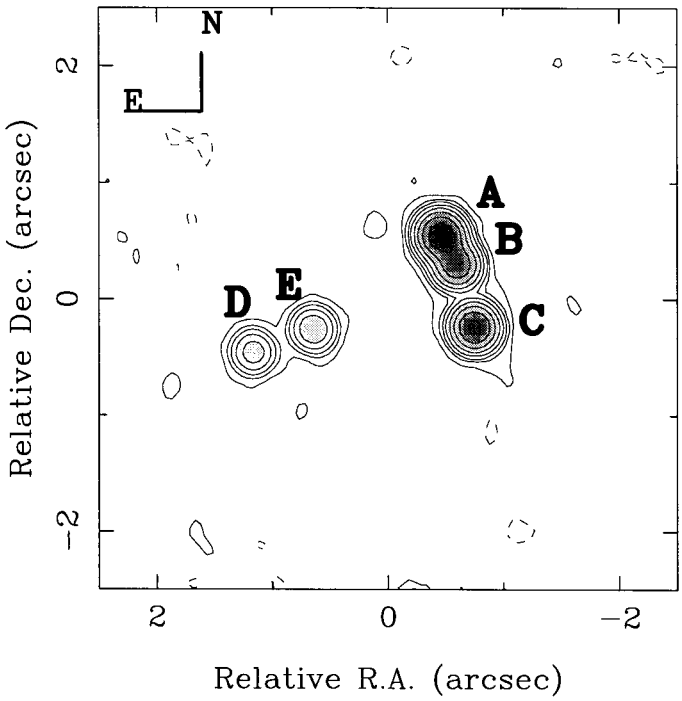

Figure 4.1 December 1996 8.5 GHz map. The contours are (−2.5, 2.5, 5, 10, 20, 40, 80, 160, 320, 640) times the RMS noise level of 0.0145 mJy/beam. Map made by fitting point source components, with flux densities listed in Table 4.3, to the (u, v) data, and restoring with a $0''.27 \times 0''.23$ restoring beam.

counter image to components A, B, and C, flux density ratios are computed for each component with respect to component A. By computing flux density ratios at each frequency, it is possible to avoid uncertainties due to errors in the absolute flux calibration. The resulting curves (Fig. 4.6), normalized to their values at 8.5 GHz, clearly indicate that the spectrum of component E differs from those of the other four components.

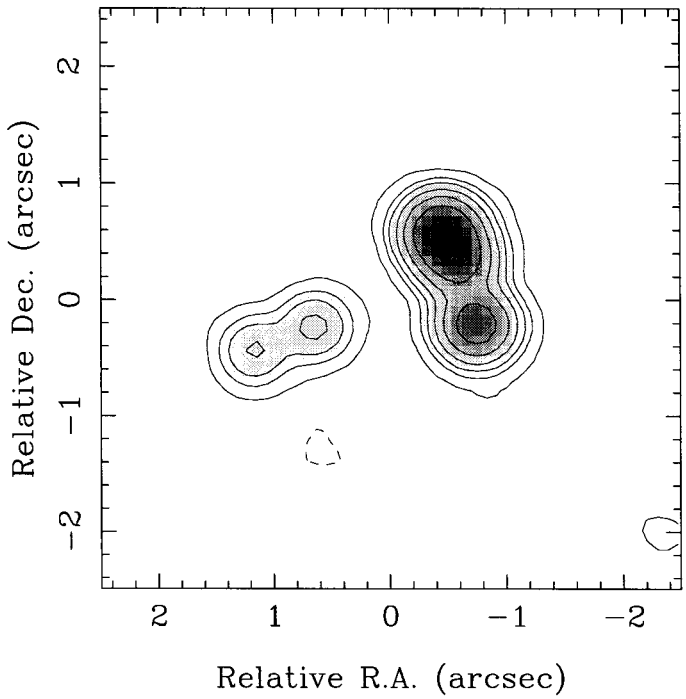

Figure 4.2 December 1996 4.9 GHz map. The contours are (−2.5, 2.5, 5, 10, 20, 40, 80, 160, 320) times the RMS noise level of 0.0621 mJy/beam. Map made by fitting point source components, with flux densities listed in Table 4.3, to the (u, v) data, and restoring with a $0''.44 \times 0''.41$ restoring beam.

Table 4.2 COMPONENT POSITIONS

Component	$\Delta\alpha^a$	$\Delta\delta^a$	σ_x^b
A	0.000	0.000	···
B	−0.134	−0.248	0.001
C	−0.288	−0.789	0.001
D	+1.628	−1.007	0.006
E	+1.121	−0.824	0.005

[a]Positions relative to component A are taken from the 1996 Dec 31 8.5 GHz map. Component A is at 20:47:20.29, +26:44:02.7 (J2000).
[b]Uncertainties in relative positions calculated using the 1996 Dec 31 8.5 GHz data and assuming that the uncertainties in the component flux densities are three times the RMS noise level in the map.

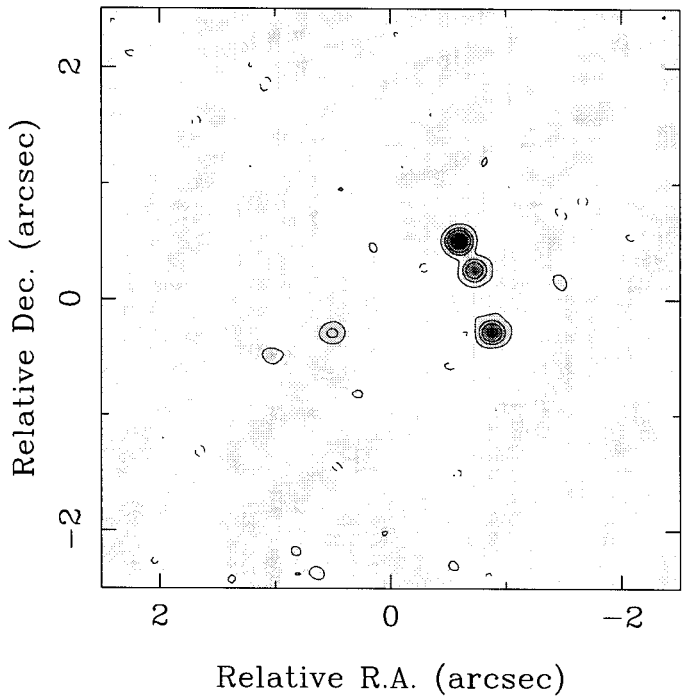

Figure 4.3 December 1996 15 GHz map. The contours are (−2.5, 2.5, 5, 10, 20, 40) times the RMS noise level of 0.139 mJy/beam. Map made by fitting point source components, with flux densities listed in Table 4.3, to the (u, v) data, and restoring with a $0\farcs14 \times 0\farcs13$ restoring beam.

Table 4.3 COMPONENT FLUX DENSITIES

Date	Array	ν (GHz)	S_A (mJy)	S_B (mJy)	S_C (mJy)	S_D (mJy)	S_E (mJy)	RMS (mJy/beam)
1995 Sep 02	VLA	8.5	18.4	9.42	14.8	2.41	1.83	0.28
1995 Sep 11	VLA	14.9	15.5	9.18	11.8	1.22	2.36	0.32
1995 Nov 12	VLBA	5.0	15.8	8.09	8.75	...	...	0.20
1996 Dec 31	VLA	1.4	29.02	15.73	19.92	2.81	2.18	0.08
		4.9	23.40	12.65	15.19	2.68	3.00	0.06
		8.5	16.55	8.90	10.99	1.77	2.34	0.01
		14.9	10.69	5.75	7.13	1.05	1.90	0.14
1997 Nov 30	MERLIN	5.0	16.8	9.82	14.8	2.02	1.53	0.15

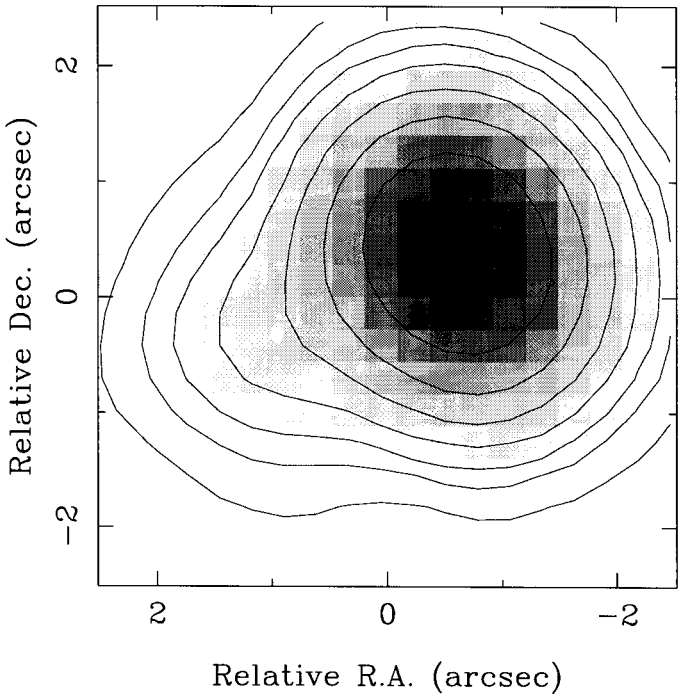

Figure 4.4 December 1996 1.4 GHz map. The contours are (−2.5, 2.5, 5, 10, 20, 40, 80, 160, 320) times the RMS noise level of 0.0784 mJy/beam. Map made by fitting point source components, with flux densities listed in Table 4.3, to the (u, v) data, and restoring with a $1\farcs5 \times 1\farcs4$ restoring beam.

Table 4.4 COMPONENT FLUX DENSITY RATIOS

ν (GHz)	Date	B/A	C/A	D/A	E/A
1.4 GHz	1996 Dec 31	0.54 ± 0.009	0.69 ± 0.010	0.097 ± 0.008	0.075 ± 0.008
4.9 GHz	1996 Dec 31	0.54 ± 0.009	0.65 ± 0.009	0.11 ± 0.008	0.13 ± 0.008
8.5 GHz	1995 Sep 02	0.51 ± 0.051	0.80 ± 0.059	0.13 ± 0.046	0.099 ± 0.046
8.5 GHz	1996 Dec 31	0.54 ± 0.003	0.66 ± 0.003	0.11 ± 0.003	0.14 ± 0.003
14.9 GHz	1995 Sep 11	0.59 ± 0.072	0.76 ± 0.078	0.079 ± 0.062	0.15 ± 0.062
14.9 GHz	1996 Dec 31	0.54 ± 0.044	0.67 ± 0.047	0.098 ± 0.046	0.18 ± 0.063

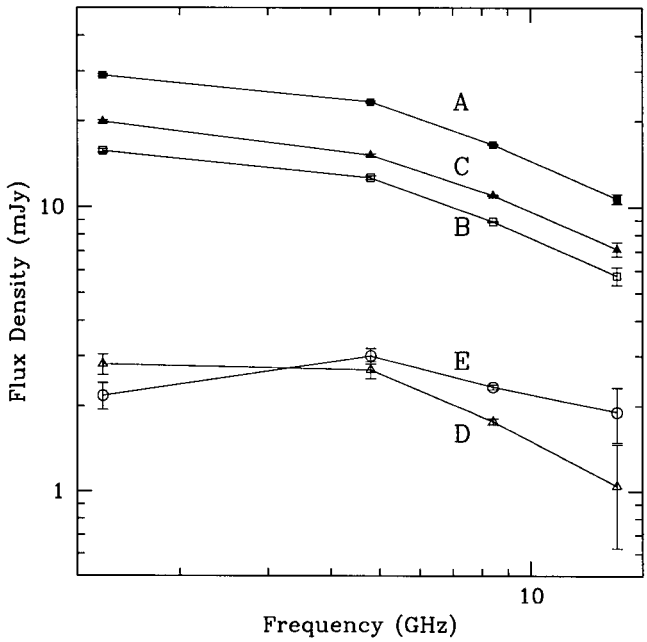

Figure 4.5 Radio spectra of the five components in the B2045+265 system. The error bars are 3 σ errors, based on the RMS noise in the maps.

4.3 MERLIN and VLBA Observations

A 5 GHz MERLIN observation of B2045+265 was made on 1997 November 30, with approximately 12.5 hr total integration on source. The final map (Fig. 4.7) has an RMS noise level of 0.146 mJy/beam and an angular resolution of 60 milliarcsec (mas). The data are well fitted by 5 point sources, with flux densities given in Table 4.3. However, there are some indications of additional emission around components A and C in the residual map, at the $2-3\,\sigma$ level. The excess emission may indicate that the images are slightly resolved. If mas-scale structure can be detected in the images, it can be used to put constraints on the lens model. The transformation matrix between

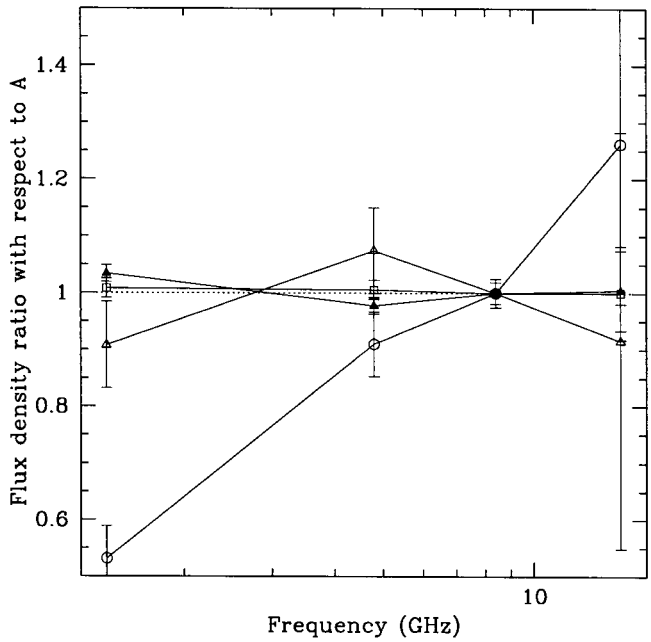

Figure 4.6 Flux density ratios for components B (open squares), C (filled triangles), D (open triangles) and E (open circles) with respect to component A. All curves have been normalized to their 8.5 GHz point. Error bars are calculated by propagating the RMS noise in the maps at each frequency.

corresponding positions in the resolved images provides crucial limits on the lensing potential by fixing its second derivatives at those points (e.g., Gorenstein et al. 1988). Observations with high angular resolution and dynamic range are needed to search for such structure. A 5 GHz VLBA snapshot (35 min total integration on source) of this system was made on 1995 November 12. In this observation, which has an angular resolution of $\sim$1 mas, the three brightest components are detected. The flux density of each component is only $\sim$60% of its flux density in the 5 GHz VLA observations. Once again, this may indicate the presence of extended mas-scale structure in this source

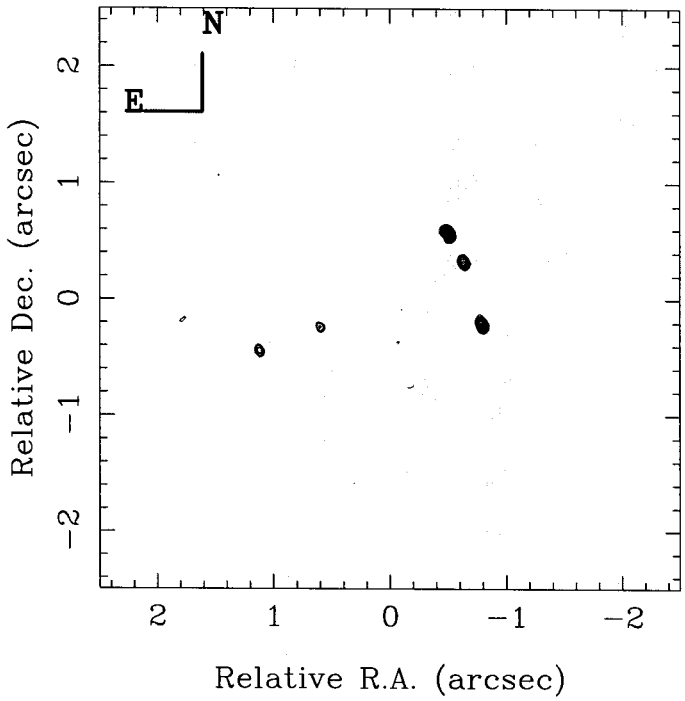

Figure 4.7 MERLIN map. Components A, B, and C may be slightly resolved.

which could be detected in more sensitive observations. Deep VLBA observations of B2045+265 have now been scheduled which may produce maps with sufficient dynamic range to detect extended structure in the images.

4.4 Infrared Imaging

4.4.1 NIRC

The system was imaged on 1996 July 31 using the Near Infrared Camera (NIRC; Matthews & Soifer 1994) on the W. M. Keck I Telescope. Images were taken in both J and K bands, with 45 one-minute exposures in K and 27 one-minute exposures in

J. In order to estimate the point-spread function (PSF), 18 exposures of a star at a distance of 1.47 arcmin were interleaved with the exposures on the lens in each band. The seeing was $0\farcs45$–$0\farcs90$ in K and $0\farcs75$–$1\farcs15$ in J during the observations.

The dark current level was subtracted from each image, and then sky-subtraction and gain correction were performed. The sky and gain frames used for each image were constructed from images observed directly before and after it. The individual frames were aligned by centroiding on a star which appeared in each frame. For the highest sensitivity in the final images, all 45 frames in K and all 27 frames in J were combined into mosaics. The K band mosaic is shown in Fig. 4.8 and close-ups of the lens system in the two bands are shown in Figs. 4.9 and 4.10. The two main features in the images of the lens system are a short arc, corresponding to the three brightest radio images, and the lensing galaxy, which is located $1\farcs2$ from the arc. Spectroscopy has shown that the object seen $2''$ to the left of the lens system in Fig. 4.8 is a star.

4.4.2 NICMOS

B2045+265 was observed with the *Hubble Space Telescope* using the Near Infrared Camera/Multi-Object Spectrometer (NICMOS) on 1997 July 14. The NIC-1 camera was used, which has a pixel scale of 43 mas. Two exposures were taken giving a total exposure time of 2624 sec. The images were subjected to the standard NICMOS

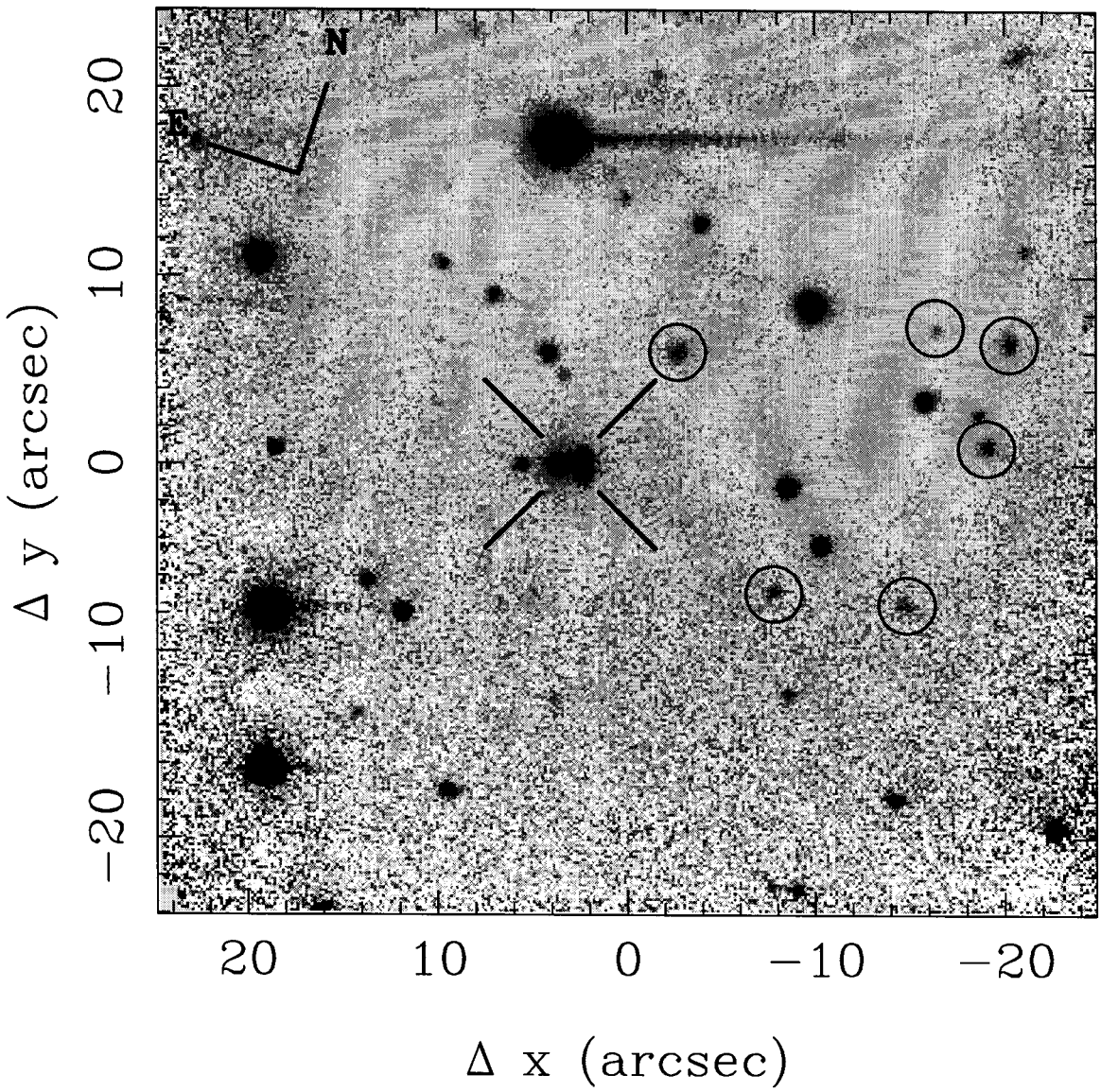

Figure 4.8 NIRC K band mosaic of the B2045+265 field. The lens system is marked with the crosshairs, with the lensing galaxy to the left and an arc of emission from the background source to the right. The object 2″ to the left of the galaxy is a star. The circled objects are extended and may be galaxies in a group at the redshift of the lens (see § 7.3).

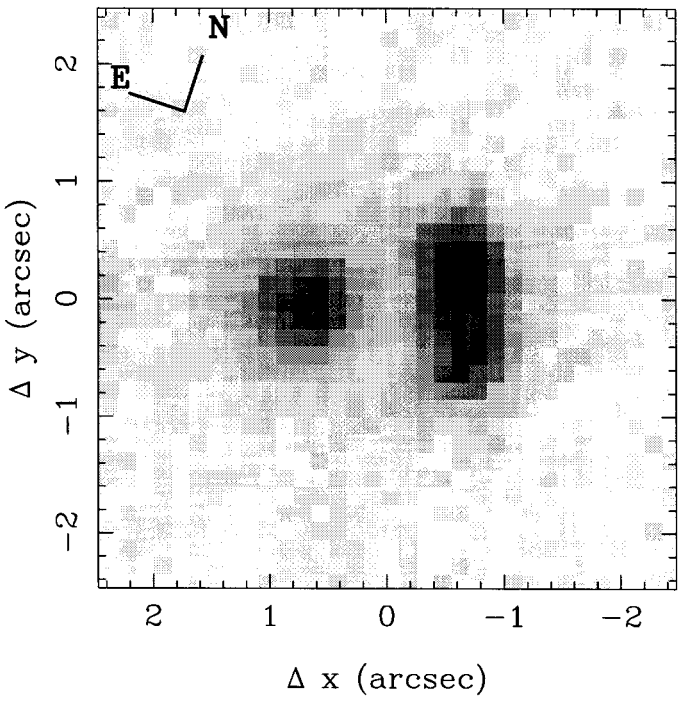

Figure 4.9 NIRC K band image of B2045+265. The lensing galaxy is to the left, perhaps with some emission being contributed from component D. An arc consisting of emission from components A, B and C is to the right.

calibration pipeline involving bias and dark current subtraction, linearity and flat-field correction, photometric calibration and cosmic ray identification and removal. The final image (Fig. 4.11) clearly shows the three brightest lensed images and the lensing galaxy. The relative positions of components A, B, and C match those seen at radio wavelengths to within 0.″01. In addition, the galaxy location matches the position of radio component E to within the errors. There appears to be low surface brightness emission between images B and C, indicating the possibility that extended optical emission from the background source is being lensed into an arc-like structure. The expected position of component D is marked in the figure.

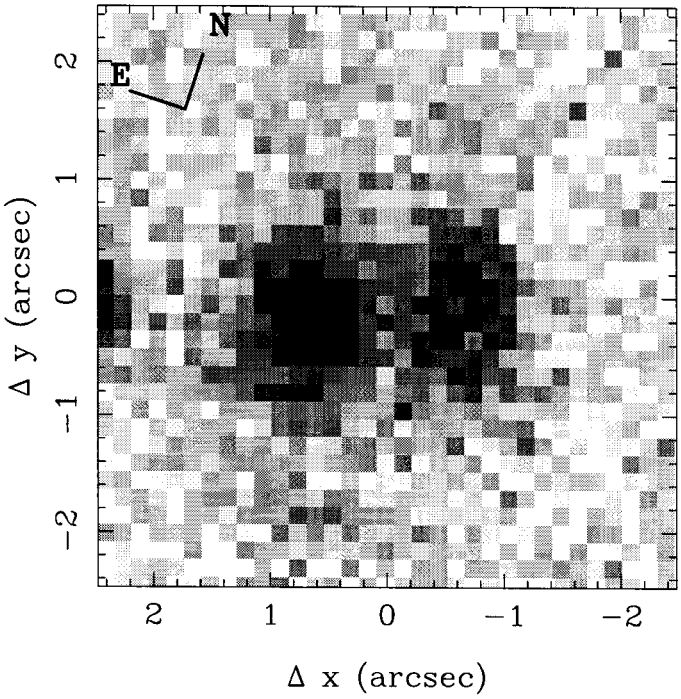

Figure 4.10 NIRC J band image of B2045+265.

4.4.3 Photometry

Because the NICMOS image has high spatial resolution, it is possible to compute magnitudes for the individual images of the background source in the F160W bandpass (roughly corresponding to the ground-based H band). Magnitudes were calculated using both the DAOPHOT package (Stetson 1987) in IRAF[4] and the SExtractor package (Bertin & Arnouts 1996). First, the magnitudes of the three bright lensed images were calculated using 0.″26 diameter apertures. Next, an empirical PSF, constructed from radial profiles of stars in the field, was fitted to the emission from

[4]IRAF (Image Reduction and Analysis Facility) is distributed by the National Optical Astronomy Observatories, which are operated by the Association of Universities for Research in Astronomy under cooperative agreement with the National Science Foundation.

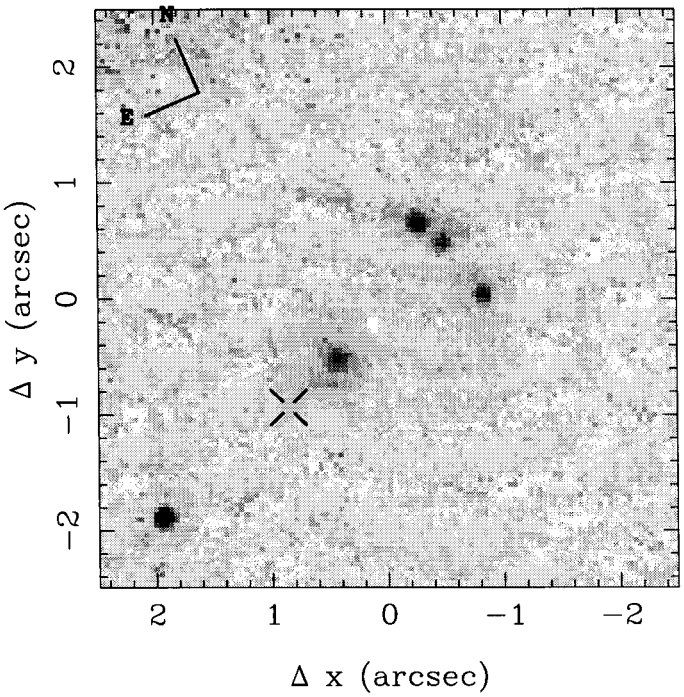

Figure 4.11 NICMOS F160W image of B2045+265. The extended object near the center of the image is the lensing galaxy. The crosshairs mark the expected position of component D.

the lensed images and the star near the lensing galaxy. The scaled PSFs were then subtracted from the data and the lens magnitude was calculated using a 1.″9 diameter aperture. This aperture was chosen to match the largest image separation in the system, which is approximately equal to twice the Einstein radius of the lens. The aperture diameter corresponds to $7.9\,h^{-1}$ kpc at the redshift of the lens. The PHOTFNU header card was used to convert count rates in the image into flux densities into Janskys and then a Vega zero-point of 1087 Jy was assumed to get the F160W magnitudes. For comparison with the NIRC photometry (see below), the magnitude of the "arc" defined by the three lensed images of the background source

was also computed. The DAOPHOT and SExtractor packages produced magnitudes that were consistent within the errors of the sky determination. The final magnitudes are given in Table 4.5. It should be possible to search for extinction caused by the lensing galaxy by comparing the F160W and radio flux density ratios of the lensed images. However, the uncertainties in the NICMOS component magnitudes are large ($\sim 0.2^m$) and thus the F160W flux density ratios, B/A = 0.69 and C/A = 0.76, are consistent with the radio flux density ratios at the 1 σ level. The upper limit on the brightness of a point-source at the location of component D is $m_{F160W} > 22^m$. This is not surprising since component D should be 2.5^m fainter than A.

It is considerably more difficult to do photometry on the NIRC images because the seeing disk is large compared to the component separations. Instead of finding magnitudes of the individual lensed images, the magnitude of the "arc" was calculated by centering a rectangular aperture of width 0.″9 and height 1.″8 on the "arc." The sky was estimated from regions directly to the north, west and south of the aperture. Once again, the DAOPHOT package was used to subtract the emission from the lensed images and the star from the data before the lens galaxy magnitude was calculated. The photometric zero points were estimated by observing the infrared standard star SJ9184 ($K = 11.82$, $J = 12.18$; Persson et al. 1998), which was observed in each band prior to the lens and PSF star exposures. The zero points in the two observed bands were $K_0 = 22.44$, and $J_0 = 22.92$. The J and K magnitudes of the lensing galaxy

Table 4.5 COMPONENT DATA (INFRARED OBSERVATIONS)

Component	$\Delta\alpha^a$	$\Delta\delta^a$	J	m^b_{F160W}	K
A[c]	0.00	0.00	···	20.6	···
B[c]	−0.13	−0.23	···	21.0	···
C[c]	−0.28	−0.78	···	20.9	···
Lens Galaxy[d]	+1.10	−0.80	19.2	18.6	17.6
"Arc"	···	···	19.6	18.7	17.3

[a]Relative positions in arcseconds calculated with respect to component A after a −23° rotation was performed to match the radio image orientation.
[b]F160W magnitudes computed assuming that the Vega zero point is 1087 Jy.
[c]Magnitudes computed in a 0.″26 diameter aperture.
[d]Magnitudes computed in a 1.″9 diameter aperture.

and "arc" are given in Table 4.5.

4.5 Optical Spectroscopy

Spectra of B2045+265 were taken with the Low Resolution Imaging Spectrograph (LRIS; Oke et al. 1995) on the Keck I Telescope on 1996 June 18–19. A 1″ longslit and the 300 gr/mm grating were used, giving a pixel scale of 2.44 Å/pix. The slit was positioned at P.A. = 112°, in order to have the highest probability of spatially separating the emission of the background source from that of the lensing galaxy. Seven 1500 sec exposures were taken, four on the first night and three on the second night.

The spectra were reduced using standard IRAF tasks. The average seeing over the two nights was sufficiently good to enable the extraction of separate spectra at

the positions of the lensing galaxy and the brightest source emission. The spatial separation between lens and source spectra is 1.″3, matching the separation between the lens and the three bright lensed images seen in the NICMOS image. The final spectra have a wavelength range $\lambda\lambda$4309–9361Å. Flux calibration was performed using the standard star Feige 110 (Oke 1990) which was observed at the end of each night. An atmospheric absorption template was created by fitting a power law to the flux-calibrated spectrum of the BL Lac object 2155–304. This template was used to remove atmospheric features from the B2045+265 spectra. The individual exposures were weighted by the squares of their signal-to-noise ratios and combined to create the final lens and source spectra shown in Figs. 4.12 and 4.13.

The lens system was re-observed with LRIS on 1996 September 15 with a setup similar to that used in the earlier observations, but with wavelength coverage $\lambda\lambda$2344–7398Å. Two 2000 sec exposures were taken and the data were reduced using a method similar to that described above. In this case, however, the chip response was not removed from the final spectrum. The seeing was worse than in the earlier observations; as a result, the source and lens spectra could not be extracted separately and both source and lens features are seen in the final spectrum (Fig. 4.14).

The reduced spectrum of the lensing object is typical of a Sa galaxy (e.g., Kennicutt 1992). It shows [O II] λ 3727Å emission at 6962Å, Ca II K λ3934Å absorption at 7345Å, Ca II H λ3968Å absorption (possibly blended with Hϵ λ3970Å) at

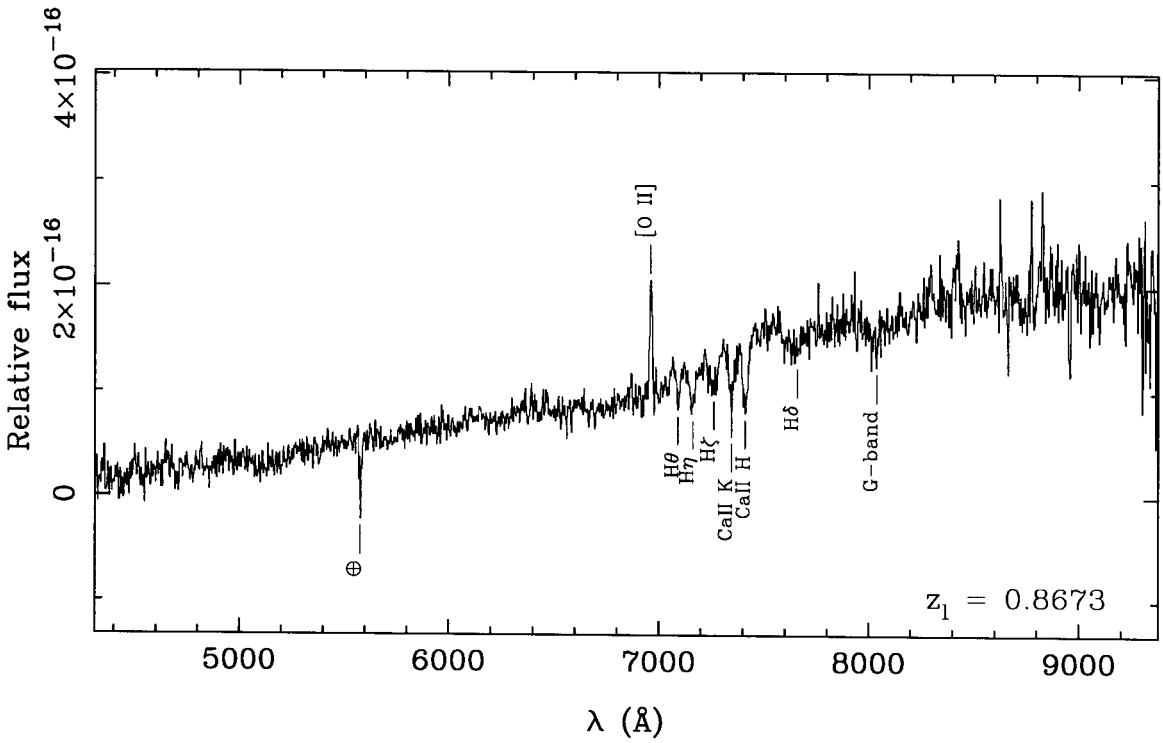

Figure 4.12 LRIS spectrum of the lensing galaxy from data taken on 1996 June 18–19.

7411Å, and Hη and Hθ $\lambda\lambda$ 3835, 3797Å absorption at 7159Å and 7092Å, respectively. These spectral features establish the lens redshift as $z_\ell = 0.8673 \pm 0.0005$, where the uncertainty in the redshift is determined from the RMS scatter in the redshifts derived from the [O II], Ca II K, Hη and Hθ lines. The source spectrum shows a broad emission line at $\lambda = 6396$Å. No other broad emission features are seen in the spectrum, which ranges from 4300 to nearly 9400Å. We identify the line as Mg II λ2800Å, which implies $z_s = 1.28$, because it is the only broad emission line that is so isolated in typical quasar spectra (e.g., Boyle 1990; Francis et al. 1991). The second set of spectra were taken in order to search for C III] λ1909 emission, expected to

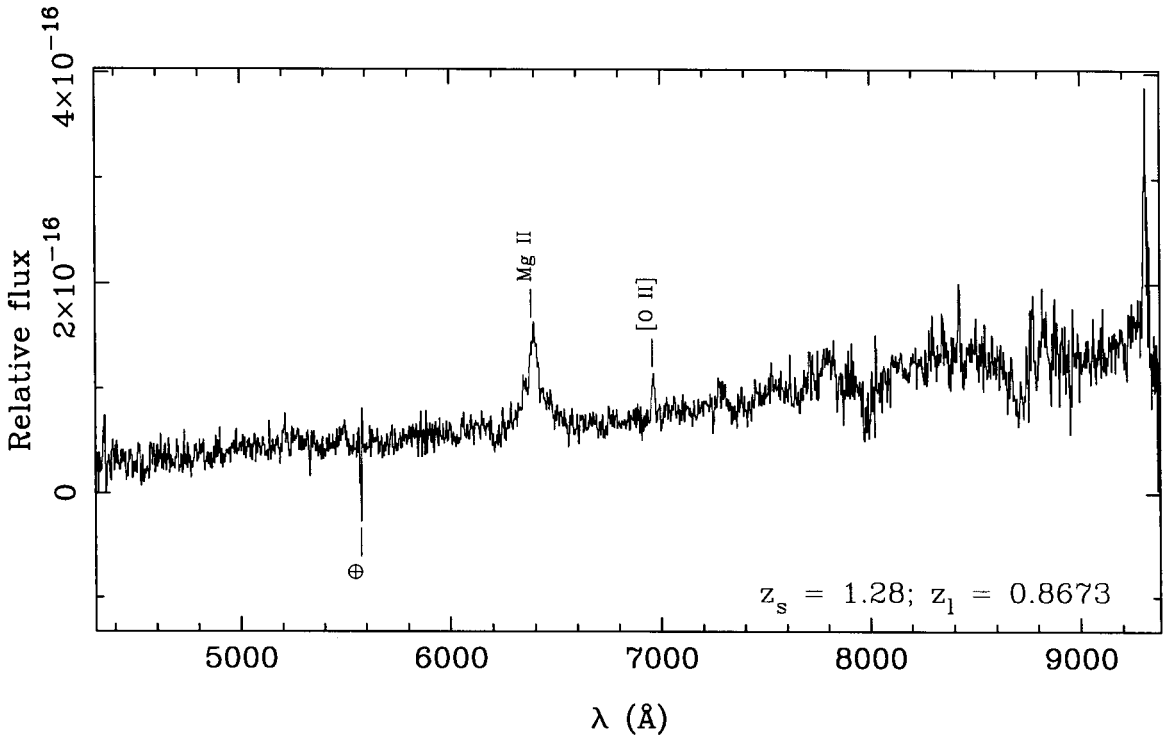

Figure 4.13 Spectrum of background source taken on 1996 June 18–19. There is some contamination from light from the lensing galaxy, which produces the [O II] emission line.

fall at $\sim$ 4350Å. No line was seen at this position, although the sensitivity in this part of the spectrum is low and the presence of a weak line is not ruled out. Other possible identifications for the observed emission line (e.g., Hβ, C III], C IV, Lyα) would imply the presence of strong emission lines in parts of the spectrum in which the signal-to-noise ratio is high, none of which we see. We conclude that the line is correctly identified and the source lies at redshift $z_s = 1.28 \pm 0.01$, where the uncertainty in the redshift is estimated from uncertainties in finding the line centroid in both the emitted and the observed frames.

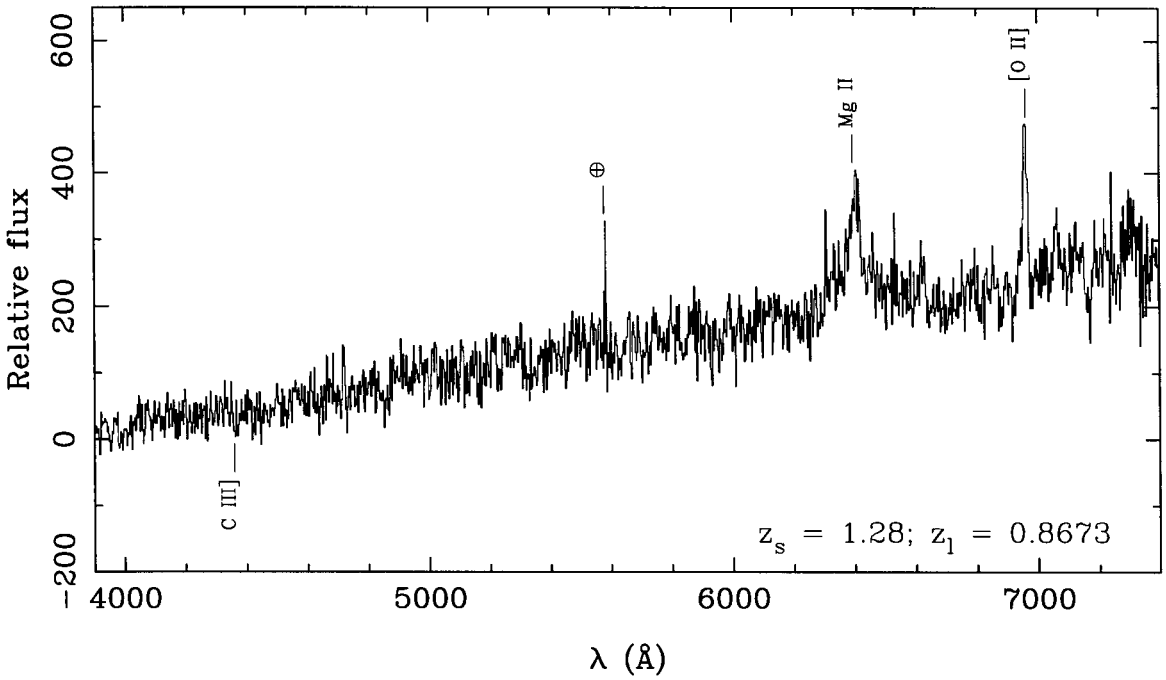

Figure 4.14 Wavelength calibrated spectrum taken on 1996 Sept. 15. Both source and lens features are seen in the spectrum. The position of the expected C III] emission is marked. The signal drops to zero blueward of 4000Å.

4.6 Source Variability

In order for a lens system to be used to measure H_0, the background source must be variable so that time delays can be measured. We use two methods to search for evidence of variability in the background source in B2045+265. The first is to examine the component flux density ratios at different epochs. The ratios are not affected by errors in the absolute flux calibration and so any detected changes in the flux density ratios reflect actual changes in the flux density of the background source. A comparison of the 8.5 GHz observations made in September 1995 with those made in December 1996 shows small changes in the ratios of the component flux densities,

but not at a significant level.

The second method is to monitor the total 22 GHz flux density of the B2045+265 lens system. Daily observations of the system were made with the 40 m telescope of the Owens Valley Radio Observatory during the periods 1996 May 18 – September 03 and 1996 November 04 – 22. The data were calibrated using the CMBPROG package (Leitch 1998). A 15% ± 3% change in total flux density was observed in November 1996 over a period of less than a week. Because several other sources being monitored showed no change in flux density during the same period, the observed change in flux density may indicate variability in the background source. However, it is also possible that the detected variability is due to changes in component E, which has a radio spectrum that is flatter that that of the lensed images. To determine which of the components is varying requires high angular resolution monitoring of the system with the VLA.

4.7 Discussion

4.7.1 The Nature of Component E

The detection of five unresolved radio components in the B2045+265 system raises the possibility that component E is the fifth lensed image of the background source. We believe, however, that component E is instead associated with the lensing galaxy.

Although standard lensing models can produce five images in configurations similar to that seen in the B2045+265 system (e.g., Blandford & Narayan 1992), the central fifth image tends to be highly demagnified with respect to the other images. This behavior is not seen in B2045+265; in fact, component E is brighter than component D at high frequencies. In addition, the radio spectrum of component E (Figs. 4.5 and 4.6) differs sufficiently from the spectra of the other four components to suggest that component E is not related to the other components. Finally, the radio emission of component E is spatially coincident with the infrared emission from the lensing galaxy (see §4.4.2). We therefore conclude that component E is indeed associated with the lensing galaxy. It thus appears that we have discovered a radio galaxy lensing a radio-loud quasar. Of previously known lens systems, only 2016+112 (Lawrence et al. 1984) may have radio emission associated with a lensing galaxy. However, recent observations of 2016+112 suggest that the radio emission of its component C1 may be lensed emission from a (separate) background source (Garrett et al. 1996).

The flat radio spectrum of component E in B2045+265 is typical of an active galactic nucleus. If component E is, indeed, associated with the lensing galaxy, then the radio position of E gives an accurate location for the nucleus of the lensing galaxy. The location of the center of the lensing galaxy relative to the lensed images is a key component in models of the lensing potential (see §4.7.2). An *a priori* knowledge of the relative position of the center of the lensing galaxy provides strong constraints on

lens models.

4.7.2 Preliminary Lens Model

We model the lens potential as a singular isothermal sphere potential with "mixed" shear (Kochanek 1991), in which the scaled lensing potential can be expressed as:

$$\psi = br + \gamma br \cos 2(\theta - \theta_\gamma).$$

Locations in the image plane relative to the lens center are given by $\vec{x} = (r, \theta) = (x, y)$. The critical radius of the isothermal sphere is given by b, and γ and θ_γ give the magnitude of the shear and its position angle. In the modeling process we have used an *astronomical* rather than mathematical coordinate system such that $x \equiv \Delta\alpha$ and $y \equiv \Delta\delta$. The polar coordinates are defined in the usual way, with $r = (x^2 + y^2)^{1/2}$ and $\theta = \arctan(y/x)$. This results in a *left-handed* coordinate system.

Although the image positions are defined relative to the position of component A, they are treated as absolute positions. Thus, both the lens position (x_ℓ, y_ℓ) and source position (x_s, y_s) are included as parameters in the model. We assume that component E marks the nucleus of the lensing galaxy and fix the lens position at that location, leaving five varying parameters and eight observational constraints (x and y for each of the four images).

A downhill simplex routine (Press et al. 1992) is used to minimize the difference

Table 4.6 LENS MODEL

Parameter	Value
b	$1\farcs076$
γ	0.104
θ_γ^a	$69\fdg4$
x_ℓ^a	$+1\farcs12^b$
y_ℓ^a	$-0\farcs82^b$
x_s^a	$+0\farcs72$
y_s^a	$-0\farcs67$

[a]The positions relative to component A (x, y) and θ_γ are defined in a *left-handed* coordinate system. See §4.7.2.
[b]Held fixed during model fitting.

between the observed and model positions, expressed as:

$$\chi^2 = \sum_i \left[\frac{|\vec{x}_m - \vec{x}_o|^2}{\sigma_x^2} \right]$$

where the subscripts m and o refer to the model and observed values, respectively. The positional errors are defined to be the 8.5 GHz beam size divided by the signal-to-noise ratio of the component in the 8.5 GHz map. To avoid biases introduced by the choice of starting values, we repeat the process with a grid of choices of initial conditions containing 3^n values, where n is the number of varying parameters in the model fitting. The best-fit parameters for the model are given in Table 4.6, and the model is shown graphically in Fig. 4.15. The observed image positions are recovered by this simple model of the lensing potential, with RMS image displacements of $<$20 mas.

Radio images are unaffected by microlensing, so it is possible to use the flux density ratios of the images to constrain the model of the lensing potential further.

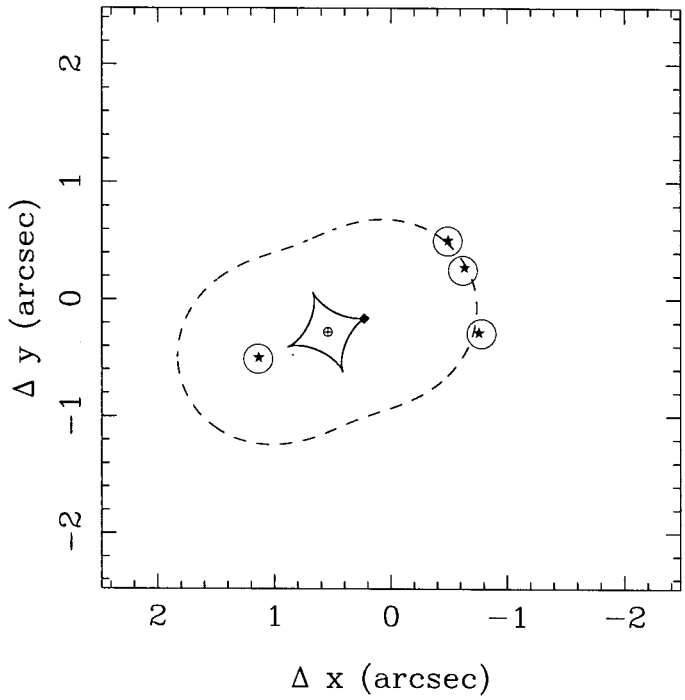

Figure 4.15 Lens model showing critical curve (broken line), caustic curve (solid line), lens center ($\oplus$), source position (filled diamond) and model image positions ($\star$). The four circles are centered on the observed image positions.

The observed flux density ratios, however, are difficult to reproduce with a simple model such as the one presented above. Although this simple model is adequate to recover the four image positions, it does not reproduce the relative magnifications of images A, B, C. The reason for this is easy to see. If, as we have assumed, the potential is smooth, then we can perform a Taylor expansion of it about the location of image B. If we approximate the images as collinear, then the highest order essential terms in this expansion are quadratic in the coordinate perpendicular to the A – C line and quartic parallel to this line. Higher order terms are, by assumption, ignorable. It is then possible to show that in the limit of small image separations there

are several scaling laws including $S_B \sim S_A + S_C$, i.e., the flux of the central image approaches the sum of the fluxes of the other two images (Kovner & Paczyński 1988; Blandford 1990). This is clearly violated in this source, which indicates strongly that the potential is not smooth on the scale of the A – C image separation.

In order to improve upon our model, we have introduced higher order terms in the potential such as might be produced by a local mass perturbation. Specifically we expand the potential around images A and C to third order along the A - C line and to fourth order around image B. We then impose continuity of the potential and its first two derivatives midway between A and B and midway between B and C. There are then three observable quantities, the ratio of the image separations and the ratios of the image fluxes, that can be used to solve for the coefficients in these Taylor expansions. Performing this exercise leads to the conclusion that adding a small, positive mass perturbation centered on a point located $0\farcs11$ from B towards C suffices to recover the flux ratios as well as the image locations. (This perturbation might be caused by a spiral arm, for example (cf Mao & Schneider 1997)). The ratio of the (almost certainly unmeasurable) time delays $\Delta t_{BA}/\Delta t_{BC}$ is now found to be 0.2; however, the delay Δt_{BD} should be quite robust to this perturbation within a given global model. In conclusion, none of the existing observations challenge the gravitational lens interpretation that we present here.

4.7.3 Properties of the Lensing Galaxy

Properties of the lensing galaxy can be derived by using the fact that it is acting as a gravitational lens. For example, the mass within the Einstein ring of a lens is (e.g., Blandford & Narayan 1992):

$$M_E \approx 1.24 \times 10^{11} \left(\frac{\theta_E}{1''}\right)^2 \left(\frac{D}{1\mathrm{Gpc}}\right) M_\odot, \quad D \equiv \frac{D_\ell D_s}{D_{\ell s}}$$

where θ_E is the angular radius of the Einstein ring and D_ℓ, D_s, and $D_{\ell s}$ are the angular diameter distances between observer and lens, observer and source and lens and source, respectively. The angular diameter distance between two objects at z_i and z_j ($z_i < z_j$) is given by (Carroll, Press, & Turner 1992):

$$D_{ij} = \frac{c}{H_0(1+z_j)|\Omega_k|^{1/2}} \mathrm{sinn}\left(|\Omega_k|^{1/2}\mathcal{I}(z_i, z_j)\right),$$

where

$$\mathcal{I}(z_i, z_j) = \int_{z_i}^{z_j} \frac{dz}{[(1+z)^2(1+\Omega_M z) - z(2+z)\Omega_\Lambda]^{-1/2}}$$

and $\mathrm{sinn}(x)$ is defined as $\sinh(x)$ for $\Omega_k < 0$, x for $\Omega_k = 0$, or $\sin(x)$ for $\Omega_k > 0$, respectively. The Ω terms are defined in the standard fashion:

$$\Omega_M = \frac{8\pi G}{3H_0^2}\rho_0, \quad \Omega_\Lambda = \frac{\Lambda}{3H_0^2}, \quad \Omega_k = -\frac{kc^2}{R_0^2 H_0^2}.$$

The integral $\mathcal{I}$ has an analytic solution for $\Omega_\Lambda = 0$, and if $\Omega_M = 1$ the angular diameter distance acquires the simple form

$$D_{ij} = \frac{2c}{H_0}\frac{1}{(1+z_j)}\left(\frac{1}{(1+z_i)^{1/2}} - \frac{1}{(1+z_j)^{1/2}}\right).$$

For B2045+265, the lens redshift is secure. The source redshift, based on one emission line, is less certain. For this reason, we express the physical quantities derived in this section as functions of the source redshift. We will also assume, for ease of discussion, an Einstein-de Sitter cosmology. The effects of varying the source redshift and the cosmological model are presented in Table 4.7. The angular diameter distances for this system are $D_\ell = 860\,h^{-1}$Mpc and

$$\frac{D_s}{D_{\ell s}} = \frac{1.8673[(1+z_s)^{1/2}-1]}{(1+z_s)^{1/2}-1.8673}.$$

The mass enclosed within the Einstein ring radius is calculated by assuming that the maximum image separation is a measure of $2\theta_E$; i.e., that θ_E=0.″95. This assumption yields $M_E \approx 9.6\times10^{10}(D_s/D_{\ell s})h^{-1}M_\odot$ for the B2045+265 system. Note that M_E represents the *total* mass contained in the cylinder with projected radius R_E. The speed of a particle moving in a circular orbit (v_{circ}) at the Einstein ring radius is derived from M_E by assuming that the mass distribution of the lensing galaxy is an isothermal sphere. A simple calculation is used to convert M_E to the mass inside the sphere of radius R_E. The value for v_{circ} follows directly from the mass inside the sphere. The luminosity of the lens inside R_E can be estimated by converting its K magnitude to rest-frame M_B and M_V magnitudes. The k-correction for the lens redshift and rest-frame $(V-K)$ and $(B-V)$ colors for typical Sa galaxies are taken from Poggianti (1997). The resulting luminosities are $(L_V)_E = 2.92\times10^{10}h^{-2}L_{\odot,V}$ and $(L_B)_E = 2.36\times10^{10}h^{-2}L_{\odot,B}$. The rest-frame B band mass-to-light ratio becomes

$(M/L_B)_E = 4.1(D_s/D_{\ell s})h(M/L_B)_\odot$.

Inserting the source redshift derived from the optical spectra (§4.5) yields a lens mass of $M_E \approx 4.7 \times 10^{11} h^{-1} M_\odot$ within the Einstein ring radius ($\sim 4h^{-1}$ kpc at the redshift of the lens). This mass implies a circular velocity at R_E of 570 km/sec, two to three times the velocities seen in both nearby (e.g., Rubin et al. 1985) and more distant ($0.1 < z < 1$; Vogt et al. 1996) spiral galaxies. The Einstein ring mass-to-light ratios are $(M/L_V)_E = 16h(M/L_V)_\odot$ and $(M/L_B)_E = 20h(M/L_B)_\odot$. These mass-to-light ratios are not unusual for lens systems (e.g., Fig. 7 of Keeton, Kochanek, & Falco 1998), although they are higher than expected given the redshift of the lens and assumptions about the luminosity evolution of lens galaxies (Keeton et al. 1998). The large lensing mass required to produce the observed image separation is a result of the relative closeness of the background source to the lens in redshift space. There are several possible explanations for the unusually high projected mass.

Compact groups of galaxies associated with the primary lensing galaxies have been discovered in recent observations of two lens systems (1115+080 and B1422+231; Kundić et al. 1997a,b; Tonry 1998). We are conducting observations of the B2045+265 field to search for evidence of a group associated with the lensing galaxy (see also Fig. 4.8). The high contamination rate by field galaxies (~85% at $z \sim 1$;

Postman, Lubin, & Oke 1998), however, makes high-redshift groups difficult to detect. If such a group exists and is gravitationally bound, its gravitational potential can enhance the image splitting by the lensing galaxy. In such a scenario, we would overestimate the mass of the lensing galaxy.

Another explanation for the high projected mass inside the Einstein ring is that the lens may be one of a close pair of possibly merging galaxies. This situation has been observed in the case of the CLASS lens 1608+656. The initial observations revealed an Einstein ring projected mass of $M_E \approx 3.1 \times 10^{11} h^{-1} M_\odot$, corresponding to $v_{circ} = 440\,\mathrm{km/sec}$ (Myers et al. 1995; Fassnacht et al. 1996). Later HST imaging showed that the lens is composed of a very close pair of galaxies, explaining the high mass and ellipticity required for the 1608+656 system (Jackson et al. 1997). We are unable to determine unequivocally whether two galaxies are present in the B2045+265 system because the sensitivity of our NICMOS observation is too low. More sensitive NICMOS and WFPC2 observations of B2045+265 are needed to test the two-galaxy hypothesis.

A third possibility is that the source redshift or the assumed cosmology (or both) are in error. We examine the results of varying the source redshift by assigning different identifications to the emission line seen in Fig. 4.13. We then re-calculate the physical parameters associated with the lens in three different cosmological models: $(\Omega_M, \Omega_\Lambda) = (1, 0)$, $(0.2, 0)$, and $(0.2, 0.8)$. We find that the effects of changing z_s are

Table 4.7 LENS PARAMETERS

Line ID	z_s	Ω_M	Ω_Λ	D_ℓ (h^{-1} Mpc)	D_s (h^{-1} Mpc)	$D_{\ell s}$ (h^{-1} Mpc)	M_E ($10^{11}h^{-1}M_\odot$)	$(M/L_B)_E$ ($h(M/L_B)_\odot$)	v_{circ} (km/s)
Mg II	1.28	1.0	0.0	860	890	180	4.7	20	570
		0.2	0.0	1000	1100	240	5.3	16	560
		0.2	0.8	1200	1300	340	5.1	11	500
C III]	2.35	1.0	0.0	860	810	330	2.3	10	400
		0.2	0.0	1000	1200	470	2.8	9	400
		0.2	0.8	1200	1300	650	2.6	6	360
C IV	3.13	1.0	0.0	860	740	350	2.0	8	370
		0.2	0.0	1000	1100	530	2.5	8	380
		0.2	0.8	1200	1200	700	2.3	5	340
Ly α	4.26	1.0	0.0	860	640	337	1.8	7	360
		0.2	0.0	1000	1100	540	2.3	7	370
		0.2	0.8	1200	1100	690	2.1	5	330

larger than those produced by changing the cosmological model. Of the alternative identifications of the emission line in the source spectrum, the choice of Lyα produces lens galaxy properties that are the closest to those associated with normal nearby spirals (Table 4.7). However, no sign of a Lyα forest is seen on the short-wavelength side of the emission line, even after subtracting the estimated contribution of the lens galaxy from the source spectrum. The absence of other emission lines in the spectrum (§4.5) and the lack of a Lyα forest argue against the identification of the emission line as Lyα. More sensitive spectroscopy of this system must be conducted to determine the source redshift unambiguously.

4.7.4 Prospects for Measuring H_0

A lens system can be used to estimate H_0 by comparing the time delays predicted by the lens model to the observed time delays. The time delays are a function of the lensing potential, the source and image positions, the redshifts of the source and lens, and the world model (through the angular diameter distances):

$$\Delta t_i = (1 + z_\ell)\frac{D_\ell D_s}{cD_{\ell s}}\left[\frac{1}{2}|\vec{x}_i - \beta|^2 - \psi(\vec{x}_i)\right],$$

where $\vec{x}_i = (x_i, y_i)$ is the angular position of the i^{th} lensed image and $\vec{\beta} = (x_s, y_s)$ is the position of the source. The observable quantity is the difference in the time delays, $\Delta t_{ij} \equiv \Delta t_i - \Delta t_j$. The predicted delays are proportional to h^{-1} through the ratio of angular diameter distances, so if it is possible to measure delays, the ratio of the predicted and observed delays will give h. For the model given in § 4.7.2, the components are expected to vary in the order: C, A, B, D. The predicted delays between components A, B and C are small: $\Delta t_{AC} = 6.5h^{-1}$ hr and $\Delta t_{BC} = 7.7h^{-1}$ hr. The delays between each of the three bright components and component D are all on the order of $142\,h^{-1}$ d. It will be challenging to measure the short time delays since radio loud quasars typically do not vary significantly on those time scales. However, with high-sensitivity observations, it will be quite possible to measure the long delays in this system, if the background source is variable.

4.8 Summary and Future Work

We have discovered a new four-image gravitational lens in the second phase of CLASS. The B2045+265 lens system is unusual in several respects. First, it is, with the possible exception of the puzzling 2016+112 system, the first known gravitational lens system in which both the background source and the lensing galaxy are radio sources. The radio emission from the lens, presumably from an active nucleus, can be used to locate the center of the lensing galaxy with high precision, which provides a strong constraint for lens models. Secondly, the flux density ratios of the three brightest lensed images are inconsistent with the predictions of simple models of lensing potentials. This result may indicate that there is significant structure in the mass distribution. Finally, the projected mass (and mass-to-light ratio) inside the Einstein ring of the lens is unusually high for a Sa galaxy. This may imply that there is a significant amount of dark matter associated with this galaxy, that the lens actually consists of a close pair of galaxies, or that the overall mass distribution of an associated group of galaxies is contributing to the lensing potential. Alternatively, the source redshift may be misidentified.

There are intriguing hints that the images of the background source may be resolved by high angular resolution observations. We have obtained high dynamic range VLBA observations which can be used to search for this possible extended mas-scale structure. If such structure is detected, the transformation matrices between the

lensed images of the background source provide strong constraints on the lensing model. These data may explain the unusual flux density ratios among the three bright images. The VLBA observations also will provide a more accurate position for the center of the lensing galaxy. In addition, more sensitive *Hubble Space Telescope* and spectroscopic observations can provide further details about the lensing galaxy and background source. The goal of these observations is to develop a well-constrained model of the lensing potential. A program of monitoring can be used to search for time delays in the system. Any measured delays can be combined with the lens models to yield a measurement of H_0.

We are indebted to the VLA analysts and operators, to Terry Stickel and Wayne Wack for heroic operation of the Keck Telescopes, and to the Keck Observatory and STScI staff. CDF thanks Erik Leitch for generously spending many hours in instruction in the use of the OVRO 40 m telescope and for writing the CMBPROG software. The operation of the 40 m telescope would be impossible without the dedication and knowledge of Russ Keeney and Mark Hodges. We are grateful to Gerry Neugebauer, Lee Armus and Aaron Evans for their expert assistance during the reduction of the NIRC and NICMOS data. We thank Lori Lubin, D. Wardell Hogg, Mike Pahre, Mark Metzger, and Chung-Pei Ma for useful discussions and comments on the manuscript. We thank the anonymous referee for helpful suggestions on how to improve the paper. This work is

supported by the NSF under grant #AST 9420018 and by the European Commission, TMR Program, Research Network Contract ERBFMRXCT96-0034 "CERES."

REFERENCES

Bertin, E. & Arnouts, S. 1996, A&A, 117, 393

Blandford, R. D. 1990, QJRAS, 31, 305

Blandford, R. D. & Narayan, R. 1992, ARA&A, 30, 311

Boyle, B. J. 1990, MNRAS, 243, 231

Carroll, S. M., Press, W. H., & Turner, E. L. 1992, ARA&A, 30, 499

Fassnacht, C. D., Womble D. S., Neugebauer, G., Browne, I. W. A., Readhead, A. C. S., Matthews, K., & Pearson, T. J. 1996, ApJ, 460, L103

Francis, P. J., Hewett, P. C., Foltz, C. B., Chaffee, F. H., Weymann, R. J., & Morris, S. L. 1991, ApJ, 373, 465

Fukugita, M., Futamase, T., & Kasai, M. 1990, MNRAS, 246, 24P

Fukugita, M. & Turner, E. L. 1991, MNRAS, 253, 99

Garrett, M. A., Porcas, R. W., Nair, S., & Patnaik, A. R. 1996, MNRAS, 279, L7

Gorenstein, M. V., Cohen, N. L., Shapiro, I. I., Rogers, A. E. E., Bonometti, R. J., Falco, E. E., Bartel, N., & Marcaide, J. M. 1988, ApJ, 334, 42

Hogg, D. W. & Blandford, R. D. 1994, MNRAS, 268, 889

Jackson, N. J., Nair, S., & Browne, I. W. A. 1997, in *Observational Cosmology with the New Radio Surveys*, eds., M. Bremer, N. Jackson & I. Perez-Fournon, (Dordrecht: Kluwer) 315

Keeton, C. R., Kochanek, C. S., & Falco, E. E. 1998, ApJ, submitted (astro-ph/9708161)

Kennicutt, R. C., Jr. 1992, ApJS, 79, 255

Kochanek, C. S. 1991, ApJ, 373, 354

Kovner, I. & Paczyński, B. 1988, ApJ, 335, L9

Kundić, T., Cohen, J. G., Blandford, R. D., & Lubin, L. M. 1997a, AJ, 114, 507

Kundić, T., Hogg, D. W., Blandford, R. D., Cohen, J. G., Lubin, L. M., & Larkin, J. E. 1997b, AJ, 114, 2276

Lawrence, C. R., Schneider, D. P., Schmidt, M., Bennett, C. L., Hewitt, J. N., Burke, B. F., Turner, E. L., & Gunn, J. E. 1984, Science, 223, 46

Leitch, E. M. 1998, Ph.D. thesis

Mao, S. 1992, ApJ, 389, 63

Mao, S. & Schneider, P. 1998, MNRAS, 295, 587

Matthews, K. & Soifer B. T. 1994 in *Infrared Astronomy with Arrays*, ed. I. McLean (Dordrecht: Kluwer), 239

Myers, S. T., et al. 1995, ApJ, 447, L5

Myers, S. T., et al. 1998, in preparation

Oke, J. B. 1990, AJ, 99, 1621

Oke, J. B. et al. 1995, PASP, 107, 375

Patnaik, A. R., Browne, I. W. A., Walsh, D., Chaffee, F. H., & Foltz, C. B. 1992, MNRAS, 259, 1P

Persson, S. E., Murphy, D. C., Krzeminski, W., Roth, M., & Rieke, M. 1998, AJ, submitted

Poggianti, B. M. 1997, A&AS, 122, 399

Postman, M., Lubin, L. M., & Oke, J. B. 1998, AJ, 116, 560

Press, W. H., Teukolsky, S. A., Vetterling, W. T., & Flannery, B. P. 1992, *Numerical Recipes in C* (New York: Cambridge University Press)

Refsdal, S. 1964, MNRAS, 128, 307

Rubin, V. C., Burstein, D., Ford, W. K., Jr., & Thonnard, N. 1985, ApJ, 289, 81

Schneider, P., Ehlers, J., & Falco, E. E. 1992, *Gravitational Lenses* (New York: Springer-Verlag)

Schneider, P. & Weiss, A. 1992, A&A, 260, 1

Shepherd, M. C., Pearson, T. J., & Taylor, G. B. 1994, BAAS, 26, 987

Stetson, P. 1987, PASP, 99, 191

Tonry, J. 1998, AJ, 115, 1

Turner, E. L. 1990, ApJ, 242, L135

Turner, E. L., Ostriker, J. P., & Gott, J. R. 1984, ApJ, 284, 1

Vogt, N. P., Forbes, D. A., Phillips, A. C., Gronwall, C., Faber, S. M., Illingworth, G. D., & Koo, D. C. 1996, ApJ, 465, L15

Chapter 5

A Determination of H_0 with the Gravitational Lens 1608+656[†]

C. D. Fassnacht, T. J. Pearson, A. C. S. Readhead

Owens Valley Radio Observatory, California Institute of Technology, 105-24, Pasadena, CA 91125

I. W. A. Browne

NRAL Jodrell Bank, University of Manchester, Macclesfield, Cheshire SK11 9DL, UK

L. V. E. Koopmans

Kapteyn Astronomical Institute, Postbus 800, 9700 AV Groningen, The Netherlands

S. T. Myers

Department of Physics and Astronomy, University of Pennsylvania, 209 S. 33rd St., Philadelphia,

PA 19104-6396

P. N. Wilkinson

[†] This chapter is being prepared for submission to the *Astrophysical Journal.*

NRAL Jodrell Bank, University of Manchester, Macclesfield, Cheshire SK11 9DL, UK

Abstract

We present the results of a program to monitor the gravitational lens B1608+656 with the VLA. The system was observed over a seven month period from 1996 October to 1997 May. The 64 epochs of observation have an average spacing of 3.6 d. The light curves of the four images of the background source show that the flux density of the background source has varied at the 3 – 5% level. We measure time delays in the system based on common features that are seen in all four light curves. The three independent time delays in the system are found to be $\Delta t_{BA} = 30^{+5}_{-7}$ d, $\Delta t_{BC} = 36^{+5}_{-8}$ d, and $\Delta t_{BD} = 76^{+6}_{-7}$ d at 95% confidence. The uncertainties on the time delays are determined by Monte Carlo simulations which use fake light curves that have the characteristics of the observed light curves. This is the first gravitational lens system for which three independent time delays have been measured. A companion paper (Koopmans & Fassnacht 1998) presents a mass model for the lensing galaxy. The model correctly reproduces the image positions, flux density ratios, and the ratios of the time delays. The last condition is crucial for determining H_0 with a four-image lens. We combine the time delays with the model to obtain a value for the Hubble Constant

of $H_0 = 59^{+4}_{-5}$ km sec^{-1} Mpc^{-1} (statistical). In addition there is an estimated systematic uncertainty of ± 15 km sec^{-1} Mpc^{-1} from uncertainties in modeling the radial mass profile of the lensing galaxy. The value of H_0 presented in this paper is comparable to recent measurements of H_0 from the gravitational lenses 0957+561 (e.g., Kundić et al. 1997), PG 1115+080 (Schechter et al. 1997; Impey et al. 1998), 0218+357 (Biggs et al. 1998), and PKS 1830−211 (Lovell et al. 1998).

5.1 Introduction

Even before the discovery of the first gravitational lens system, a technique for using gravitational lenses to measure the distance scale of the universe had been developed (Refsdal 1964). The technique requires a lens system in which multiple images of the background source are formed. A "map" of the geodesics along which the light travels to form the images is constructed and used to predict the differences in light travel times along the geodesics. If the background source is variable, these time delays can be measured as each image varies in turn. The ratios between the observed and predicted delays give the Hubble Constant in the assumed world model $(\Omega_M, \Omega_\Lambda)$. The use of gravitational lenses for determining H_0 has major advantages over traditional "distance ladder" approaches. First, the technique gives a direct estimate of H_0 at cosmological distances, where the effects of peculiar velocities are minimal. Second,

this measurement of H_0 is obtained in one step, without the propagation of errors inherent in the distance ladder approach.

With the discovery that the "double quasar" 0957+561 A,B was a lens system (Walsh et al. 1979), the effort to use lenses to measure H_0 began in earnest. For many years the effort was hindered by both the paucity of known lens systems and the difficulty in measuring time delays in the systems. In fact, an unambiguous time delay has only recently been measured in 0957+561 in spite of over ten years of intensive monitoring (Kundić et al. 1995; Kundić et al. 1997; Oscoz et al. 1997; Haarsma et al. 1998). Another of the earliest known lenses, PG 1115+080 (Weymann et al. 1980), has also just produced measurable time delays (Schechter et al. 1997). However, we may have entered a new era for time delay measurements from gravitational lenses. One reason for this is the accelerated rate of discovery of new lenses from systematic radio surveys. The Jodrell-VLA Astrometric Survey (JVAS; Patnaik et al. 1992; Browne et al. 1997b; Wilkinson et al. 1998) has produced 6 new lenses, and time delays have been measured for one of them (0218+357; Biggs et al. 1998). The ongoing Cosmic Lens All-Sky Survey (CLASS; Myers et al. 1998) has found 12 new lenses since it began in 1994. This paper reports the first measurement of time delays from a CLASS lens.

The CLASS project is a large search for gravitational lenses with the VLA[1], with

[1]The National Radio Astronomy Observatory is operated by Associated Universities, Inc., under cooperative agreement with the National Science Foundation.

an explicit goal of finding lens systems which can be used to measure H_0. The gravitational lens B1608+656 (RA: 16 09 13.956, Dec: +65 32 28.971, J2000) was observed in the first phase of CLASS and was immediately recognized as a lens system. The radio discovery image shows four unresolved components in a typical lens geometry (Myers et al. 1995; see Fig. 5.1 for a map of the system). The system was also discovered in a search for gigahertz-peaked spectrum sources and was found to be the lensed core of a classical radio double source (Snellen et al. 1995). Further investigations of the system have provided data crucial for using the system for measuring H_0. We have measured the lens redshift ($z_\ell = 0.630$; Myers et al. 1995) and source redshift ($z_s = 1.39$; Fassnacht et al. 1996). Optical and infrared observations taken with the *Hubble Space Telescope* reveal that the background source is being lensed by a pair of possibly merging galaxies (Jackson et al. 1997; Fassnacht et al. 1998b). The positions of the lensing galaxies relative to the lensed images are important constraints on models of the lensing potential (Koopmans & Fassnacht 1998; hereafter Paper 2). The HST images also show arcs due to the lensing of stellar emission from the background source. These arcs could be used as further constraints of the lens model.

Flat-spectrum cores of radio galaxies such as the lensed object in 1608+656 are often variable. To test for variability in the 1608+656 background source, we made several observations of the system with the VLA, separated by timescales of months.

These data showed that the flux density of the background source varied by up to 15%. The variability makes 1608+656 an excellent candidate for a dedicated monitoring program to determine time delays. This paper presents the results of VLA monitoring from October 1996 to May 1997. These observations have resulted in the measurement of the three independent time delays in the 1608+656 system and a subsequent determination of H_0. The Hubble Constant is expressed as $H_0 = 100\,h$ km/sec/Mpc. Throughout this paper we assume $(\Omega_M, \Omega_\Lambda) = (1, 0)$. The effect of varying the cosmological model is treated in Paper 2 (see also Chapter 1 of this thesis).

5.2 Observations

We observed 1608+656 between 1996 October 10 and 1997 May 09, during which time the VLA was in the A, BnA, and B configurations. The 64 epochs were separated, on average, by 3.6 d. The observations were carried out at 8.46 GHz, giving angular resolutions ranging from 0.″25 to 0.″7 in the different array configurations. The observations are summarized in Table 5.1. The typical epoch is 60 min long and includes scans on 1608+656, a flux calibrator (3C 286 or 3C 48), a phase calibrator (1642+689) chosen from the VLA calibrator list (Perley & Taylor 1997), and two secondary flux calibrators (1634+627 and 1633+741). The secondary flux calibrators are nearby steep-spectrum sources that are not expected to vary over the timescales of the observations. We observe these sources to determine corrections for errors in

the absolute flux calibration from epoch to epoch. The basic observing pattern is:

- 1642+689 (1 min on source)
- 1634+627 (1 min on source)
- 1608+656 (4–6 min on source)
- 1633+741 (2 min on source)

A typical 60 min observation begins with a 9 – 10 min scan (including slew time) on the flux calibrator, contains three repetitions of the basic pattern on 1608+656, and ends with scans on 1642+689 (1 min) and the flux calibrator again (~3 min). For the few observations that are 30 min or 90 min in length, the number of repetitions of the basic pattern is altered.

5.3 Data Reduction

5.3.1 Calibration

The data reduction is separated into two major steps, calibration and mapping. The data for each epoch are calibrated using standard routines in AIPS. Before calibration, the data quality for all sources is assessed and bad points are flagged with the EDITA and TVFLG tasks. Both of the flux calibrators are heavily resolved by the VLA in A configuration at 8.5 GHz. Hence, we cannot treat the calibrators as point sources

Table 5.1 OBSERVATIONS

Epoch	MJD−50000	Array Configuration	LST	t_{tot} (min)	t_{1608} (min)	Comments
1996 Oct 10	366	D→A	17:00	60	27	
1996 Oct 12	368	D→A	15:45	30	5	
1996 Oct 16	372	D→A	21:30	60	21	
1996 Oct 18	374	A	18:00	60	21	
1996 Oct 20	376	A	02:00	60	21	Elev. $\leq 30°$. Thunderstorms
1996 Oct 23	379	A	17:45	30	6	
1996 Oct 26	382	A	15:00	60	18	$T_{sys} > 100$K .
1996 Oct 29	385	A	22:45	30	5	Elev. $\leq 30°$. Gusting winds
1996 Oct 31	387	A	20:30	60	18	
1996 Nov 01	388	A	19:00	60	18	
1996 Nov 03	390	A	18:30	60	21	Wind ≥ 10 m/s
1996 Nov 07	394	A	07:15	30	6	Elev. $\leq 30°$
1996 Nov 08	395	A	13:30	60	21	
1996 Nov 11	398	A	13:30	60	18	
1996 Nov 12	399	A	07:45	30	8	Elev. $\leq 30°$
1996 Nov 15	402	A	17:30	60	21	High wind gusts
1996 Nov 18	405	A	16:00	60	21	
1996 Nov 23	410	A	17:30	60	20	Wind ≥ 10 m/s
1996 Nov 27	414	A	21:30	60	20	
1996 Dec 01	418	A	14:30	60	20	
1996 Dec 05	422	A	14:45	30	7	
1996 Dec 07	424	A	15:15	30	5	
1996 Dec 10	427	A	17:30	60	20	Wind ≥ 10 m/s
1996 Dec 15	432	A	17:45	90	34	
1996 Dec 20	437	A	19:25	30	5	
1996 Dec 23	440	A	18:15	90	34	
1996 Dec 24	441	A	15:45	30	10	
1996 Dec 29	446	A	15:30	60	20	
1997 Jan 03	451	A	17:00	60	20	Wind ≥ 10 m/s
1997 Jan 07	455	A	19:15	90	35	
1997 Jan 11	459	A	16:30	60	20	
1997 Jan 16	464	A→BnA	16:30	60	20	
1997 Jan 17	465	A→BnA	09:45	30	8	Elev. $\leq 30°$. Flurries
1997 Jan 20	468	A→BnA	16:00	60	20	
1997 Jan 26	474	BnA	14:30	60	20	Rain
1997 Jan 30	478	BnA	13:30	60	19	
1997 Feb 02	481	BnA	20:30	60	20	
1997 Feb 08	487	BnA	19:30	60	19	
1997 Feb 13	492	BnA→B	16:00	60	18	
1997 Feb 18	497	B	18:30	60	19	
1997 Feb 23	502	B	18:30	60	19	
1997 Feb 28	507	B	18:30	60	19	Snow storms
1997 Mar 03	510	B	18:30	60	19	
1997 Mar 08	515	B	16:30	60	18	
1997 Mar 14	521	B	18:53	75	30	
1997 Mar 16	523	B	18:23	45	12	
1997 Mar 21	528	B	18:30	60	20	
1997 Mar 25	532	B	22:00	60	19	Wind ≥ 10 m/s. Snowing
1997 Mar 30	537	B	19:45	90	30	
1997 Apr 01	539	B	18:00	60	20	
1997 Apr 05	543	B	18:30	60	20	
1997 Apr 07	545	B	18:30	60	20	
1997 Apr 11	549	B	18:30	60	20	

Table 5.1 (continued) OBSERVATIONS

Epoch	MJD−50000	Array Configuration	LST	t_{tot} (min)	t_{1608} (min)	Comments
1997 Apr 15	553	B	18:30	60	20	
1997 Apr 19	557	B	15:30	60	18	
1997 Apr 22	560	B	18:30	60	20	
1997 Apr 26	564	B	18:30	60	20	
1997 May 03	571	B	18:30	60	20	
1997 May 08	576	B	18:45	90	30	
1997 May 13	581	B	18:30	60	20	
1997 May 17	585	B	17:00	60	19	
1997 May 21	589	B	18:30	60	20	
1997 May 23	591	B	18:30	60	20	
1997 May 26	594	B	20:30	60	19	

without limiting the number of baselines that can be used to calculate phase and gain solutions. In order to increase the number of baselines available for the calculations, we create models of 3C 286 and 3C 48 that incorporate the extended emission from the sources. We combine observations from several epochs with the DBCON task in AIPS. The resulting data sets have excellent (u, v)-plane coverage, from which we can make high dynamic-range maps. The mapping, which is performed in the DIFMAP package (Shepherd 1997), consists of alternating iterations of CLEANing (Högbom 1974) and self-calibration. The final lists of CLEAN components are read back into AIPS and serve as the calibrator models.

The procedures for the phase calibrator are simpler because the emission from 1642+689 is dominated by an unresolved component. Thus, the assumption that 1642+689 is a point source leads to adequate phase and gain solutions. These calibration solutions are applied to the 1608+656, 1633+741, and 1634+627 data.

5.3.2 Source Maps

We map the data and determine flux densities using the DIFMAP package. We do not expect to see any structural changes over the course of the observations; only changes in flux densities should be observed. To treat the data from each epoch in a uniform fashion and to shorten the mapping procedure, we create models of the observed source structures from high dynamic-range maps. For epochs with noisy data, these models are needed to fix the locations of the regions of low surface brightness emission, which otherwise would not be well-constrained by the data.

To make the high dynamic-range maps of each source, we combine 13 high-quality data sets from A and B configuration observations with the DBCON task. The combined data sets, which have excellent (u, v) coverage, are then mapped in DIFMAP. The secondary flux calibrators, which have significant emission from extended structures, are mapped by using an iterative cycle of CLEANing and self-calibration. Both phase and amplitude self-calibration are used. The models for these sources consist of the final lists of CLEAN components. The emission from 1608+656 is dominated by the four unresolved images of the background source (Fig. 5.1). Hence, instead of CLEANing the data, we assign point-source model components to the four images of the background source. We then use the DIFMAP `modelfit` function, which varies the component positions and flux densities to obtain the best fit to the (u, v)-plane visibilities. The model fitting iterations are alternated with phase and amplitude

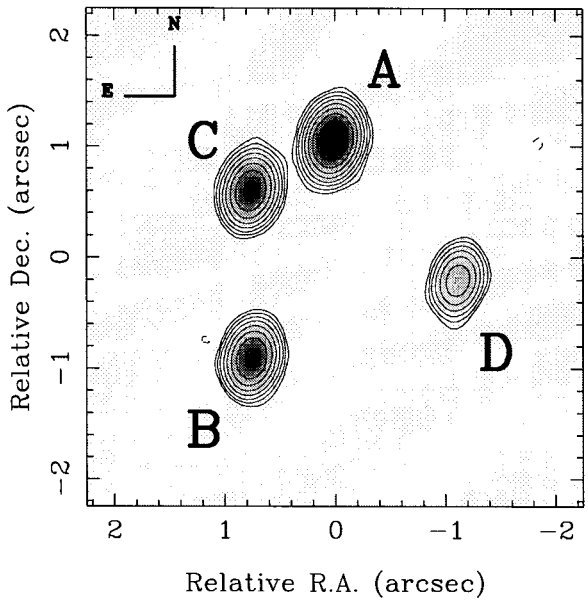

Figure 5.1 Map of 1608+656 from observation on 1996 November 18. The contours are (−3, 3, 6, 12, 24, 48, 96, 192, 384, 768) times the RMS noise level of 0.035 mJy/beam. The map is made by fitting point source components to the (u, v) data and restoring with a $0''.33 \times 0''.23$ restoring beam.

self-calibration. In later rounds of the model fitting, several nearby weak sources are seen in the residual maps. These sources are included in the model for the last few iterations of the model fitting.

The first step in the mapping procedure at each epoch is to read in the data and perform a phase-only self-calibration against the model of the source. This procedure aligns the phase center of the observation with that of the model and eliminates the need for many early steps of cleaning and self-calibration. After this point, the procedures used for 1608+656 differ from those used for the secondary flux calibrators.

5.3.3 1608+656

We determine the flux densities of the four lensed images in the 1608+656 system at each epoch as follows. After the initial phase self-calibration step at each epoch, the model described in the previous section is varied to find the best fit to the (u, v)-plane visibilities for that epoch. The component positions are held fixed and only the flux densities are allowed to vary. After several iterations of model fitting, another phase self-calibration is performed against the new model and more iterations of the model fitting are performed. At this point, the component flux densities and the RMS noise in the residual map are recorded in a log file (the "phasecal" data set). We then perform an overall gain calibration on the data, getting one gain correction per antenna for the observation. Typical gain corrections are 1 – 2%. Another round of model fitting is performed and the final component flux densities and RMS noise in the residual map are recorded in the log file (the "gscale" data set). We record the two separate data sets in case the gain calibration introduces any errors which may bias the subsequent analysis. All subsequent analysis is performed on both data sets and no significant differences are seen in the results.

5.3.4 Secondary Flux Calibrators

The steep-spectrum secondary flux-density calibrators contain significant extended emission and should not vary over the course of the observations. We expect that any

observed variations in flux density are due to errors in the absolute flux calibration, and as such can be expressed as an overall scaling of the model CLEAN component flux densities. That is, the CLEAN component flux densities should not vary with respect to each other. The task of finding the overall flux density of these sources is thus simplified into finding the scale factor that, when multiplied by the component flux densities, gives the best fit to the data. To find the best-fit scaling for each data set, we create 11 CLEAN component models of the sources, based on the models described in §5.3.2. We scale the flux densities of the model components by factors of 0.9 to 1.1, in steps of 0.02. Each of the scaled models is compared to the (u, v)-plane visibilities and a reduced χ^2 goodness-of-fit value is returned. We then fit a parabola to the points in the reduced χ^2 curve and find the scale which corresponds to the minimum reduced χ^2. This scaling gives the total flux density of the source at that epoch.

5.3.5 Light Curve Editing

Moore & Hewitt (1997), in their analysis of the 15 GHz light curves of the gravitational lens 0414+0534, developed objective criteria to flag questionable data. They deleted from their light curves all points associated with observations with the following conditions: the telescope elevations were less than 30°, the wind speed was greater than 10 m/s, or there was precipitation. We have noted all epochs satisfying their

criteria in the "Comments" column of Table 5.1. However, we are able to include many of these points in our analysis because observations at 8.5 GHz are less sensitive to the observing conditions than are observations taken at 15 GHz. As such, we have only excluded epochs for which the data are severely affected by the observing conditions. This assessment is made by examining the light curves of the secondary calibrator sources. All epochs for which the flux densities of the calibrators deviate by more than 15% from the mean value are deleted. Only two epochs are deleted after the application of this criterion: 376 and 382 (MJD−50000). Note that epoch 376 satisfies two of the flagging criteria defined by Moore & Hewitt. At epoch 382, the system temperatures for all of the telescopes were in the range 100 – 200 K, as compared to the 30 – 50 K system temperatures measured for all other epochs. These high system temperatures may have resulted from the fact the subreflectors of several of the antennas had frozen prior to the observation and had just thawed. The signal-to-noise ratio of the maps for epoch 382 were so low that no useful information could be extracted from them. The final edited light curves contain 62 epochs, with an average spacing of 3.7 d. Edited versions of the secondary flux calibrator and 1608+656 light curves are shown in Figures 5.2 and 5.3.

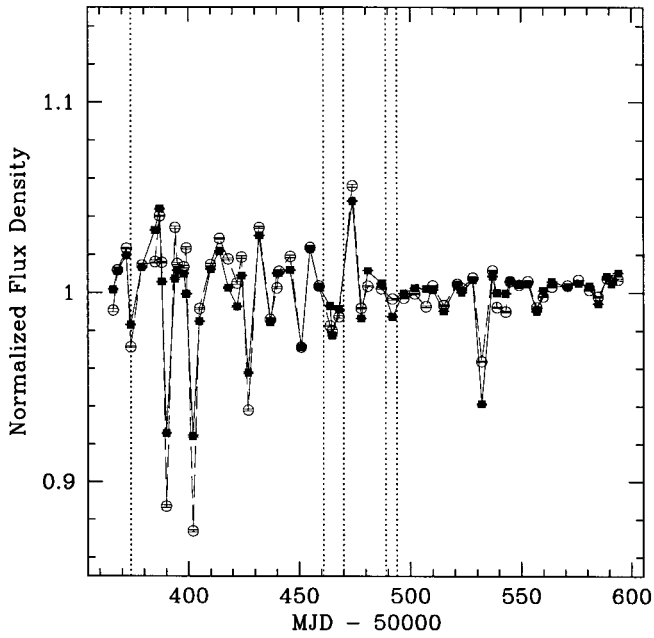

Figure 5.2 Light curves of the secondary calibrators 1633+741 (open circles) and 1634+627 (filled boxes). Each curve has been divided by its mean value over the length of the observations. The assumption that the variations seen in the flux densities of these sources arise from errors in the absolute flux calibration of the data is supported by the fact that the curves follow each other so closely. The dotted vertical lines represent changes of array configuration. See Table 5.1 for the array configuration at each epoch.

5.3.6 "Flat-fielding" and Final Light Curves

The normalized light curves of the secondary flux calibrators (Fig. 5.2) show variations of up to 10% of the mean value. The light curves of the two sources track each other extremely well, suggesting that these variations are due to errors in the absolute flux calibration of the data rather than any intrinsic variability of the sources. Because of this, we can use the light curves of the secondary flux calibrators to remove residual

flux calibration errors in the 1608+656 component light curves. We create a "flat-field" curve by normalizing the light curves of the secondary flux calibrators and then averaging the two normalized fluxes at each epoch. We then divide the 1608+656 component light curves by the "flat-field" curve. The "flat-field" correction is effective in reducing the scatter in the 1608+656 light curves, as can be seen by comparing Fig. 5.3 to Fig. 5.4.

The errors on the final flux densities which are plotted in Fig. 5.4 are a combination of additive and multiplicative terms. The additive uncertainty is well-approximated by the RMS noise in the residual map at the end of the model-fitting. The multiplicative term is indicative of how well the model-fitting procedure is able to find the "true" total flux density of a source. We estimate this error by calculating the ratio of the flux densities of 1634+627 and 1633+741, which we expect not to vary with respect to each other. The flux density ratio is not affected by errors in the absolute flux calibration, so any scatter in the ratio can be attributed to errors in the model fitting procedure. We find the fractional RMS scatter in the flux density ratio to be 1.9%; the product of the component flux densities and this value gives the multiplicative uncertainty. The final errors on the flux densities are a combination in quadrature of the additive and multiplicative terms. For the three brightest components (A, B, and C), the multiplicative terms dominate; for component D the multiplicative and additive terms are comparable.

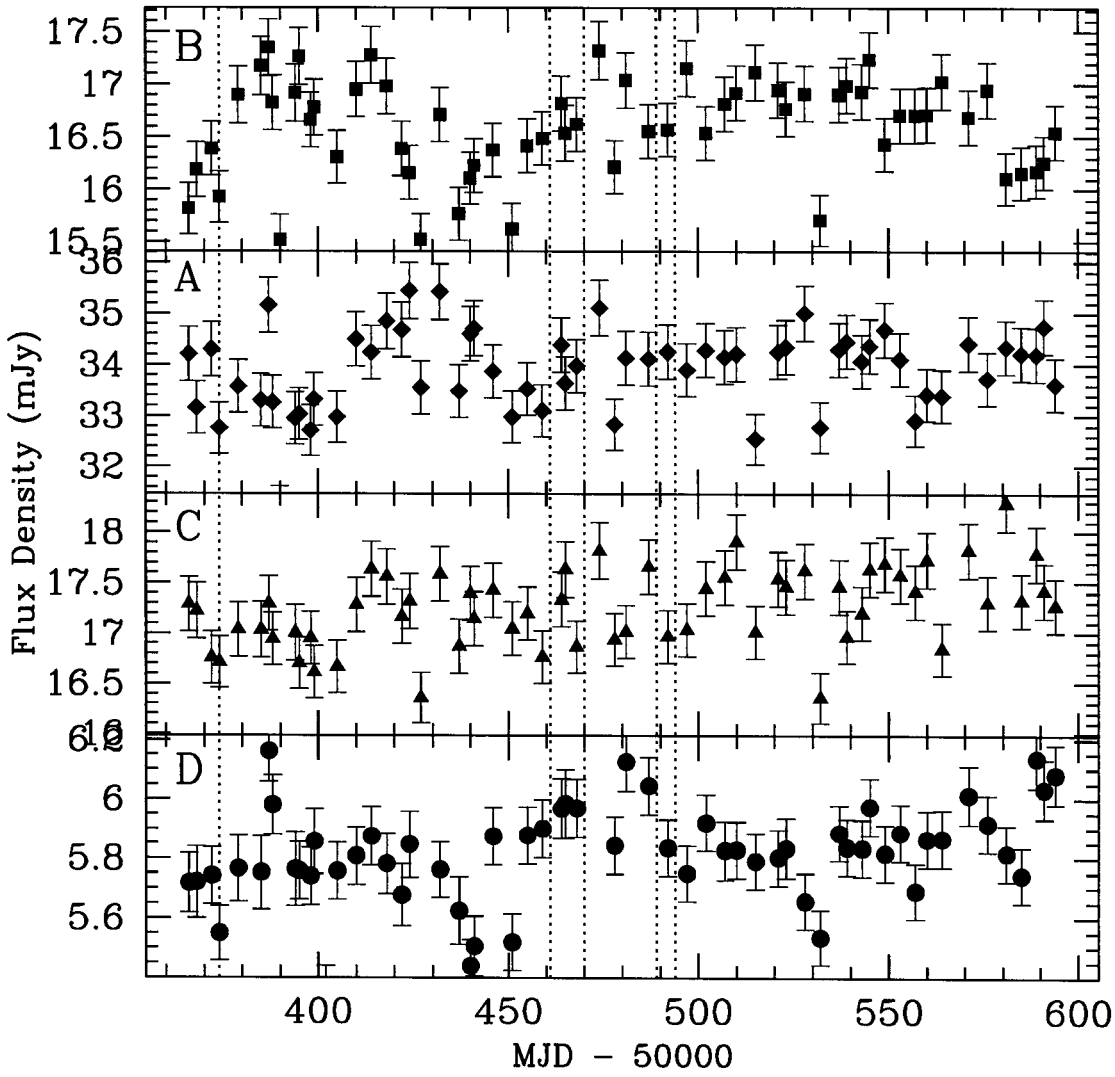

Figure 5.3 Light curves for the four images of the background source in 1608+656 *before* the "flat-field" correction has been made. The light curves are presented in the order (from top to bottom) in which the model predicts that they will vary (B, A, C, D). The limits on the vertical axes for each case are chosen to be the mean value ±7%, so that equal fractional variations in the flux densities of the components will have the same heights in the curves.

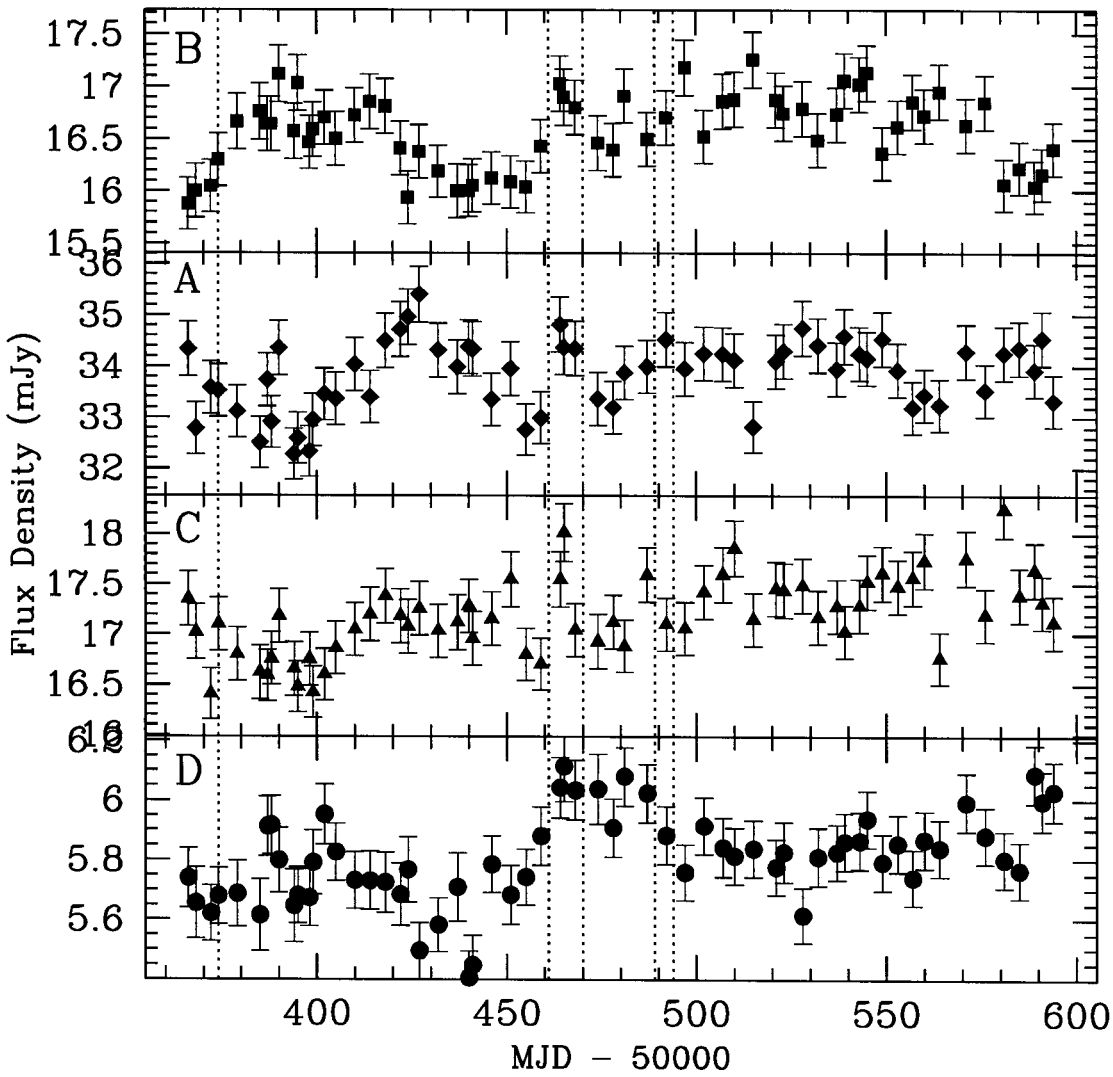

Figure 5.4 Same as Fig. 5.3 but *after* the application of the "flat-field" correction.

The flux density of a lensed image of the background source is $\mu_i S$, where S is the true flux density of the background source and μ_i is the magnification associated with the i^{th} (unresolved) image. Similarly, if the flux density of the background source changes by an amount dS, the lensed images will vary by $\mu_i\, dS$. Hence, any variations in the 1608+656 component light curves that are due to variations in the background source must have the same *fractional* amplitudes in all four curves. For this reason, the component light curves presented in Figs. 5.3 and 5.4 are scaled such that the vertical axis covers the same fractional scale. All four light curves show variations in flux density at the 3 – 5% level, and there are common features that can be seen in each. Each light curve shows a rise of ∼5% in flux density, followed by a plateau lasting ∼20 d and then a drop of ∼4%. Although these variations are not large compared to those seen in other lens systems (e.g., Kundić et al. 1995, 1997; Schechter et al. 1997; Biggs et al. 1998; Lovell et al. 1998), it is still possible to measure the time delays in this system, as discussed in §5.4.

5.4 Determination of Time Delays

Models of the 1608+656 system predict that, if the background source is variable, the lensed images will vary in the order B → A → C → D (Myers et al. 1995; Paper 2). This is, in fact, the behavior seen in the 1608+656 light curves. In order to determine time delays between component B and the other three components, we have used

two statistical methods: 1) smoothing and χ^2 minimization, and 2) smoothing and cross-correlation. The methods are discussed below. All of the analysis has been performed on both the "phasecal" and "gscale" data sets (§5.3.3). No significant differences in the results are seen, so we present only the results from the "gscale" set in the subsequent discussion.

5.4.1 Smoothing

The two methods of determining the time delays from the 1608+656 light curves require that the observed data be transferred onto a regular grid. Some previous determinations of time delays (e.g., Kundić et al. 1997; Biggs et al. 1998) have accomplished this transfer by linear interpolation of the data. However, the flux density variations seen in the 1608+656 images are small compared to the noise in the curves; therefore, linear interpolation can amplify noise spikes. In contrast, smoothing reduces the effects of noise compared to the true variations if these have typical timescales significantly longer than the sampling interval. We smooth and re-sample the data by calculating the weighted mean of points within a smoothing window that is moved from the beginning to the end of the observations in regular steps. The step size is set to one day.

We smooth each light curve with several different functions to avoid biasing the results by our choice of weighting function or window size. For completeness, we also

include the results obtained from interpolating the data by piecewise linear interpolation. We use the following smoothing schemes: (1) boxcar-weighted mean, (2) triangle-weighted mean, (3) Gaussian-weighted mean, (4) boxcar-weighted mean with a variable-width smoothing window, and (5) triangle-weighted mean with a variable-width window. In the last two schemes, the width of the smoothing window is varied such that the same number of points are always included in the window. We use 3, 5, and 7 point windows for these methods. For the fixed-width window schemes, we smooth with window widths of 5, 10, and 15 d. The Gaussian weighting scheme uses values of σ equal to 3, 5, and 7 d. In addition to the weighting from the smoothing function, the data points are also variance-weighted. Thus, the overall weighting on any point t_i which is being used to calculate a weighted mean at t_0 is:

$$w_i = \frac{\frac{1}{\sigma_i^2}\, g(t_i - t_0)}{\sum_j [\frac{1}{\sigma_j^2}\, g(t_j - t_0)]}, \tag{5.1}$$

where $g(t)$ is the smoothing function (e.g., g(t) = 1 for boxcar smoothing) and σ_i is the uncertainty on the flux density at t_i, calculated in §5.3.6. The variance of the weighted mean y at the j^{th} step in the smoothed curve then becomes

$$\sigma_{y,j}^2 = \frac{1}{\left(\sum [\frac{1}{\sigma_i^2}\, g(t_i - t_0)]\right)^2} \sum \frac{[g(t_i - t_0)]^2}{\sigma_i^2}. \tag{5.2}$$

Thus, $\sigma_{y,j}$ is used for the uncertainty in the smoothed flux density at that step.

5.4.2 χ^2 Minimization

For the χ^2 minimization technique, we compare two light curves, one of which is designated the "control" curve and the other of which is designated the "comparison" curve. Both curves are smoothed, and then the comparison curve is scaled so that its mean flux density matches that of the control curve. After this scaling, the comparison curve is shifted in time with respect to the control curve. The step size used is 1 d. The minimum and maximum shifts are set to $\pm$114 d, i.e., half of the total length of the observations. The minimum and maximum scalings are set to $\pm$20% of the ratio of the mean flux densities of the curves with a step size of 2%. Note that the number of degrees of freedom for each χ^2 computation is approximately inversely proportional to the number of overlapping points between the shifted and unshifted curves. Thus, the reduced χ^2 correctly compensates for the smaller number of overlapping points as the shifts become large. We repeat the χ^2 minimization three times, once for each independent pair of light curves. The component B light curve is always taken as the control curve. In the three repetitions of the χ^2 minimization, the comparison curves are A, C, and D, respectively. Table 5.2 summarizes the results. Typical goodness-of-fit curves for the three pairs of light curves are shown in Figures 5.5 – 5.7.

Table 5.2 TIME DELAYS FROM χ^2 MINIMIZATION AND CROSS-CORRELATION

Smoothing Function	Smoothing "Width"[a]	χ^2 Minimization			Cross-correlation		
		Δt_{BA}	Δt_{BC}	Δt_{BD}	Δt_{BA}	Δt_{BC}	Δt_{BD}
Boxcar	5	29.07	35.98	74.08	28.00	36.00	74.00
	10	28.89	36.83	75.27	29.00	37.00	75.00
	15	32.14	34.09	75.48	32.00	36.00	75.00
Triangle	5	30.89	36.25	74.07	28.00	36.00	74.00
	10	28.93	35.69	75.19	29.00	35.00	75.00
	15	30.96	33.99	75.84	30.00	36.00	76.00
Gaussian	3	30.59	36.14	75.71	30.00	36.00	76.00
	5	31.56	36.66	76.43	31.00	37.00	77.00
	7	31.52	37.13	76.99	31.00	38.00	77.00
Variable-width	3	30.24	35.75	75.47	30.00	36.00	75.00
boxcar	5	30.15	36.38	77.08	30.00	37.00	78.00
	7	30.01	36.89	76.94	30.00	39.00	77.00
Variable-width	3	30.38	35.81	75.88	30.00	36.00	76.00
triangle	5	30.57	36.50	76.69	30.00	37.00	77.00
	7	30.31	36.54	76.88	30.00	37.00	77.00
Linear Interpolation		30.30	31.80	75.49	28.00	32.00	75.00
Median		30.3	36.2	75.8	30	36	76

[a] "Width" is width of window for boxcar and triangle smoothings, σ for Gaussian smoothing, and number of points in window for variable-width smoothings.

Table 5.3 FLUX DENSITY RATIOS FROM χ^2 MINIMIZATION

Smoothing Function	Smoothing "Width"	S_A/S_B	S_C/S_B	S_D/S_B
Boxcar	5	2.0408	1.0368	0.3502
	10	2.0425	1.0379	0.3504
	15	2.0432	1.0379	0.3504
Triangle	5	2.0407	1.0368	0.3502
	10	2.0421	1.0376	0.3504
	15	2.0429	1.0379	0.3504
Gaussian	3	2.0428	1.0379	0.3504
	5	2.0432	1.0380	0.3504
	7	2.0431	1.0379	0.3504
Variable-width	3	2.0426	1.0383	0.3504
boxcar	5	2.0435	1.0384	0.3505
	7	2.0433	1.0382	0.3505
Variable-width	3	2.0427	1.0383	0.3504
triangle	5	2.0435	1.0384	0.3505
	7	2.0434	1.0382	0.3505
Linear Interpolation		2.0401	1.0355	0.3507
Median		2.0429	1.0379	0.3504

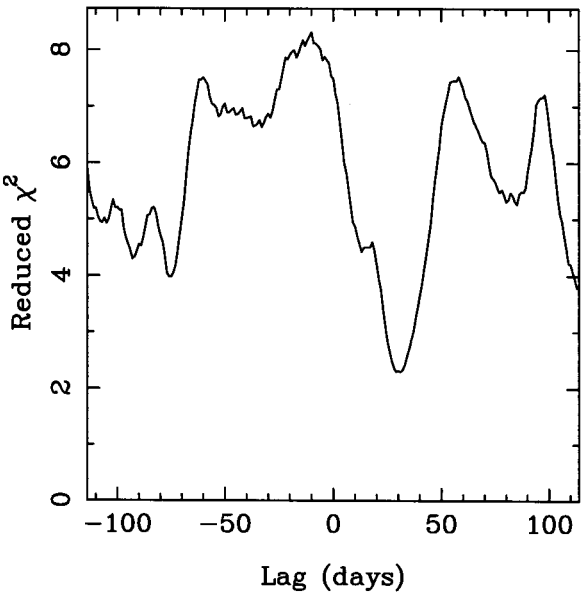

Figure 5.5 Plot of reduced χ^2 vs. lag from comparison of the light curves of components B and A, each smoothed with a boxcar of width 10 d. The minimum is at a lag of 28.9 d.

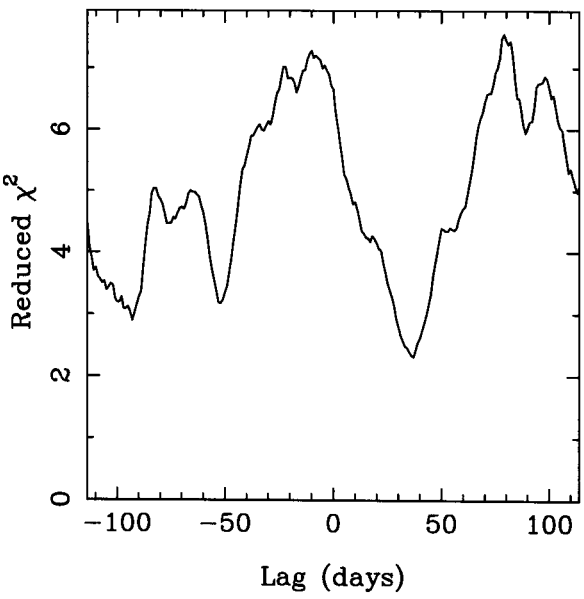

Figure 5.6 Same as Fig. 5.5 but for light curves of components B and C. The minimum is at a lag of 36.8 d.

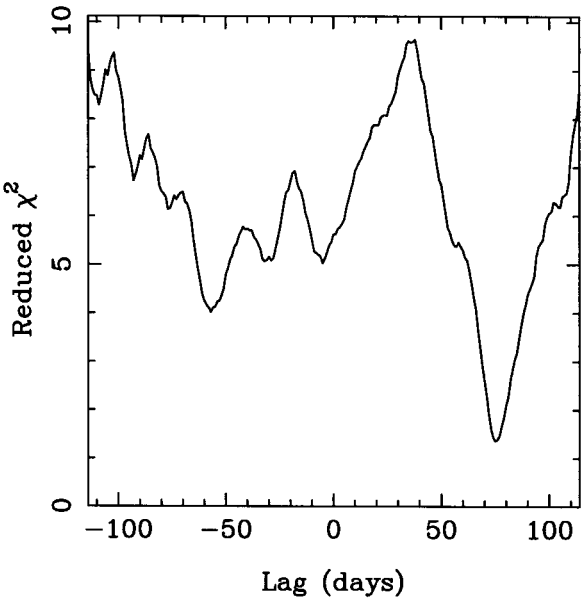

Figure 5.7 Same as Fig. 5. ; but for light curves of components B and D. The minimum is at a lag of 75.3 d.

5.4.3 Cross-corr elation

For the cross-correlatio calculations the component B light curve is once again taken as the control curve. Be ore the cross-correlations are performed, both the comparison and control curves are smoothed and then divided by their mean values over the observations. The norm alization by the mean value puts the fractional variations in the light curves at the same level. The cross-correlation functions are computed in the time domain, with the value at each lag calculated in the standard fashion:

$$r_{jk} \equiv \frac{s_{jk}^2}{s_j s_k} \tag{5.3}$$

where s_{jk} is the covariance defined by

$$s_{jk}^2 = \frac{\frac{1}{N-1}\sum_i \left[\frac{1}{\sigma_{ij}^2+\sigma_{ik}^2}(x_{ij}-\bar{x_j})(x_{ik}-\bar{x_k})\right]}{\frac{1}{N}\sum_i \frac{1}{\sigma_{ij}^2+\sigma_{ik}^2}} \tag{5.4}$$

and N is the number of overlapping points (e.g., Bevington 1969). Note that in x_{ij} or σ_{ij}, the first subscript refers to a particular observation, and the second subscript refers to the name of the variable under discussion. Thus x_{ij} is the i^{th} observation of variable x_j. The variance, s_j^2, is given by

$$s_j^2 = \frac{\frac{1}{N-1}\sum_i \left[\frac{1}{\sigma_i^2}(x_{ij}-\bar{x_j})^2\right]}{\frac{1}{N}\sum_i \frac{1}{\sigma_i^2}} \tag{5.5}$$

where the means are weighted means —

$$\bar{x_j} = \frac{\sum_i \left[\frac{1}{\sigma_i^2}x_{ij}\right]}{\sum_i \frac{1}{\sigma_i^2}}. \tag{5.6}$$

The cross-correlation calculations are repeated for all of the smoothing functions described in §5.4.1. In all cases, clear peaks in the cross-correlation curves are seen. Typical curves are shown in Figs. 5.8 – 5.10. The lags at which the peak correlation coefficients occur are given in Table 5.2. The average displacement between the cross-correlation and χ^2 minimization lags for each pair of curves is less than one day.

5.4.4 Time Delays

There is some scatter in the results presented in Table 5.2, which is not surprising considering the low levels of variation and sparse sampling of the light curves. However,

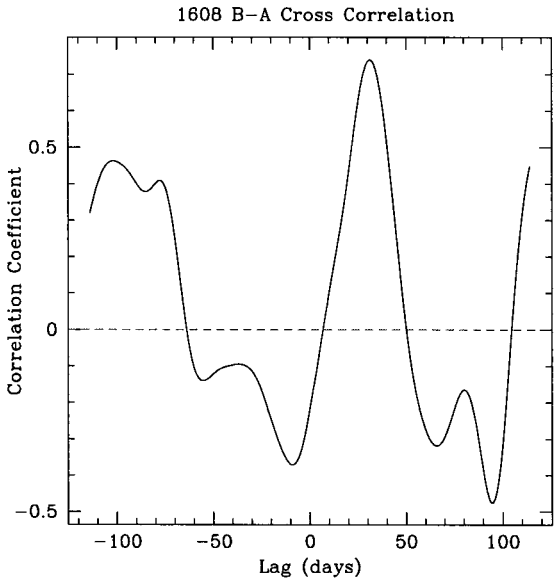

Figure 5.8 Plot of correlation coefficient vs. lag from comparison of the light curves of components B and A, each smoothed with a Gaussian with $\sigma = 5$d. The maximum is at a lag of 31 d.

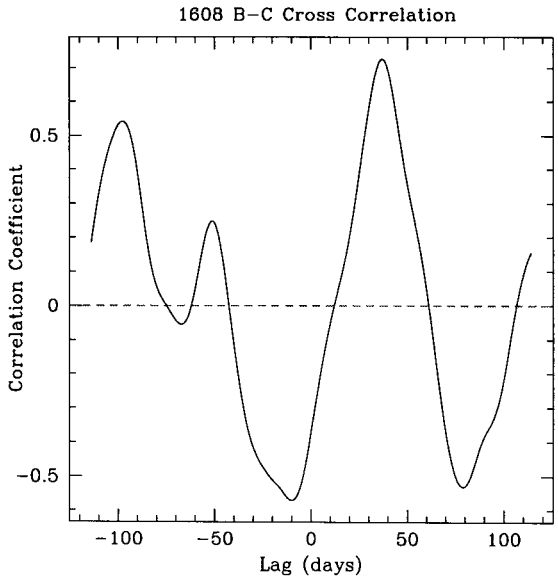

Figure 5.9 Same as Fig. 5.8 but for light curves of components B and C. The maximum is at a lag of 37 d.

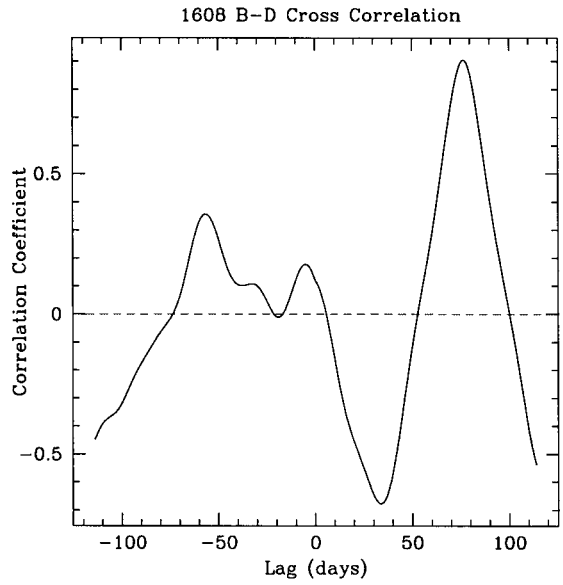

Figure 5.10 Same as Fig. 5.8 but for light curves of components B and D. The maximum is at a lag of 77 d.

the scatter is small compared with the length of the time delays and is comparable to the uncertainties in the delays that we find from the Monte Carlo simulations in §5.5.2. We take the median values of the delays in Table 5.2 to obtain $\Delta t_{BA} = 30$ d, $\Delta t_{BC} = 36$ d, and $\Delta t_{BD} = 76$ d. The median flux density ratios are $S_A/S_B = 2.043$, $S_C/S_B = 1.038$, and $S_D/S_B = 0.3504$. We shift the light curves by the median delays and normalize them using the median flux density ratios to create a composite light curve of the background source (Fig. 5.11). A composite curve constructed from the smoothed and interpolated component light curves is shown in Fig. 5.12.

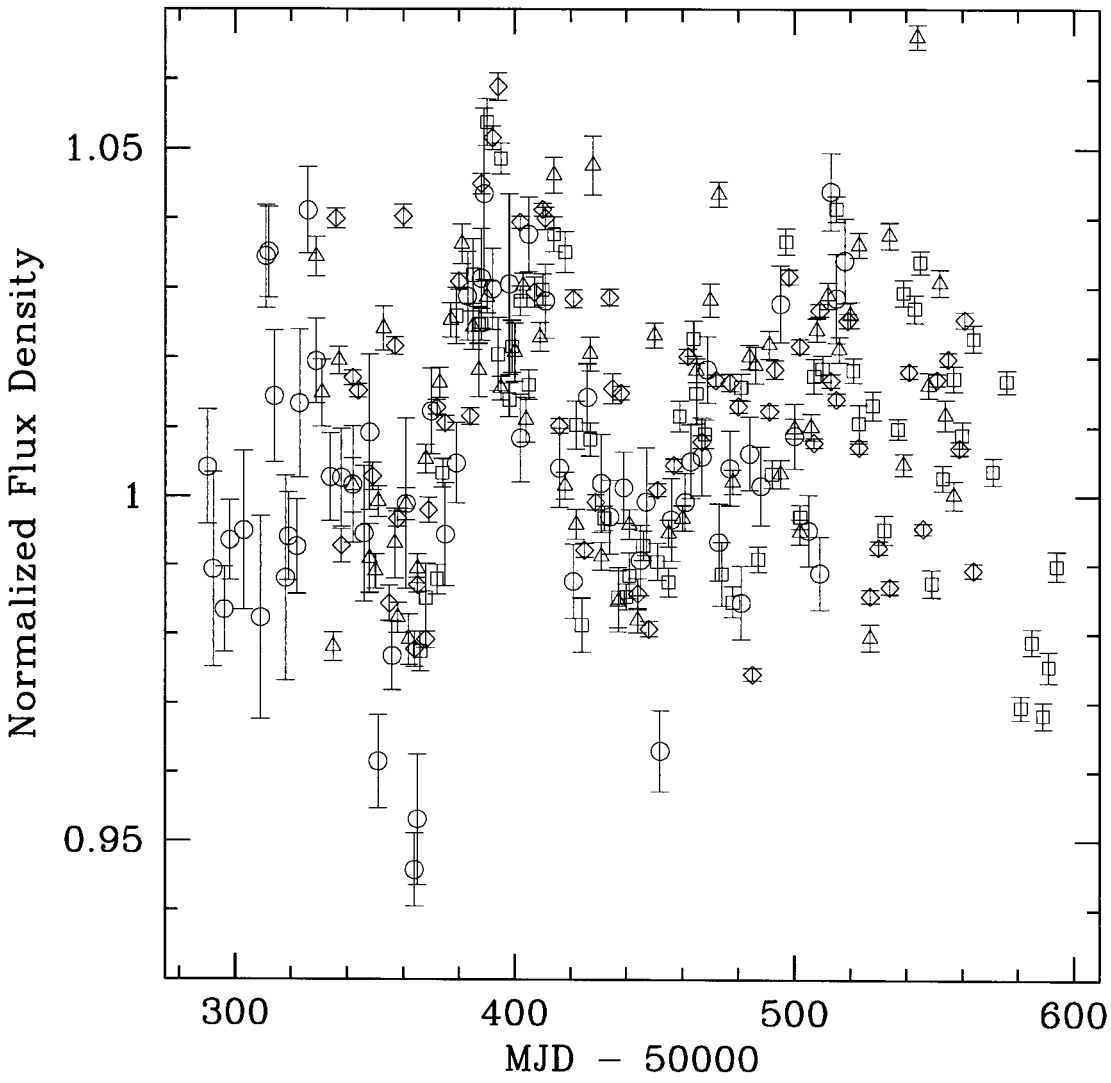

Figure 5.11 Composite light curve constructed by normalizing the component light curves and shifting by the lags given in §5.4.4. The light curves are represented by squares (component A), diamonds (B), triangles (C), and circles (D). For clarity of presentation, error bars represent only the additive component contributed by the RMS noise in the maps (see §5.3.6).

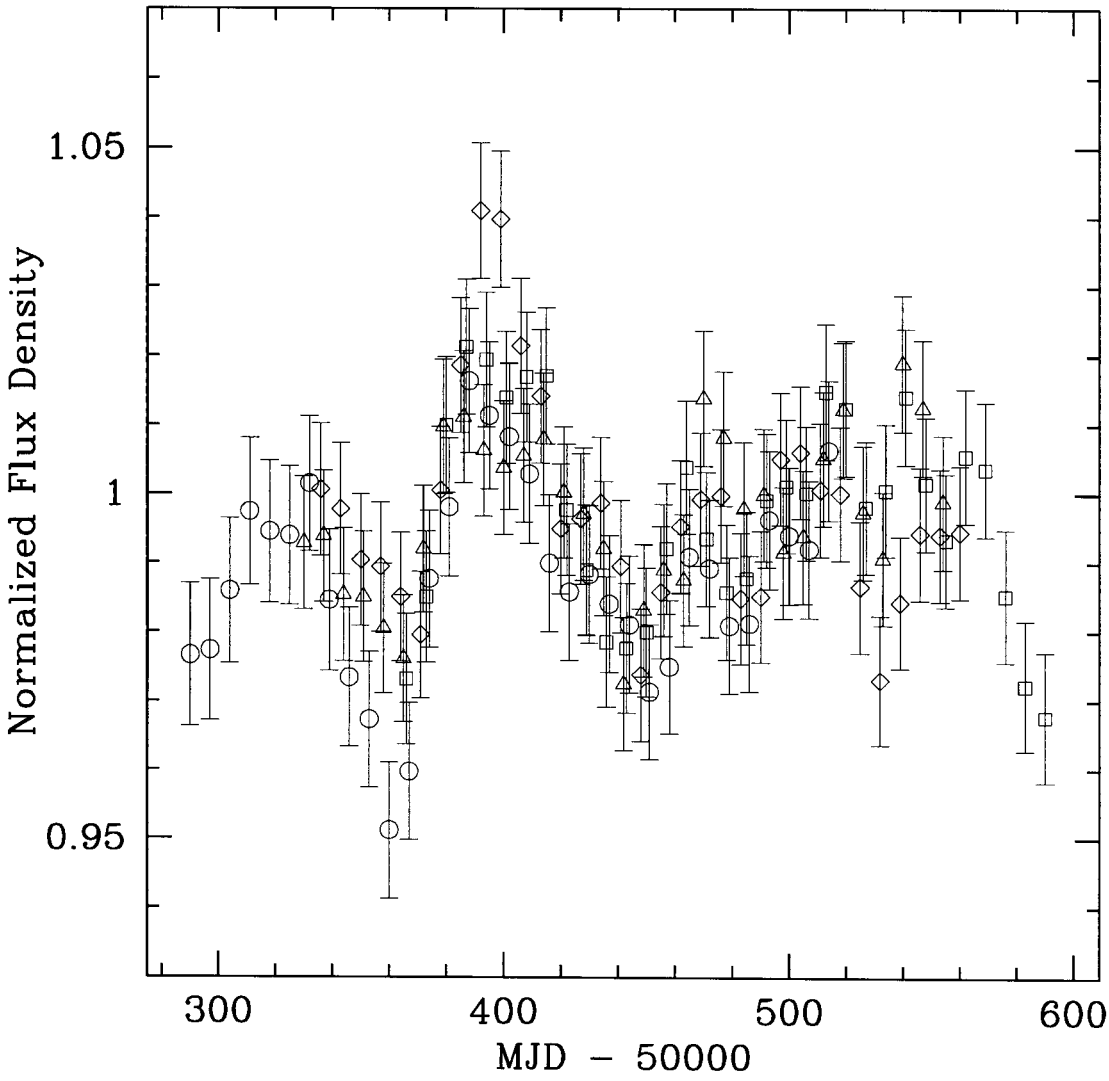

Figure 5.12 Composite light curve constructed as in Fig. 5.11, but using smoothed rather than raw light curves. The curves are smoothed with a boxcar of width 15 d. For clarity, only one out of every 7 points is shown for each curve.

5.5 Monte Carlo Simulations

5.5.1 Significance of Light Curve Correlations

As noted above, the variations seen in the 1608+656 light curves are not large, either in a fractional *or* absolute sense, compared to what has been seen in other lens systems. The fractional variations seen in 0218+357, 0957+561, and 1115+080 are all two to three times larger than those seen in 1608+656 (Biggs et al. 1998; Kundić et al. 1995,1997; Schechter et al. 1997), and PKS 1830−211 shows 50% variations in flux density[2] (Lovell et al. 1998). A sceptic might argue that the correlations between the 1608+656 light curves are not significant and could be duplicated by any set of light curves containing random scatter about a constant value.

In theory, the value of the correlation coefficient can be used to assess the significance of the correlation. With the coefficient, r calculated as described in §5.4.3, the probability of obtaining a value $\geq r$ from two *uncorrelated* curves of Gaussian-distributed random variables is

$$P_c(r, N) = 2 \int_{|r|}^{1} P_r(\rho, \nu) d\rho \tag{5.7}$$

where

$$P_r(r, \nu) = \frac{1}{\sqrt{\pi}} \frac{\Gamma[(\nu+1)/2]}{\Gamma(\nu/2)} (1 - r^2)^{(\nu-2)/2} \tag{5.8}$$

and $\nu = N - 2$ (e.g., Bevington 1969). However, the smoothing and interpolation

[2]For a base flux density of 4 Jy!

performed on the sparsely sampled 1608+656 light curves makes the interpretation of the significance of the value of r complicated. The difficulty lies in assessing the number of *independent* points in the curves at each lag. Monte Carlo simulations show that the number of independent points cannot be estimated simply as the width of the overlap region divided by the width of the smoothing window (i.e., the number of smoothing windows in the overlap region). This calculation *underestimates* the number of independent points in the region. Because it is difficult to determine the significance of the correlation analytically, we perform Monte Carlo simulations to find the significance empirically. In the simulations, we calculate correlations between light curves consisting of randomly distributed data. To create random light curves with the same distribution of flux densities as seen in the data, we simply randomize the time series for the component light curves while preserving the flux densities at their measured values. By randomizing the times at which the flux densities are measured, we destroy any possible correlations between the curves. Each light curve is randomized independently so that correlations at zero lag associated with measurement errors are avoided.

The simulations are conducted with 3000 sets of randomized curves. Each set of light curves is processed in the manner described in §5.4.3 and produces three sets of correlation curves (B–A, B–C, and B–D). All values of the correlation coefficient are recorded. The distributions of the cross-correlation values obtained from the

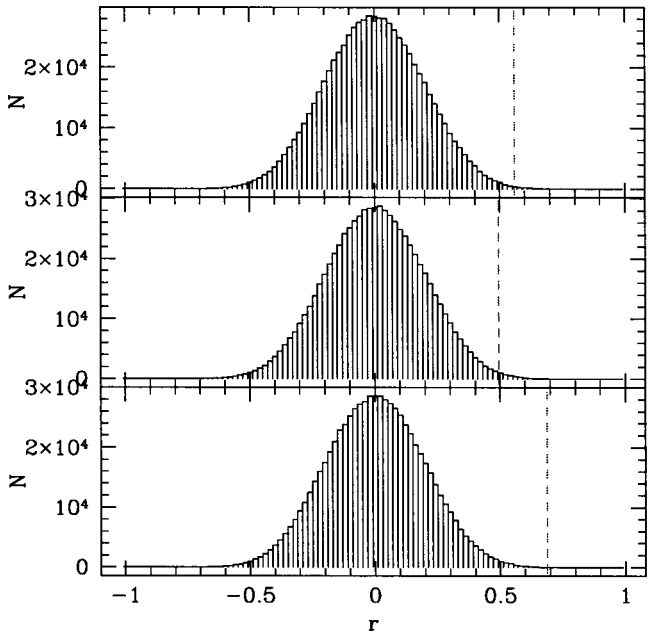

Figure 5.13 Distribution of cross-correlation values obtained from 3000 Monte Carlo simulations of randomized light curves. The distributions presented in this figure are obtained by smoothing the light curves with a boxcar of width 10 d. The dashed vertical lines represent the peak cross-correlation values obtained from the real data.

10 d boxcar smoothing scheme are shown in Fig. 5.13. The empirical probabilities of obtaining at least the observed peak values, which are indicated by the vertical dashed lines in the figure, from uncorrelated curves are all low, with $P(|r| \geq |r_A|) = 0.0026$, $P(|r| \geq |r_A|) = 0.0095$, and $P(|r| \geq |r_D|) = 9.7 \times 10^{-5}$. It is even more unlikely that three pairs of randomized curves could produce three such anomalously high cross-correlation peaks. There can thus be no significant doubt that the correlations we measure are real.

5.5.2 Uncertainties in Time Delays and Flux Density Ratios

The time delay measurement uncertainties contribute directly to the error budget for measuring H_0 with a gravitational lens. In particular, the fractional uncertainties in the time delays contribute a matching fractional uncertainty in H_0, i.e.,

$$\frac{(\sigma_H)_{delay}}{H_0} = \frac{\sigma_{\Delta t}}{\Delta t}. \tag{5.9}$$

We estimate the uncertainties in the time delays by performing Monte Carlo simulations of the observations. In the simulations we assign time delays between the pairs of light curves and then see how well we can recover the input delays. We also use the simulations to estimate the uncertainties in the flux density ratios, which are necessary for modeling the lensing potential (Paper 2).

We produce fake curves with the same characteristics as our real data by smoothing the composite light curve (Fig. 5.11) to create a master light curve. This curve represents the true behavior of the background source. The offsets between the points of the composite curve and the master curve are distributed as a zero-mean Gaussian with $\sigma = 0.014$. Note that this is a *fractional* value since all of the light curves have been normalized to create the master light curve. The Gaussian distribution is used to generate the random offsets for the simulations. The appropriate rescaling of the random offsets is achieved through Equation 5.10.

For each round of the simulation we generate four sparsely-sampled fake light

curves. The flux density for component j at a time t_i in the fake curves is given by:

$$S_j(t_i) = S_B\, R_j(S_0(t_i + \Delta t_j) + n_{ij}), \quad j = A, B, C, D \tag{5.10}$$

where $S_0(t)$ is the master flux density, the R_j are the input flux density ratios (2.043, 1.000, 1.038, and 0.3504), the Δt_j are the input time delays (30 d, 0 d, 36 d, and 76 d), and n_{ij} is the random offset. The value for S_B is fixed at 16.625 mJy. The four curves are sampled with the pattern used in the observations (see Table 5.1). The flux density error at each point in the sparsely-sampled curves is set to the observed flux density error for that epoch (see §5.3.6).

The fake curves are processed in the manner described in §5.4. The best-fit time delays and flux density ratios for each simulation are recorded. Histograms of typical distributions of time delays from 4000 repetitions of the above procedure are shown in Fig. 5.14. The distributions are highly non-Gaussian. Thus, we determine the confidence limits by finding the lags which enclose 95% of the data rather than fitting a Gaussian to the distribution. The results for the χ^2 minimization and cross-correlation techniques are given in Table 5.4. We conservatively take the broader distribution in each case as our estimate of the 95% confidence contours. Thus, we estimate the time delays to be $\Delta t_{BA} = 30^{+5}_{-7}$ d, $\Delta t_{BC} = 36^{+5}_{-8}$ d, and $\Delta t_{BD} = 76^{+6}_{-7}$ d.

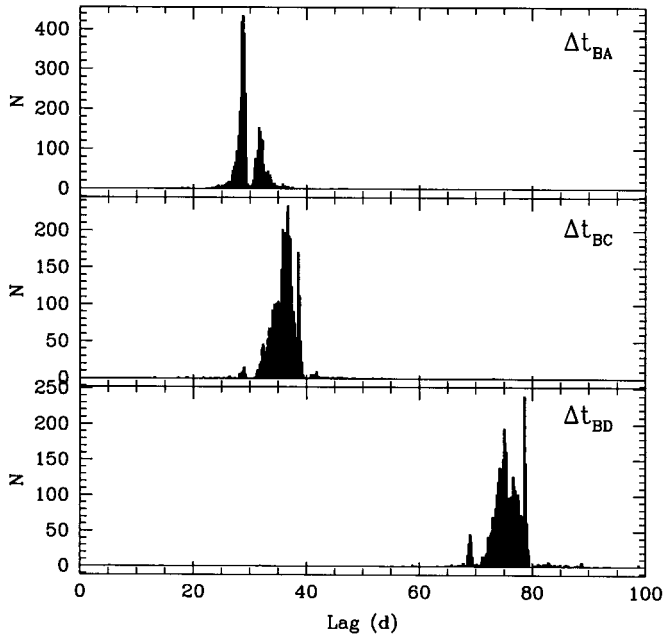

Figure 5.14 Distribution of time delays recovered from 4000 Monte Carlo simulations of the 1608+656 component light curves. The distributions provide estimates of the uncertainties in the time delays.

Table 5.4 UNCERTAINTIES IN TIME DELAYS FROM MONTE CARLO SIMULATIONS

Quantity	Input Value	χ^2 Minimization[a]	Cross-correlation[a]
Δt_{BA}	30	25.5 – 34.6	23 – 35
Δt_{BC}	36	31.2 – 39.0	28 – 41
Δt_{BD}	76	68.6 – 79.3	69 – 82
S_A/S_B	2.0429	2.0363 – 2.0569	...
S_C/S_B	1.0378	1.0351 – 1.0456	...
S_D/S_B	0.3504	0.3490 – 0.3526	...

[a]Range encloses 95% of data.

5.6 Discussion

The goal of monitoring a gravitational lens system is to measure time delays that can then be combined with a model of the lensing potential to produce a measurement of H_0. We have been successful in measuring the three independent time delays in the 1608+656 system. Paper 2 presents a model for the 1608+656 system. The model is based on the time delays and flux density ratios presented here, and on positions from VLBA (Fassnacht et al. 1998a) and HST observations of the system (Jackson et al. 1997; Fassnacht et al. 1998b). The lensing potential contains contributions from the two lensing objects seen in HST images of the system (Jackson et al. 1997), each of which is modeled as an elliptical isothermal mass distribution. The effects of varying the positions of the lensing galaxies, of changing the nature of the lensing galaxy cores (singular or non-singular), and of departing from an isothermal profile are all explored. The best-fit model is obtained through a simulated annealing process. It correctly reproduces the positions and flux density ratios of the lensed images (with the exception of the D/A flux density ratio). Most importantly, the predicted time delay ratios match the observed time delay ratios to within 2%. Although the individual time delays depend on the Hubble Constant ($\Delta t_i \propto h^{-1}$), the time delay ratios have no H_0 dependence. Thus, the model for any lens with more than two images *must* correctly reproduce the observed time delay ratios if it is to be used in the determination of H_0. In this sense, gravitational lenses

which produce more than two images can put stronger constraints on lens models than can two image lenses, as long as the time delays can be measured.

The 1608+656 system is the first four-image lens for which the three independent time delays have been measured and a model correctly reproduces the time delay ratios. The best-fit isothermal model from Paper 2 predicts time delays of $\Delta t_{BA} = 18.0\ h^{-1}$ d, $\Delta t_{BC} = 21.4\ h^{-1}$ d, and $\Delta t_{BD} = 44.9\ h^{-1}$ d. Combining these predicted values with the observed time delays gives three individual determinations of H_0: $(H_0)_A = 60.0$, $(H_0)_C = 59.4$, and $(H_0)_D = 59.1$ km sec^{-1} Mpc^{-1}. We combine these by calculating a weighted mean, where the weights are derived from the uncertainties in the time delays from §5.5.2 via Equation 5.9. The B-D value dominates the mean since it has the smallest fractional uncertainty. The weighted mean is $H_0 = 59^{+4}_{-5}$ km sec^{-1} Mpc^{-1}, where the uncertainty on the weighted mean is calculated as in Equation 5.2. The above calculations have not included the systematic effects from the choice of the radial mass profile in the lens modeling. The estimated systematic error is $\pm$15km sec^{-1} Mpc^{-1} (Paper 2). It may be possible to reduce this error by modeling the extended lensed stellar emission from the background source (see Figure 2.4), as has been done with the radio Einstein ring MG 1654+1346 (Kochanek 1995). This modeling approach is being conducted by Surpi & Blandford (1998).

5.7 Summary

We have presented the results of an intensive program of monitoring the four-image lens system 1608+656 with the VLA. The component light curves show 3 – 5% variations in flux density from which we have measured the three independent time delays in this system: $\Delta t_{BA} = 30^{+5}_{-7}$ d, $\Delta t_{BC} = 36^{+5}_{-8}$ d, and $\Delta t_{BD} = 76^{+6}_{-7}$ d. These time delays are combined with the mass model of the lens presented in Paper 2 to give $H_0 = 59^{+4}_{-5}$ km sec^{-1} Mpc^{-1} (statistical) ± 15 km sec^{-1} Mpc^{-1} (systematic). The statistical uncertainties represent the 95% confidence interval. The statistical uncertainties in the time delays can be reduced if a stronger variation in the background source is observed, while the systematic uncertainties may be reduced through the inclusion of the lensed extended emission in the lens modeling process. Our previous observations have shown that the background source in this system has varied by as much as 15% in the past, so we are conducting another program of monitoring. If a stronger variation is detected in the new data, the uncertainties on the time delays will be reduced and the accuracy of the measurement of H_0 with this system will be improved.

REFERENCES

Bevington, P. R. 1969, *Data Reduction and Error Analysis for the Physical Sciences*, (New York: McGraw-Hill)

Biggs, A. D., Browne, I. W. A., Helbig, P., Koopmans, L. V. E., Wilkinson, P. N., & Perley, R. A. 1998, MNRAS, submitted

Blandford, R. & Narayan, R., 1986, 310, 568

Blandford, R. D. & Narayan, R. 1992, ARA&A, 30, 311

Browne, I. W. A., Patnaik, A. R., Wilkinson, P. N., & Wrobel, J. M. 1997, MNRAS, in press

Fassnacht, C. D., Womble D. S., Neugebauer, G., Browne, I. W. A., Readhead, A. C. S., Matthews, K., & Pearson, T. J. 1996, ApJ, 460, L103

Fassnacht, C. D. et al. 1998, in preparation.

Fassnacht, C. D., Pahre, M. A., & Readhead, A. C. S. 1998, in preparation

Haarsma, D. B., Hewitt, J. N., Lehár, J., & Burke, B. F. 1998, ApJ, in press (astro-ph/9807115)

Högbom, J. 1974, ApJS, 15, 417

Impey, C. D., Falco, E. E., Kochanek, C. S., Lehár, J., McLeod, B. A., Rix, H.-W., Peng, C. Y., & Keeton, C. R. 1998, ApJ, submitted (astro-ph/9803207)

Jackson, N. J., Nair, S., Browne, I. W. A. 1997, in Observational Cosmology with the New Radio Surveys, eds., M. Bremer, N. Jackson & I. Perez-Fournon, (Dordrecht: Kluwer) 315

Kochanek, C. S. 1995, ApJ, 445, 559

Koopmans, L. V. E. & Fassnacht, C. D. 1998, ApJ, submitted

Kundić, T. et al. 1995, ApJ, 455, L5

Kundić, T. et al. 1997, ApJ, 482, 75

Lovell, J. E. J., Jauncey, D. L., Reynolds, J. E., Wieringa, M. H., King, E. A., Tzioumis, A. K., McCulloch, P. M., & Edwards, P. G. 1998, ApJ, in press (astro-ph/9809301)

Moore, C. B. & Hewitt, J. N. 1997, ApJ, 491, 451

Myers, S. T., et al. 1995, ApJ, 447, L5

Myers, S. T., et al. 1998, in preparation

Oscoz, A., Mediavilla, E., Goicoechea, L. J., Serra-Ricart, M. & Buitrago, J. 1997, ApJ, 479, L89

Patnaik, A. R., Browne, I. W. A., Wilkinson, P. N., & Wrobel, J. M. 1992b, MNRAS, 254, 655

Perley, R. A. & Taylor, G. B. 1997, *VLA Calibrator Manual*

Refsdal, S. 1964, MNRAS, 128, 307

Schechter, P. L., et al. 1997, ApJ, 475, L85

Schneider, P., Ehlers, J., & Falco, E. E. 1992 *Gravitational Lenses*, (New York: Springer-Verlag)

Shepherd, M. C. 1997, in *Astronomical Data Analysis Software and Systems VI*, eds. G. Hunt & H. E. Payne, (ASP Conference Series, v125) 77

Snellen, I. A. G., de Bruyn, A. G., Schilizzi, R. T., Miley, G. K. & Myers, S. T. 1995, ApJ, 447, L9

Supri, G. & Blandford, R. D. 1998, in preparation

Walsh, D., Carswell, R. F., & Weymann, R. J. 1979, *Nature*, 279, 381

Weymann, R. J., Latham, D., Roger, J., Angel, P., Green, R. F., Liebert, J. W., Turnshek, D. A., Turnshek, D. E., & Tyson, J. A. 1980, *Nature*, 285, 641

White, R. J. & Peterson, B. M. 1994, PASP, 106, 879

Wilkinson, P. N., Browne, I. W. A., Patnaik, A. R., Wrobel, J. M., & Soratia, B. 1998, MNRAS, in press

Chapter 6

Summary

6.1 A Grad Student Looks at Thirty-one

When I began this thesis project several years ago, my rather grandiose goal was to make a measurement of the Hubble Constant with one of the new gravitational lenses that we would (presumably) discover in the CLASS sample. At that time, 0957+561 was the only lens which had provided a determination of H_0, and that measurement was controversial. Kundić et al. (1995, 1997a) had not yet made the observations that finally ended the debate over the "long" vs. "short" delay in that lens. There have certainly been times along the way when I have had doubts about whether this project would have any success. There was, after all, no guarantee that CLASS would provide interesting lenses, or that the background source in my favorite lens system would vary enough to provide a clear measurement of a time delay. In spite of those doubts, the project has worked out extremely well. First, the CLASS project has been

very successful. Twelve new gravitational lenses have been discovered, and there are still several lens candidates that need to be investigated further. Second, each of the newly-discovered lens systems has its own unique and intriguing aspects. The two lens systems discussed in this thesis certainly presented some surprises. Finally, 1608+656 was variable during the time it was being monitored.

The lens 2045+265 has several traits that makes it an interesting system to study. First, it appears that the lensing galaxy is a flat-spectrum radio source. This fact aids in the modeling of the system because the position of the flat-spectrum core of the lensing galaxy can be determined accurately from radio observations. The ability to fix the relative positions of the lens and the lensed images of the background source to high precision places strong constraints on models of the lensing potential. Second, there are indications that the images of the background source are resolved at milliarcsecond (mas) resolution. As discussed in Chapter 1, if the images of the background source are resolved and a mapping from one to the other can be made, constraints can be placed on the model by limiting the second derivatives of the gravitational potential. Third, the flux density ratios of the three brightest components are not what is expected from generic lens models. This disparity arises from a perturbation of the gravitational potential, which may be caused by, say, a spiral arm (e.g., Mao & Schneider 1997). Finally, the redshift of the background source, if correct, implies an *extremely* massive lensing galaxy. When higher-quality spectra of

the system can be obtained, the redshift of the background source may be unambiguously measured, and this issue will be settled. Until then, we are presented with a system for which all of the arguments based on galaxy masses, mass-to-light ratios, and the fundamental plane (C. Kochanek, private communication) are in favor of a high-redshift source, but for which the spectrum seems to indicate a lower redshift.

The 1608+656 system also has many interesting characteristics. First, images taken with the *Hubble Space Telescope* show that there are two lensing galaxies inside the ring of images, which may be in the process of merging (Jackson et al. 1997). Secondly, the background source is unusual for a radio-loud lens system in that it is not a quasar, but rather an E+A (or K+A) galaxy. The extended stellar emission from the background source is seen clearly in HST images, where it is lensed into arcs. A faint Einstein ring is also seen in these images. Third, there is evidence that the lens may be part of a compact group of galaxies, making it similar to 1422+231 and PG 1115+080 (Kundić et al. 1997b,c; Tonry 1998). Finally, the system is exciting for those of us on the quest for H_0 because the background source is variable.

6.2 Thoughts About 1608+656 and H_0

The observations presented in Chapter 5 have given a measurement of H_0 from 1608+656. How does this measurement compare to the values of H_0 found from other lens systems? There are four other systems for which time delays

Table 6.1 VALUES OF H_0 FROM GRAVITATIONAL LENS SYSTEMS

Lens System	H_0	Notes
B0218+357	69^{+13}_{-19}	2σ uncertainties. Model from Biggs et al. 1998
0957+561	63 ± 12	Model from Grogin & Narayan 1996
PG1115+080	44 ± 4	Model from Impey et al. 1998
1608+656	$59 \pm 4 \pm 15$	2σ uncertainties. Model from Koopmans & Fassnacht 1998
PKS1830−211	65^{+16}_{-9}	1σ uncertainties. Model from Nair et al. 1993

have recently been measured: 0957+561 (Kundić et al. 1995; Kundić et al. 1997a; Oscoz et al. 1997; Haarsma et al. 1998), PG 1115+080 (Schechter et al. 1997), B 0218+357 (Biggs et al. 1998), and PKS 1830−211 (Lovell et al. 1998). The lens models for these systems change slightly as new observations are taken. However, the changes in the models usually do not push the calculated value of H_0 outside the region defined by the uncertainties of the previous determinations. All four systems yield values of H_0 consistent, within the errors, with that derived from 1608+656 (Table 6.1). More systems need to be observed, but already it is apparent that that gravitational lenses are fulfilling their promise as tools to investigate cosmology.

6.3 "To Infinity and Beyond!*" – What Secrets Does the Future Hold?

*Buzz Lightyear, in *Toy Story*.

6.3.1 1608+656 and 2045+265 Revisited

Although the observations presented in this thesis have provided a wealth of information about 1608+656 and 2045+265, they have also raised several questions. Below is a list of observational and theoretical work that might provide answers to some of the questions.

Do the lensed images in 1608+656 and 2045+265 show extended milliarcsecond-scale structure? In order to use a lens system to derive H_0, the model of the gravitational potential of the lensing object must be well-constrained. If the observational constraints are not strong, there is considerable freedom in choosing the radial profile of the mass distribution of the lens. This freedom in the modeling process leads to large uncertainties in any determination of H_0 from the system. Therefore, it is important to obtain as many observational constraints as possible. One such constraint comes from the flux density ratio of the images (Chapter 1). This constraint is strengthened if the images of the background source are resolved and a mapping from one image to the other can be deduced (e.g., Gorenstein et al. 1988). I have obtained deep VLBA images of both 1608+656 and 2045+265, with which I will search for extended milliarcsecond-scale emission in the lensed images.

What is the redshift of the background source in 2045+265? The redshift of the background source in 2045+265 is based on one broad emission line. The interpretation of the spectrum presented in this thesis suggests that this line is Mg II,

giving a source redshift of $z_s = 1.28$. However, as discussed in Chapter 4, this redshift suggests that the mass of the lensing galaxy is outrageously large. A higher redshift for the background source would alleviate the problem. Sensitive spectroscopic observations need to be made to search for another emission line so that the source redshift can be determined unambiguously.

Can 2045+265 be used to determine H_0? There are several observations that need to be performed if 2045+265 is to be used to determine H_0. First, the background source redshift must be confirmed, as discussed above. Second, the lens model must be improved to account for the unusual flux density ratios in the system and to include any extended small-scale structure that may be found in the VLBA observations. Third, evidence for variability must be found. If the source is observed to vary, an intensive monitoring program can be conducted.

Can the uncertainties on the 1608+656 time delays be reduced? The uncertainties on the 1608+656 time delays presented in Chapter 5 are relatively large because the observed fractional variations in flux density are small ($\sim 3 - 5\%$). If stronger variations can be observed, the uncertainties in the delays should decrease. I am conducting a second program of monitoring on 1608+656 with the VLA to search for stronger variations.

Can the uncertainties in the 1608+656 model be reduced? The systematic uncertainties in the value of H_0 derived from 1608+656 are large compared to

the statistical uncertainties. The systematic uncertainties arise from the freedom in choosing a radial mass profile for the lensing galaxy. It may be possible to constrain the mass profile further by modeling the lensed stellar emission from the background source. This lensed emission forms arcs and a faint Einstein ring in the HST images (Jackson et al. 1997; see also Figure 2.4). This procedure was used by Kochanek (1995) in modeling the Einstein ring in MG 1654+134. The ring emission provided observational constraints that limited the radial mass profile of the lensing galaxy. I have obtained deep NICMOS images of 1608+656 which are being used by Surpi & Blandford (1998) to model the extended emission. Similarly, Schechter has very deep WFPC2 images of the system, which could be used for the same purpose.

6.3.2 Why Stop at One Cosmological Parameter?

As discussed in Chapter 1, the optical depth to lensing as a function of source redshift can be used to place limits on Λ. The CLASS+JVAS sample is the largest systematically selected sample of radio sources which has been carefully searched for lens systems. As such, the observed lensing rate in the CLASS+JVAS samples can be used to place strong limits on Λ. However, the redshift distribution of the parent sample is unknown since no large redshift surveys of faint flat-spectrum radio sources have been conducted. My colleagues and I are addressing this issue through spectroscopic observations of very faint flat-spectrum radio sources at Keck and Palomar. The lenses

discovered in CLASS have typical magnifications of $\sim$10 and total flux densities in the range 25 – 200 mJy. From deep observations with the Westerbork Synthesis Radio Telescope we have selected a sample of 40 flat-spectrum radio sources with flux densities between 2.5 and 5 mJy. We are in the process of observing these sources spectroscopically to estimate the redshift distribution of the parent population of the faintest CLASS lenses.

6.4 Final Thoughts

In this chapter I have outlined some projects growing out of the work presented in this thesis. These projects only scratch the surface. CLASS has been enormously successful in providing a sample of sources with which any number of fun and interesting scientific investigations can be conducted. I am looking forward to hearing the results of these cosmological explorations.

REFERENCES

Biggs, A. D., Browne, I. W. A., Helbig, P., Koopmans, L. V. E., Wilkinson, P. N., & Perley, R. A. 1998, MNRAS, submitted

Gorenstein, M. V., Cohen, N. L., Shapiro, I. I., Rogers, A. E. E., Bonometti, R. J., Falco, E. E., Bartel, N., & Marcaide, J. M. 1988, ApJ, 334, 42

Haarsma, D. B., Hewitt, J. N., Lehár, J., & Burke, B. F. 1998, ApJ, in press (astro-ph/9807115)

Impey, C. D., Falco, E. E., Kochanek, C. S., Lehár, J., McLeod, B. A., Rix, H.-W., Peng, C. Y., & Keeton, C. R. 1998, ApJ, submitted (astro-ph/9803207)

Jackson, N. J., Nair, S., Browne, I. W. A. 1997, in Observational Cosmology with the New Radio Surveys, eds., M. Bremer, N. Jackson & I. Perez-Fournon, (Dordrecht: Kluwer) 315

Kochanek, C. S. 1995, ApJ, 445, 559

Koopmans, L. V. E. & Fassnacht, C. D. 1998, in preparation

Kundić, T. et al. 1995, ApJ, 455, L5

Kundić, T. et al. 1997a, ApJ, 482, 75

Kundić, T., Cohen, J. G., Blandford, R. D., & Lubin, L. M. 1997b, AJ, 114, 507

Kundić, T., Hogg, D. W., Blandford, R. D., Cohen, J. G., Lubin, L. M., & Larkin, J. E. 1997c, AJ, 114, 2276

Lovell, J. E. J., Jauncey, D. L., Reynolds, J. E., Wieringa, M. H., King, E. A., Tzioumis, A. K., McCulloch, P. M., & Edwards, P. G. 1998, ApJ, in press (astro-ph/9809301)

Madore, B. F., et al. 1998, Nature, in press

Mao, S. & Schneider, P. 1998, MNRAS, 295, 587

Nair, S., Narasimha, D., & Rao, A. 1993, ApJ, 407, 46

Oscoz, A., Mediavilla, E., Goicoechea, L. J., Serra-Ricart, M., & Buitrago, J. 1997, ApJ, 479, L89

Schechter, P. L., et al. 1997, ApJ, 475, L85

Supri, G. & Blandford, R. D. 1998, in preparation

Tonry, J. 1998, AJ, 115, 1